Long-Term Partial Discharge Behavior of Protrusion and Free Metallic Particle Defects in Air-Insulated HVDC Gas-Insulated Substations

A Study on Long-Term PD Behavior

Luka Šćulac

TUDelft

NTNU

Long-Term Partial Discharge Behavior of Protrusion and Free Metallic Particle Defects in Air-Insulated HVDC Gas-Insulated Substations

A Study on Long-Term PD Behavior

by

Luka Šćulac

to obtain a Master of Science in Electrical Engineering at Delft University of Technology
and in Wind Energy Technology at the Norwegian University of Science and Technology,
to be defended publicly on Wednesday April 16, 2025 at 10:00 AM.

Student number:	5911761 / 123722
Project duration:	August 20, 2024 – April 16, 2025
Thesis committee:	Prof. ir. P. T. M. (Peter) Vaessen Prof. ir. F. (Frank) Mauseth Dr. H. (Hani) Vahedi Dr. H. K. H. (Hans Kristian Hygen) Meyer Dr. M. G. (Mohamad Ghaffarian) Niasar
Faculty:	Faculty of Electrical Engineering, Mathematics and Computer Science, Delft
Faculty:	Faculty of Electric Energy, Trondheim
Company:	Siemens Energy, Munich

Style: TU Delft Report Style, with modifications by Daan Zwaneveld

Preface

I want to dedicate this master's thesis to all the wonderful individuals I have encountered on my journey during the EWEM program. I have shared numerous newfound experiences and spent some of the best years of my life with my classmates. The countless hours spent in lecture halls and project rooms have gifted me invaluable knowledge and admiration for the work and effort carried out by my fellow professors. The members of the thesis committee at TU Delft and NTNU and my daily supervisors at TU Delft and SINTEF have worked tirelessly to guide and aid me in every possible way. Without their insightful expertise and thought-provoking discussions, I would not have achieved the standard and quality expected of any student graduating from these world-class universities. I want to thank the EWEM coordinators whose careful guidance has made the experience rewarding and life-altering. I hope this will not be the last time I see these wonderful individuals.

In writing the thesis, I tried to culminate all the knowledge I have acquired in my nearly nine-year academic career. Starting from a crowded college dorm in Los Angeles, I always believed I would achieve something remarkable. The dream led me to the University of Twente in the small city of Enschede in the Netherlands, where I completed my bachelor's degree. I did not rest as I pushed further forward, landing in Aachen to pursue a master's degree at RWTH. Becoming complacent, I stumbled upon the EWEM program and its offer to experience three different universities (DTU, TU Delft, and NTNU) in lands far and wide. Everything happens for a reason and I see myself on the precipice of something great once again.

Lastly, I want to express my deepest gratitude to my parents, who believed in themselves and decided to leave Croatia to see what the world offered to those who dare.

Luka Šćulac
Trondheim, April 2025

Summary

High-voltage direct current (HVDC) has established itself as the leading technology for long-distance transmission, particularly for interconnections between countries and offshore wind farms. Sulfur hexafluoride (SF_6*) has traditionally been the preferred insulating medium in gas-insulated substations (GIS) due to its excellent dielectric properties; however, its high global warming potential (GWP) remains a significant drawback. Partial discharge (PD) detection serves as a critical diagnostic tool for ensuring the operational reliability of GIS systems. This study investigates the long-term PD behavior of protrusion and free metallic particle defects in HVDC GIS filled with technical air. The PD apparent charge magnitude and repetition rate evolution are analyzed using pulse sequence analysis (PSA) plots. Results indicate that PSA plots evolve and vary depending on the defect type, posing challenges for human experts and machine learning models in defect classification. Furthermore, most existing PSA plots are derived from test conditions using *SF_6*, highlighting the need for research in alternative insulation gases such as technical air. Both conventional and unconventional PD detection methods were employed within a full-scale GIS test cell. The two defect types were subjected to voltage application for one week. The free metallic particle defect exhibited a 20% change in PD apparent charge magnitude over the test duration but showed minimal alterations in weight and physical structure. In contrast, the protrusion defect experienced a 30% increase in PD apparent charge magnitude, accompanied by significant physical changes, as revealed through microscope imaging. The observed changes in PD behavior after just one day of voltage application suggest that long-term testing in technical air is unnecessary. Similarly, PSA patterns from *SF_6* were successfully used to classify defects in technical air, demonstrating that knowledge transfer is possible. Finally, the similarities between certain patterns of free metallic particles and protrusion defects in technical air highlight the need for further investigation in different test environments to refine defect classification in future studies.*

Contents

List of Figures

List of Tables

Nomenclature

Abbreviations

Abbreviation	Definition
AC	Alternating Current
AIS	Air-Insulated Substations
BDV	Breakdown Voltage
CO_2	Carbon Dioxide
C_4FN–CO_2	Fluoronitrile–CO_2 Mixture
C_5FK–dry air	Fluoroketone–Dry Air Mixture
DC	Direct Current
EM	Electromagnetic
EU	European Union
GIL	Gas-Insulated Line
GIS	Gas-Insulated Substations
GWP	Global Warming Potential
HF	High Frequency
HV	High Voltage
HVAC	High Voltage Alternating Current
HVDC	High Voltage Direct Current
IEC	International Electrotechnical Commission
IEEE	Institute of Electrical and Electronics Engineers
N_2	Nitrogen Gas
NoDi*	Normalized Differenced Star
PD	Partial Discharge
RF	Radio Frequency
PDIV	Partial Discharge Inception Voltage
PDEV	Partial Discharge Extinction Voltage
PRPD	Phase Resolved Partial Discharge
PSA	Pulse Sequence Analysis
SF_6	Sulfur Hexafluoride
UHF	Ultra High Frequency
VHF	Very High Frequency

Symbols

Symbol	Definition	Unit
C	Capacitance	$[F]$
f	Frequency	$[s^{-1}]$
R	Resistance	$[\Omega]$
V	Voltage	$[V]$
Z	Impedance	$[\Omega]$
α	Ionization coefficient	$[m^{-1}]$
$\bar{\alpha}$	Effective ionization coefficient	$[m^{-1}]$
η	Electron affinity	$[m^{-1}]$

1

Introduction

1.1. Motivation

The trend towards more renewable energy sources in the global energy grid has expedited the need for efficient long-distance bulk transmission capacity, as many large-scale plants such as wind and solar farms are far from demand centers. Historically, high-voltage alternating current (HVAC) has been the main transmission technology, benefiting from the early development of alternating current (AC) transformers that enabled switching between voltage levels. The development of mercury valves in the 1930s and thyristor valves in the 1960s paved the way for high-voltage direct current (HVDC) to enter the energy market. Today, both HVAC and HVDC are used in bulk energy transmission, but HVDC maintains distinct advantages. Over long distances, HVDC offers lower overall system costs and losses as it requires fewer conductors and utilizes the full transmission capacity due to the lack of the skin effect present in AC. [1]

As demand centers have grown into large urbanized areas, air-insulated substations (AIS) have become impractical due to their large space requirements. Substations are critical locations for tasks such as voltage transformation, circuit breaking, and disconnection of lines. In their place, gas-insulated substations (GIS) have grown in popularity as they offer numerous advantages over the traditional AIS options, making them an integral part of modern-day power systems. The key benefits include a space-saving design, independence from environmental conditions, and high reliability. By utilizing pressurized gas to insulate live components, GIS installations reduce the overall physical footprint by 70% compared to equivalent AIS configurations. While the initial investment is higher, the failure rate of the circuit breaker and busbar in GIS is one-fourth and one-tenth of that in AIS, respectively, owing to the sealed and protected nature of the components. [2]

Sulfur hexafluoride (SF_6) has been the mainstay of GIS for decades due to its superior dielectric strength and excellent thermal properties [3]. SF_6 delivers two to three times the breakdown strength of technical air at ambient pressure and exhibits arc-quenching and cooling qualities desired in operations such as circuit breaking [4]. However, SF_6 poses a serious threat to the environment in the event of a leak as its global warming potential (GWP) amounts to 24,300 times that of carbon dioxide (CO_2) [5]. To curb global temperature increase, the European Union (EU) provisionally agreed to ban high-voltage (HV) GIS systems relying on fluorinated gases by 2032, among other measures [6]. The EU has laid the groundwork for a collaborative project with industry-leading manufacturers to foster research and development efforts to replace SF_6 in GIS installations. This work contributes to the EU Project Mission by advancing the understanding of physical phenomena in HVDC GIS systems operating within $\pm$ 550 kV and further investigating technical air as an alternative insulating gas. [7] Some manufacturers have opted for synthetic air over technical air due to its consistent concentration of gas components, achieving 99.9999% purity in some cases and thereby offering more reliable performance characteristics [8]. For consistency, technical air refers to the dried and filtered air derived from the atmosphere that contains traces of CO_2 and argon. While this work uses technical air for the PD measurements, it also relies on research findings based on synthetic air for further reference due to the lack of literature directly comparing the two in GIS.

In literature, technical air, along with other natural-origin gases such as nitrogen gas (N_2) and CO_2, as well as fluorinated gases such as fluoroketone–dry air mixture (10%) (C_5FK–dry air) and fluoronitrile–CO_2 mixture (6.6%) (C_4FN–CO_2), have been extensively studied as potential alternatives to SF_6 [4], [9]–[13]. Dry air has emerged as a strategic choice as its environmental leakage poses no GWP and requires no special handling or storage precautions. [14] However, due to its lower electron affinity, dry air exhibits lower electrical strength than SF_6, even when subjected to higher pressures, as shown in Figure 1.1 [15]. The electrical strength of an insulating gas is reflected in its breakdown voltage (BDV), the threshold at which the insulating gas becomes conductive and breakdown occurs [16].

In inhomogeneous electric fields such as the one depicted in Figure 1.1 with a protrusion defect, raising the voltage from zero to the BDV limit reveals another phenomenon: the partial discharge inception voltage (PDIV), the threshold at which partial discharge (PD) activity starts. Increasing the gas pressure increases the PDIV, while increasing the length of the defect significantly reduces it, given that the other conditions remain the same. The lower PDIV of synthetic air than that of SF_6 is an unintended advantage, as PD activity is more easily detected. [17]

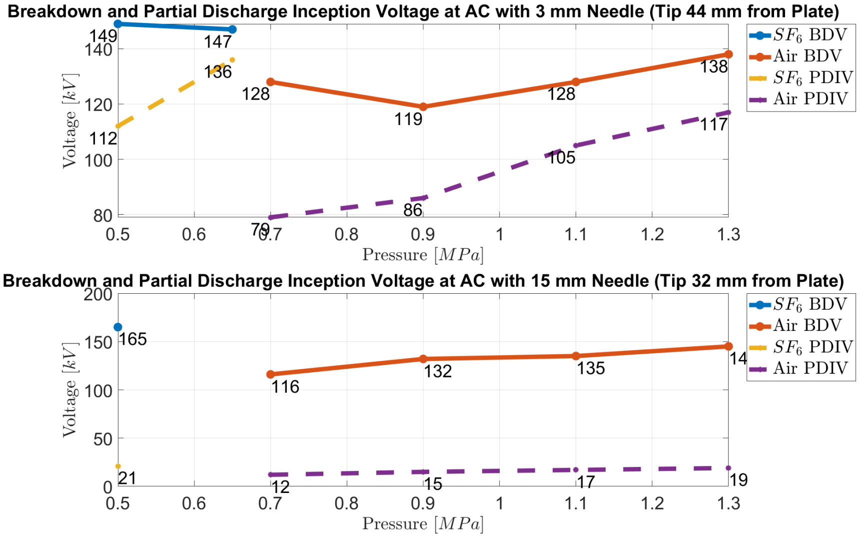

Figure 1.1: BDV and PDIV at AC voltage for protrusion defects (3 mm long needle with 200 μm tip radius and 15 mm long needle with 30 μm tip radius) with a diameter of 1 mm under SF_6 and synthetic air in GIS [17]

As the name suggests, a PD does not establish a full conductive path between a conductor and other live or insulating components, contrary to a complete breakdown. Defects such as protrusions and free metallic particles create a non-uniform electric field that results in localized electrical discharges once the PDIV is reached [16]. The electrical discharges can impact the integrity of the insulation and are a significant concern for end-users whose GIS installations typically remain operational for several decades. PD measurements offer invaluable insights into the breakdown mechanisms of insulating gases, as PD activity is a precursor to a possible breakdown event. Thus, PD measurements provide a reliable method for assessing the long-term health of GIS installations. These measurements are critical for identifying defects during production, installation, and operation to determine the risk of a dielectric breakdown. PD phenomena in HVAC GIS have been extensively studied, and different tools are already in place for industrial applications. However, the same knowledge set of PD behavior and defect identification cannot be carried over to HVDC GIS. [10]

PD behavior differs greatly from AC to direct current (DC) voltage due to the continuous charge accumulation facilitated by the constant electric field. Depending on the conductivity and permittivity of the insulating materials, the resulting electric field transition from a capacitive to a resistive distribution may take days to months, requiring careful testing to ensure a ”pure” DC environment [10]. Exhaustive studies on PD activity under DC voltage stress have investigated key effects, including those on PDIV

[10], [13], [15], [16], [18]–[23]. As illustrated in Figure 1.2, the PDIV values observed under AC voltages for technical air and SF_6 do not directly correlate to DC voltage conditions. Negative DC voltage consistently delivers the lowest PDIV values with protrusion and free metallic particle defects. Positive polarity exhibits a more unpredictable behavior, falling beneath or exceeding the PDIV of the negative half-wave of AC voltage across different gases for the same defect. The positive half-wave of AC voltage maintains the highest PDIV values across all cases presented in Figure 1.2. [12]

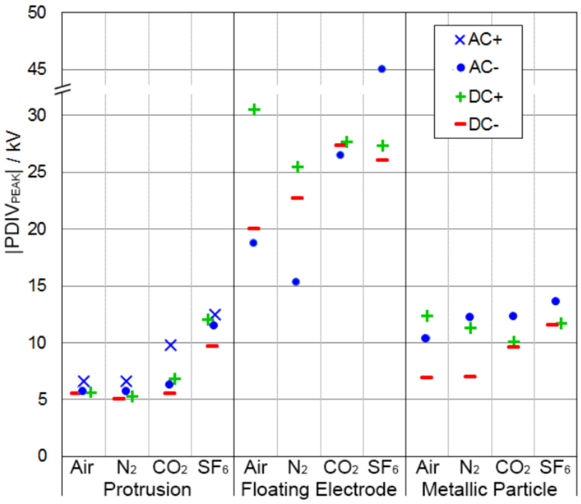

Figure 1.2: Peak value of the PDIV at the negative and positive half wave of AC voltage and negative and positive polarity of DC voltage with different defects at a gas pressure of 0.3 MPa [12]

While PD behavior such as the magnitude and time of occurrence can be distinguished between defects, T. Vu-Cong et al. [10] demonstrated that PD behavior for a protrusion defect in SF_6 and SF_6 alternative gases, C_5FK–dry air and C_4FN–CO_2, changed significantly over several days, concluding that PD behavior is not consistent. The authors argue that further research is needed to investigate the long-term aging of different defects and insulating gases, especially since most PD measurements are typically conducted for several minutes in short-duration voltage applications. Thus, understanding how PD behavior evolves is crucial for improving the reliability and performance of GIS installations under DC voltage stress.

1.2. Objectives of this Work

While various studies [12], [15], [24] have explored PD behavior in technical air under DC voltage stress, a critical gap remains in understanding its long-term evolution, especially at elevated pressures meant to match the breakdown strength of SF_6. The key uncertainty lies in how defects in GIS installations age over time in different gases and how these changes affect the characteristic PD magnitude and repetition rate of each defect type. Therefore, the primary objective of this thesis was to analyze the progressive, long-term evolution of PD behavior in technical air under DC voltage stress in full-scale GIS and to compare the results with the long-term study conducted by T. Vu-Cong et al. [10]. Due to time constraints, the highest pressure used was 3 Bar absolute.

This work focused on two common defect types in GIS: protrusions and free metallic particles. Both defects represent the most frequently encountered in GIS installations, and studying them under long-term conditions broadens the understanding of PD behavior over extended periods [25]. The defects received additional attention as the degree of erosion due to the electrochemical etching caused by PD activity needs to be evaluated. Additionally, the PD measurements for both defects are analyzed in depth to determine whether their respective PD characteristics can be reliably distinguished, thereby contributing to the already expansive backlog of PD patterns.

Finally, this research aimed to adapt the long-term PD measurement data into a format suitable for analysis and investigated the possibility of using algorithms to identify the defect type and polarity.

2

Theory

This chapter provides background information on PD phenomena under DC voltage, including the appropriate terminology and the defects considered in the experiments. Likewise, the PD measurement methods and analysis techniques used are covered. The theory focuses on the literature and knowledge necessary for proper PD measurement and correct defect recognition to further align with the experimental aim of this work.

2.1. Partial Discharge (PD) Fundamentals and Defects

As outlined in the International Electrotechnical Commission (IEC) 60270 standard, a PD is defined as a localized electrical discharge that does not fully bridge the insulation between two conductors. As PD activity is a consequence of local electrical stress concentrations, PD measurements are used as a diagnostic tool for detecting imperfections in GIS during installation, operation, and maintenance. [26] The defects in GIS installations are commonly found within the gas-insulated lines (GIL), where the live conductor is separated from the grounded housing by a gap filled with insulating gas [25].

However, the presence of a defect, such as a protrusion or free metallic particle, does not necessarily guarantee PD initiation. Two conditions must be met for a self-sustaining discharge to occur: first, a minimum breakdown voltage must be achieved in a portion of the insulating gas, and second, a free electron must be present to trigger the ionization process. The availability of a starting electron is inherently random and determined by a statistical lag time, which is affected by factors such as conductivity, temperature, and pressure [27].

PD activity is fundamentally tied to the ionization of gas molecules, requiring an understanding of the Townsend and streamer discharge mechanisms. The Townsend mechanism initiates the process by generating an electron avalanche, where the initial electrons, emitted from the cathode or generated through electron detachment from gas molecules by cosmic radiation, are accelerated by the stationary DC electric field. These electrons gain sufficient energy to ionize other molecules through collisions, creating a chain reaction expressed as the ionization coefficient, α. Concurrently, the electron affinity of the surrounding ions and molecules, η, opposes this process. The resulting effective ionization coefficient, $\bar{\alpha} = \alpha - \eta$, determines whether an avalanche develops. As the avalanche propagates between the electrodes, the differing drift velocities of electrons and ions result in an electron accumulation at the head. When the number of electrons exceeds 10^8, the local electric field strength is sufficiently high to achieve photoionization, thereby generating secondary electron avalanches in the vicinity and triggering a streamer discharge. The streamers generate charge carriers on a nanosecond scale, and the subsequent movement manifests as very fast electromagnetic (EM) or current pulses, depending on the measuring equipment, associated with PD events. Under the constant DC electric field, charge carriers can locally accumulate to form a stable space charge, resulting in a steady, pulseless glow discharge. [15]

There are several reasons why streamers may initiate but fail to bridge the gap between electrodes. In GIS, this often occurs when a region with a strong electric field distribution, sufficient to trigger initial avalanches, is adjacent to an area with a much weaker field that impedes further propagation [28]. As PD activity tends to occur in inaccessible areas during operation, understanding how these internal discharges can be modeled and later measured is essential.

2.1.1. PD Modeling

PD measurements stem from the first experiments on cavity defects within mass-impregnated cables in the 1930s [29]. The testing parameters spread thereafter to include protrusion and particle defects in HVDC GIS systems. Likewise, models were developed to better understand the relationship between the charge directly involved in the PD event and the one measured at the terminals of the test object. Naturally, advances in technology have enabled human operators to detect PD activity using methods that circumvent the need to measure directly across the terminals and instead rely on the capture of EM or acoustic signals. Nonetheless, the models developed for the charge associated with PD activity provide background on the important concept of apparent charge.

An equivalent circuit of capacitances was made and later modified in the 1950s to the now-known a-b-c model. Although originally intended for AC voltages, the a-b-c model can be adapted for DC voltage applications by incorporating resistors in parallel with the capacitors, as shown in Figure 2.1a. In this model, C_a and R_a represent the dielectric properties of the entire insulation; C_{b1}, C_{b2}, R_{b1}, and R_{b2} model the dielectric properties of the portion of insulating gas in series with the affected section; C_c and R_c represent the dielectric properties of the section experiencing the PD activity; the spark gap, F_c, mimics the breakdown event. During breakdown initiated by F_c, the internal charge can be calculated by relating the known capacitances and resistances to the measured external charge, known as the apparent charge. [29]

The term ”apparent charge” has been misinterpreted as an arbitrary value with no direct correlation to the actual discharge magnitude. This misunderstanding arises from the wording of the IEC 60270 standard, which explicitly states that the apparent charge ”is not equal to the amount of that charge involved at the site of the discharge, which cannot be measured directly” [29]. This assertion remains valid as long as the precise values of capacitances and resistances within the system remain unknown.

Research in the mid-1980s began to challenge the apparent charge concept, arguing that the a-b-c model inadequately represented the physics of gas discharge. Instead of an instantaneous breakdown as modeled by the spark gap, the discharge process involves the generation of charge carriers through ionization processes. Consequently, the spark gap in Figure 2.1a was replaced with a dipole moment to create the dipole model depicted in Figure 2.1b. [26] According to this model, the apparent charge is proportional to the real charge originating from the PD event through a continuous dimensionless positive scalar function that varies based on defect geometry and location [30].

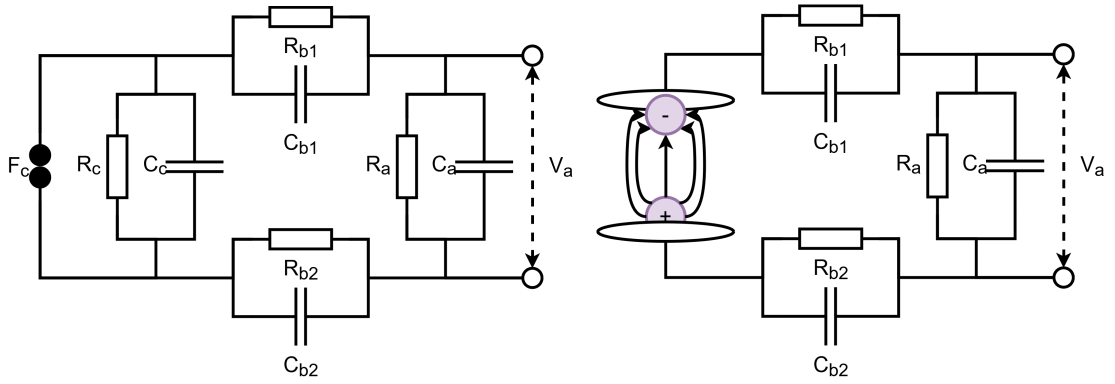

(a) Circuit schematic of the a-b-c model **(b)** Circuit schematic of the dipole model

Figure 2.1: Circuit schematic of the DC models used to simulate PDs in defects

Both the a-b-c and dipole models feed directly into the conventional approach to PD measurement, which relies on current measurements at the terminals of the test object. A detailed overview of the conventional and non-conventional methods utilized in this work, along with their operating principles, is provided in Section 2.2. With the fundamentals of PD and the associated models established, it is essential to delve into the complexities of protrusion and free metallic defects to characterize their distinctive PD behavior.

2.1.2. Protrusion Defect

Protrusions are one of the two defect types examined in this work and one of the most researched in PD behavior under DC voltage stress [27]. The PD behavior at inception is highly irregular, characterized by alternating phases of extinction and re-inception. In addition to variations in PD magnitude, breaks in the range of several seconds are observed due to the low number of starting electrons. [16]

The irregular behavior is further compounded by an abrupt change just before and at the BDV, as seen in Figure 2.2, despite a constant voltage and current increase. PD activity is evident above the PDIV with magnitudes of a few pC and time intervals of hundreds of microseconds. As the voltage applied approaches the BDV, PD activity either diminishes or ceases altogether, only to be reignited once the BDV is surpassed. [16] A. Pirker et al. [24] explained this phenomenon by the presence of space charges, resulting in corona stabilization effects or, in other words, the glow discharge. A constant corona current arises as a balance forms between the positive ions in front of the protrusion tip and the negative ions drifting in the insulating gas. The constant pulseless glow discharge fails to register as separate PD events on the measuring equipment, albeit detectable with optical methods. The electric field becomes homogenized, and a voltage increase is needed for breakdown.

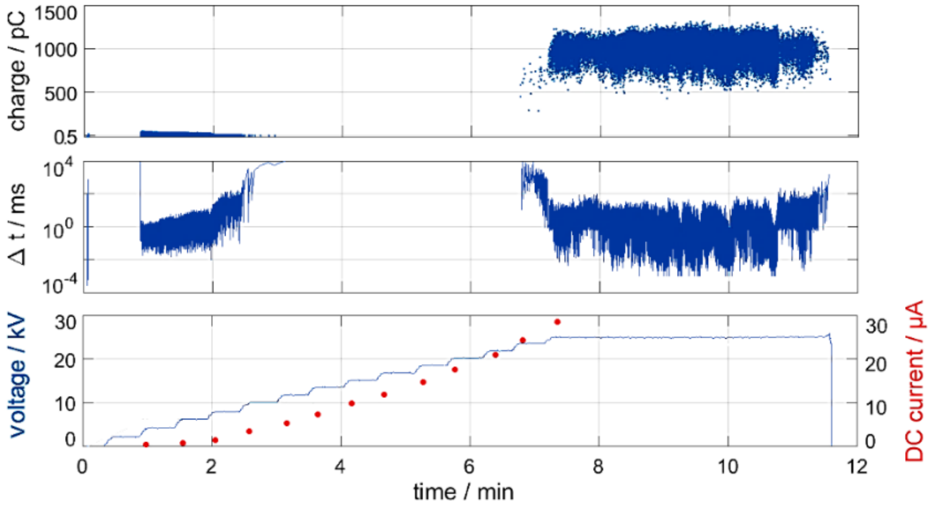

Figure 2.2: PD behavior of protrusion with a length of 40 mm and radius of 2.7 μm at positive DC voltage in air at 1 Bar [16]

When considering the PD behavior of protrusion defects, the influence of the tip radius cannot be overstated. Aside from the absolute value of the electric field, the tip radius dictates the size of the ionization region at the protrusion tip and, in turn, the number of electrons available for avalanche phenomena. A larger ionization volume results in a higher PD apparent charge magnitude. This correlation between tip radius and PD apparent charge magnitude was confirmed by T. Vu-Cong et al. [10] in their long-term analysis. Additional findings and corresponding defect patterns are discussed in Section 3.2. COMSOL simulations were conducted alongside this work but only reaffirmed the conclusions already set forth by the former paper. With the PD characteristics of protrusion defects addressed, the focus can now shift to examining those of free metallic particles.

2.1.3. Free Metallic Particle Defect

Free metallic particles are among the most prevalent defects found in GIS, accounting for an estimated 20% to 50% of system faults [3]. These particles typically originate from small metal abrasions when metal components rub against each other during installation or operation [22]. The behavior of free metallic particles under DC voltage stress is well documented, exhibiting a range of motions, including standing, bouncing, and firefly behavior.

The free metallic particles generally rest on the bottom of the grounded enclosure under no voltage conditions. At a certain voltage level, the electrostatic force acting on the particle exceeds the gravitational force, causing the particle to stand up or, in some cases, directly levitate. The magnitude of the electrostatic force and the corresponding charge on the particle depend on its shape, material properties, and diameter. Once the particle lifts off, its subsequent motion, whether bouncing or firefly, depends on several interrelated factors, such as material composition, gas pressure, and voltage polarity. [16]

Extensive research has validated the occurrence of these behaviors, their dependencies, and the thresholds at which they arise, as discussed in Section 3.3. Notably, C. Neumann et al. [16] provide a mathematical model for particle motion, incorporating the effects of electrostatic, gravitational, and viscous forces. However, determining the exact lift-off voltage is challenging without precise knowledge of the particle's charge. Instead, the lift-off voltage was determined empirically by carefully coordinating the voltage ramp-up, as further elaborated in Section 4.3. Nonetheless, the exact step-by-step mechanisms governing the bouncing and firefly motions are well understood and discussed in detail in the following sections.

Bouncing Particle Phenomenon

The particle predominantly undergoes the bouncing motion when the HV conductor is positively charged. As with either of the two motions, the particle experiences an electrostatic force, known as the Coulomb force, owing to the attraction and repulsion of the charges energized by the potential difference. Following the initial lift-off (a), as illustrated in Figure 2.3, the particle accelerates toward the HV conductor (b) as the Coulomb force overcomes the gravitational force acting on the particle. Upon reaching the vicinity of the HV conductor, the particle may induce a PD if its electric field strength exceeds the inception strength (c). The particle is then recharged with a different polarity and repelled to the ground electrode (d), where the PD and recharge processes begin again (g). [16]

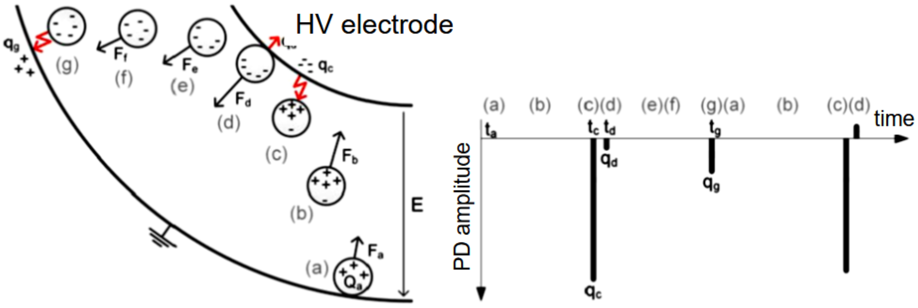

Figure 2.3: Schematic representation and PD magnitude graph of the bouncing motion in free metallic particle defects [16]

Firefly Effect Phenomenon

The particle tends to experience the firefly phenomenon at negative polarity. Once the electrostatic force overcomes the weight of the particle (a), as illustrated in Figure 2.4, the particle starts to move toward the HV conductor while its sharp edges locally enhance the electric field, generating PD activity (b). The enhanced field weakens as the particle approaches the HV conductor, and the PD magnitude decreases (c). If the particle touches the HV conductor, it behaves as a protrusion, causing a spike in PD activity (d). The charge release reduces the force affecting the particle, causing it to circle the HV conductor. If unbalanced, the particle may be expelled from the HV conductor (e), lose charge, and experience a decrease in the repulsive force (f), thereby reversing direction to repeat the process (c). [16]

P. Wenger et al. [31] provided an explanation of the mechanisms at play that enable firefly motion at a positively charged electrode and further asserted that firefly motion depends on the presence of space charge regions to recharge and redirect the free metallic particle back to the HV conductor.

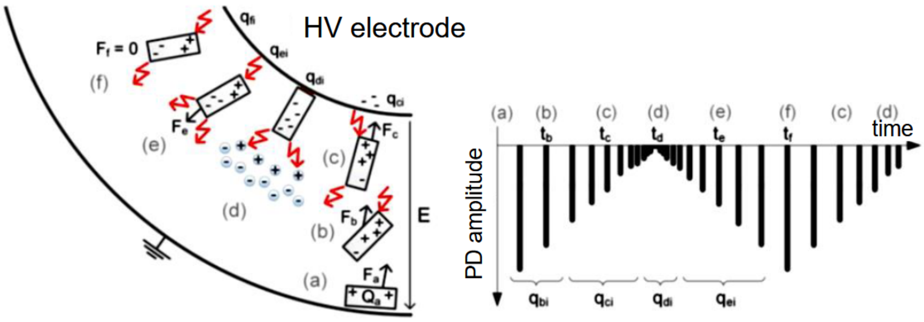

Figure 2.4: Schematic representation and PD magnitude graph of the firefly effect in free metallic particle defects [16]

As existing literature notes that certain particle geometries significantly influence the likelihood of specific particle motions, the choice of particle geometry is a crucial factor. The rationale behind the particle's design and characterization process is detailed in Section 4.1.2. With the fundamentals of PD mechanisms and defects established, the focus shifts to a detailed discussion of PD detection methods.

2.2. PD Detection Techniques

After establishing the fundamentals of PD mechanisms and defect behavior, it is equally important to understand the techniques for detecting PD pulses. Under operating voltage, protrusion and free metallic particle defects locally enhance the electric field in the surrounding insulating gas. PD activity is triggered when the electric field stress surpasses the critical breakdown threshold, producing a significant amount of charged particles in the form of electrons and ions. The resulting charge carriers, influenced by the constant electric field, generate a pulse current often accompanied by EM and acoustic emissions.

PD detection is commonly achieved through five primary methods: conventional, ultra-high frequency (UHF), ultrasonic, chemical, and optical [25]. Conventional and UHF methods are employed in this work to capture and analyze PD behavior.

2.2.1. Conventional Method

The IEC 60270 standard is the cornerstone of PD measurement, providing a framework for standardizing testing procedures across different locations, equipment, and operators to ensure repeatable and comparable results. While works such as P. Mraz et al. [30] offer clear guidelines for conducting PD measurements in compliance with this standard, they also highlight its limitations in fully integrating non-conventional techniques and the inherent challenges of these methods. The standard specifies that non-conventional methods are primarily used to gain insight into PD location rather than to measure the response of the test object, as is done with conventional methods. Furthermore, challenges arise from the complexity of calibrating non-conventional systems, often yielding inconsistent results, and the generation of multiple signals from a single defect, complicating interpretation and reducing measurement reliability. As a result, the IEC 60270 standard is often associated with and utilized in conjunction with the conventional PD method.

Compounding the challenges, the IEC 60270 standard, along with studies such as M. Hartje et al. [32], addresses the applicability of its procedures to DC voltage conditions and highlights several key differences from AC voltage measurements. The main difference lies in the lack of a phase angle to align the occurrence of PD pulses. Despite significant variations in noise levels, the absence of a clearly defined procedure for PDIV, and deviations in PDIV ranging from 50% to 80% in different lab conditions, the same testing procedures used for AC are often applied to DC. The measurement process can be aptly summarized into two distinct components: the measurement circuit and frequency band selection. Calibration is considered in the latter aspect.

Measurement Circuit

The measurement circuit in the conventional method is designed to capture the current generated by PD events. The two configurations, shown in Figure 2.5, are derived from the IEC 60270 standard and differ primarily in the positioning of the test object and coupling capacitor. The coupling capacitor, C_k, provides a low-impedance path for the high-frequency (HF) discharge current, while the blocking impedance, Z, prevents the HF PD signal from leaking into the power supply capacitance, thereby enhancing measurement sensitivity [30].

The sensitivity of PD measurement is largely determined by the ratio between the capacitance of the coupling capacitor and that of the test object, C_a. Larger coupling capacitors are generally preferred for increased sensitivity, with typical values ranging from 500 pF to 10 nF [26]. The IEC 60270 standard recommends a minimum value of 1 nF [33]. A common rule of thumb suggests that the coupling capacitor should have a higher capacitance than the test object. However, higher capacitance increases the load current demand on the power supply and results in larger discharge currents during breakdowns, necessitating protective measures for the measuring equipment [30].

The sensitivity of the PD measurement is further reflected in the choice between the two configurations. The parallel setup shown in Figure 2.5a is well-suited for test objects with low capacitance. Its effectiveness stems from the proximity between the test object and the measurement equipment, which enhances sensitivity. Conversely, the series setup in Figure 2.5b is the standard choice for test objects with higher capacitance. [26] While both setups support PD measurements under DC voltage stress, a dedicated DC voltage divider is required for voltage measurement as the coupling capacitor behaves as an open circuit in DC conditions [33].

The measurement circuit is incomplete without an appropriate PD detector to serve as the signal acquisition unit. The IEC 60270 standard stipulates that the PD detector must count PD pulses to account for their intermittent nature. In practice, PD signal acquisition is carried out by two separate units: the coupling device, CD, and the measuring instrument, MI. These components are discussed in further detail in Chapter 4.

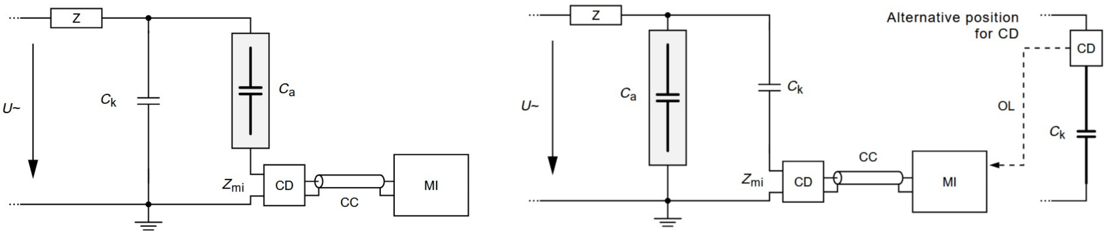

(a) Coupling capacitor C_k in parallel with measuring equipment **(b)** Coupling capacitor C_k in series with measuring equipment

Figure 2.5: Conventional PD measurement setups as defined by IEC 60270 [34]

Frequency Spectrum Selection

Selecting the appropriate frequency band for PD measurement is as critical as configuring the measurement circuit. P. Mraz et al. [30] propose a structured approach for frequency band selection. A preliminary step involves analyzing the noise spectrum, which typically includes random, switching, and sinusoidal noise. Familiarizing oneself with the prevailing noise level in the lab ensures more informed decisions in the subsequent process.

Since each PD event spans a broad frequency range, measurements can be taken at various frequencies. To standardize PD readings, the IEC 60270 standard specifies a defined wide-band frequency spectrum for PD detection, as outlined by Equation 2.1, Equation 2.2, and Equation 2.3, where f_1 denotes the lower frequency limit, f_2 represents the upper limit, and Δf is the total bandwidth [26]. For large test objects and those with large inductances, P. Mraz et al. [30] recommend measuring in the lower frequency range with the upper cut-off frequency, f_2, ranging from 200 to 300 kHz.

$$30kHz \leq f_1 \leq 100kHz \quad (2.1)$$
$$f_2 \leq 1MHz \quad (2.2)$$
$$100kHz \leq \Delta f \leq 900kHz \quad (2.3)$$

The wide-band frequency spectrum recommended by the IEC 60270 standard represents only a portion of the total PD frequency spectrum, as illustrated in Figure 2.6. Consequently, papers [20], [24] have argued that these bandwidth limitations can prevent some measurement systems from detecting the correct polarity of PD pulses or recognizing fast repetition rates in the case of glow discharge under DC conditions. Fortunately, advanced measuring equipment like the Omicron device used in this work can measure higher frequencies, while non-conventional methods offer an alternative method of PD detection [35].

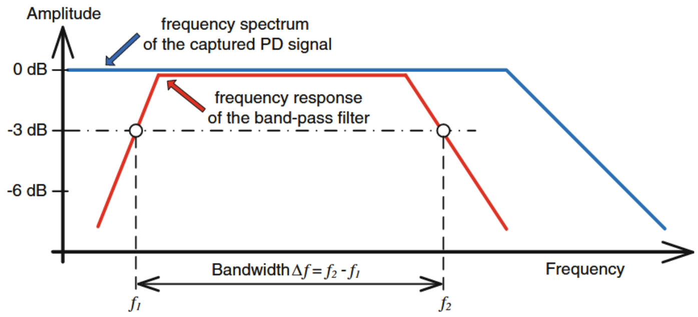

Figure 2.6: Comparison between the frequency spectrum of a PD pulse and the bandwidth recommended for PD measurements [26]

After the choice of the frequency range, the measurement setup has to be calibrated. A calibrator is directly connected across the test object terminals to inject a known charge, enabling the PD detector to determine the correct proportionality constant. The constant is denoted as the calibration factor in the results in Chapter 5. Calibration must be repeated whenever any component in the setup is altered to maintain consistent measurement levels. Common handheld calibrators produce charge magnitudes ranging from 5 to 100 pC [26]. Additionally, a linearity check is recommended to ensure consistent measurements and to detect potential irregularities. After calibration, the selected frequency range should be verified to ensure that the frequency response of the test object remains consistent between calibration and actual testing conditions. Otherwise, the frequency range must be adjusted, and the entire measurement setup recalibrated, as the calibration remains valid only for the specific frequency range for which it was originally performed.

With a detailed overview of conventional PD detection techniques complete, attention can now turn to alternative, non-conventional methods.

2.2.2. Non-Conventional Method

As the name suggests, non-conventional PD detection methods differ fundamentally from the charge-based detection of conventional methods. Among these, the UHF detection method, better known as radio frequency (RF) detection, operates by capturing the EM waves produced as a byproduct of a PD event. G. C. Stone et al. [36] adequately summarized the development of UHF sensors into the de facto standard for on-site PD measurement, owing to their high detection sensitivity, superior signal-to-noise (SNR) ratio, and defect directionality capability. These advantages arise from the interactions of several physical phenomena within GIS.

At frequencies exceeding 100 MHz, the skin penetration of EM waves is limited to just a few micrometers, allowing the metallic enclosure of GIS to effectively function as a Faraday cage. Additionally, since the typical dimensions of GIS exceed 1.5 meters, coupling between the PD signal and interference diminishes significantly above 200 MHz, enhancing the reliability of PD detection. These interactions are vital to the PD signal quality as GIS behaves poorly as a waveguide. Furthermore, each of the different transmission modes of the EM wave produces a unique intensity pattern, depending on the signal frequency. Thus, the placement of the UHF sensor relative to the PD source significantly influences the detection effectiveness. [36]

G. C. Stone et al. [36] further discussed the design and frequency response of UHF sensors used in GIS. Unlike traditional antennas, UHF sensors operate in the extreme near-field region due to their mid-band frequency, which tends to be around 1650 MHz, corresponding to an 18 cm wavelength. The sensor is placed deep into the GIS volume to maximize sensitivity and contains a large surface area, as illustrated in Figure 2.7. Intuitively, the larger surface area helps to capture the standing waves associated with the passing PD signals. However, these EM waves interact with all interior surfaces, resulting in complex interference patterns. Constructive interference appears as sharp peaks in the RF spectrum, whereas destructive interference manifests as sharp notches. The large size and HV nature of GIS also lower the cutoff frequency of the EM waves as the internal resonances manifest as longer wavelengths and, therefore, lower frequencies. Ultimately, the entire GIS can be modeled as a series of interconnected, frequency-dependent RF resonators and notch filters, where both standing wave behavior and resonance effects play critical roles in PD detection.

In practice, the UHF sensors, often built as capacitive couplers, are connected to an amplifier to boost the SNR ratio. A spectrum analyzer, digital oscilloscope, or specialized equipment then records the captured data. The exact setup of the UHF detection method used in this work is mentioned in Section 4.1.3.

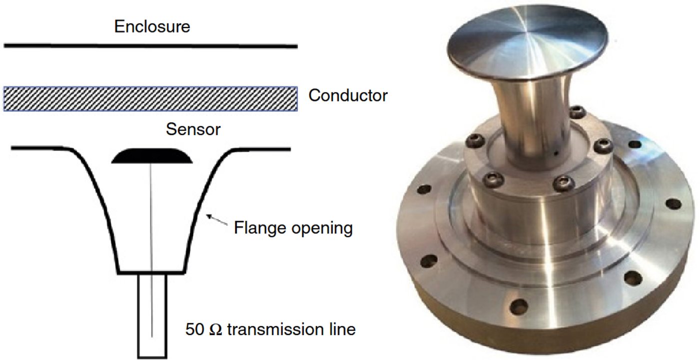

Figure 2.7: GIS electric field sensors with diagram (left) and example (right) [36]

As mentioned in the IEC 60270 standard, the calibration of the UHF detection method is not possible due to the significant variation in propagation loss between the PD source and the UHF sensor [36]. Rather, a sensitivity check is carried out that involves offsite and onsite measurements along with a frequency generator that imitates the actual defect. Unfortunately, the test cell provided for the experiments in this work has only one UHF port, so a sensitivity check could not be performed. Nonetheless, the UHF sensor provides invaluable information on PD activity that can be used to correlate with the captured data from the conventional method.

In the discussion of PD detection methods, noise and interference are always an issue. Even with the most optimal PD measurement equipment, PD pulses below 0.7 pC are generally not detectable without significant modifications to the test environment [20]. Conventional and non-conventional methods, therefore, complement each other and offer advantages and disadvantages to noise and interference rejection. UHF detection is the preferred choice but fails to capture the PD wave shape and charge magnitude. Conventional methods with their coupling capacitor are known for their high SNR ratio but exhibit inaccuracy for high repetition rates. Within the scope of the experiments, both methods are equally important in determining the PDIV, given the complexities of PD activity under DC voltage stress compared to AC.

2.2.3. PDIV Definition

Given the stochastic behavior of PD pulses under DC voltage stress, the precise mechanism of PD inception requires further investigation across various electrode-insulation configurations and operating conditions. U. Fromm [37] proposed the theory that two key intervals existed between PD pulses under DC voltage: the lag time and the recovery time. Lag time refers to the time necessary for a starting electron to appear, while recovery time represents the minimum period needed to dissipate a portion of the space charge generated by the preceding discharge before another PD event can occur. These intervals collectively lead to a near-zero repetition rate just above the PDIV as the ongoing PD activity hinges on recovering the electric field intensity after each PD event. This behavior contrasts with PD activity under AC voltage, where the PD repetition rate increases rapidly following each periodic polarity reversal due to its direct relationship with the external voltage.

To address the unclear PDIV guidelines in the IEC 60270 standard and the significant deviations in reported PDIV values highlighted by M. Hartje et al. [32], most studies adopt a practical approach to determining PDIV under DC voltage conditions. The PDIV is identified by gradually increasing the voltage across the test object from zero until a specified number of PD pulses per minute is detected. The threshold varies across studies, with typical definitions ranging from one to six pulses per minute [23], [24].

A graphical depiction of this stepwise voltage increase is shown in Figure 2.8, illustrating small voltage increments during the initial phase leading up to PDIV detection, followed by longer-duration steps for capturing sustained PD activity. To avoid artificially elevated PDIV readings, the duration of each voltage step must exceed the electrical time constant of the insulation system [16]. During testing, the applied voltage must surpass the PDIV to ensure a sufficient repetition rate for reliable measurement. Studies recommend applying voltage levels between 1.1 to 1.5 times the PDIV for accurate PD activity characterization [10], [12].

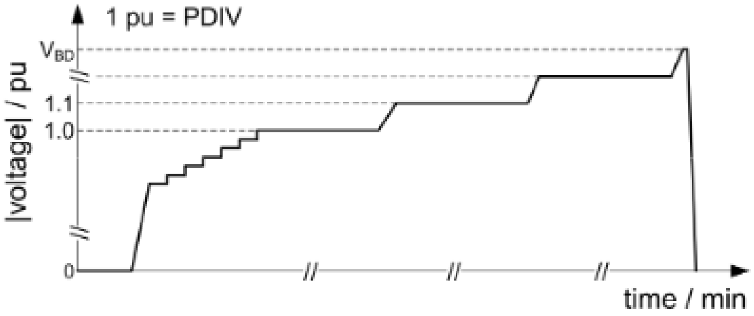

Figure 2.8: Graph of the voltage steps used to determine the PDIV [24]

The effects of voltage polarity and gas pressure on PDIV are well-documented, as detailed in section 3.1. The inherent differences in the mobilities of electrons and positive ions play a crucial role, resulting in a generally lower PDIV when a negative potential is applied to the electrode containing the defect. Under negative polarity, the electric field distribution intensifies at the defect tip as electrons, which are approximately 150 times faster than positive ions, are repelled by the negatively charged electrode. This movement of electrons initiates additional electron avalanches near the tip, accelerating the formation of streamers and partial discharges. In contrast, when a positive potential is applied, electron avalanches occur primarily within the insulating gas rather than at the defect tip. The slower-moving positive ions are repelled across the insulation gap, reducing the effective electric field near the tip. This charge redistribution diminishes the local field strength, inhibiting streamer formation and delaying PD inception. These mechanisms illustrate the asymmetric behavior of PDIV concerning voltage polarity. [38]

With the PD detection techniques covered, the intricacies of the analysis methods must be examined to validate the data obtained and achieve the correct defect identification.

2.3. PD Analysis Methods

This section addresses the tools and techniques available for analyzing PD activity under DC voltage stress. The consensus among most works is that no existing algorithm or method matches the defect identification capability of the phase-resolved partial discharge (PRPD) method used for AC voltage systems [36]. As DC voltage lacks a phase angle upon which the PRPD method explicitly relies, various studies have proposed several visualizing and evaluating methods with none definitively approved by the IEC 60270 standard [23], [24], [37]. More recently, advances in data processing have enabled the use of raw and preprocessed data from PD events to train machine learning models, thereby offering a promising direction for automated defect classification [39], [40]. These emerging techniques in neural networks are explored in brief in Section 3.4.1.

Regardless of the chosen representation method, two parameters are consistently extracted from PD events: the discharge magnitude, q_i, and the time of occurrence, t_i (or the time between discharges Δt_i). Voltage is often included as the third parameter. P. Morshuis et al. [23] provide a comprehensive overview of the graphical representations that can be derived from these parameters. Examples of pulse sequence analysis (PSA) include plotting the PD apparent charge magnitude as a function of time $q(t)$; the density function of the PD apparent charge magnitude $H(q)$, as illustrated in Figure 2.9; and the PD apparent charge magnitude and repetition rate as a function of test voltage among a few others. The shapes of these plots are used to build statistical distributions for particular defects to aid in identifying and classifying unknown ones.

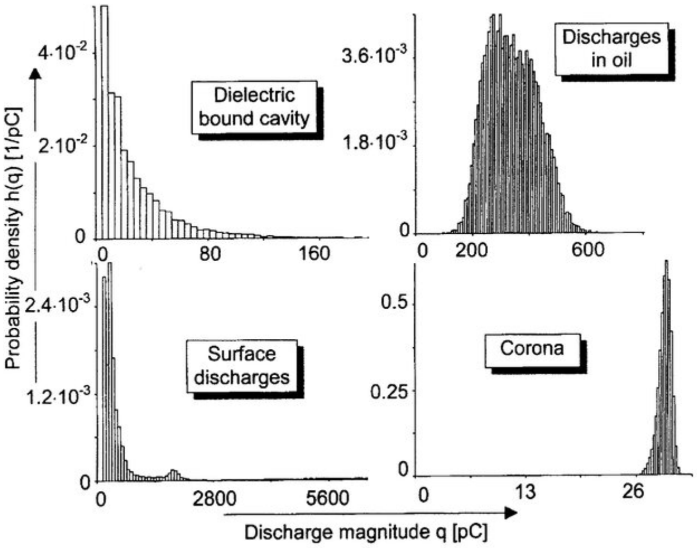

Figure 2.9: Density plots of the PD magnitude for four different defect types [23]

To enhance the defect classification process for human experts, the normalized differenced star (NoDi*) pattern was developed, utilizing the derived quantities introduced by U. Fromm [37]. This pattern is based on calculating the differences in the PD apparent charge magnitude, q, and arrival time, t, between consecutive PD pulses. The derived quantities are defined as follows [36]:

$$\Delta t_i(k) = t(k) - t(k-1) \tag{2.4}$$

$$\Delta t_{i+1}(k) = t(k+1) - t(k) \tag{2.5}$$

$$\Delta q_i(k) = q(k) - q(k-1) \tag{2.6}$$

$$\Delta q_{i+1}(k) = q(k+1) - q(k) \tag{2.7}$$

The four derived quantities can be computed and visualized using scatter plots with various horizontal and vertical axes combinations. The magnitude difference NoDi* pattern is the most commonly used, plotting Δq_i against Δq_{i+1}. Other configurations include the time difference NoDi* plot, using Δt_i and Δt_{i+1}, and the magnitude and time difference NoDi* plot, combining Δq_i with Δt_i [39]. The long-term study by T. Vu-Cong et al. [10] introduces an additional combination, as mentioned in Section 3.2.

Despite the differences in the axes, the overall scatter plot construction remains the same. As shown in Figure 2.10, the data points are distributed across a grid with evenly spaced units, where the axes are scaled to the real values of Δq and Δt. In machine-learning models, the standard 100-by-100 grid can be reduced to a 25-by-25 grid to improve efficiency without a decline in defect classification [39]. Each grid cell, or "stack," is normalized by dividing the count of pulses per minute by the total number of pulses within the stack, yielding the mean stack count per minute. This normalization allows for the comparison of NoDi* patterns across varying time durations and establishes a relation to the repetition rate of discharges. Furthermore, the stacks are color-coded using a logarithmic scale, enhancing visualization and emphasizing patterns. [24]

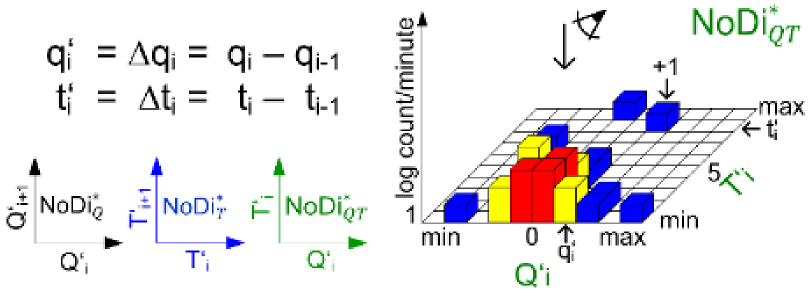

Figure 2.10: Underlying principle behind the NoDi* plots [24]

There are several compelling reasons why NoDi* plots were chosen as the preferred representation method for PD pulses in this work. First, the adoption of NoDi* plots aligns with existing research, which has already characterized the distinctive patterns associated with protrusion and free metallic particle defects. The completed characterization allows the findings in this work to be directly compared and properly evaluated. Secondly, the comprehensive long-term study by T. Vu-Cong et al. [10] demonstrated the superior effectiveness of NoDi* plots for identifying patterns in extended measurement periods, as they clearly illustrate the evolution of PD behavior over time. Finally, the pixel data of NoDi* plots are suitable for machine-learning models, which have achieved PD defect classification success rates exceeding 95% [39]. The specific NoDi* patterns used for comparison purposes in this work are detailed in Section 3.4.

With the theoretical foundation of PD activity established, the next chapter provides a concise literature review of existing studies.

3

Literature Review

This chapter explores the current developments in PD research across several key areas, including technical and synthetic air, long-term testing, free metallic particle defects, and defect identification. Advances have been made in these areas, and a clear overview was needed to ensure that this work contributed adequately to the ongoing research. The studies discussed in this section were chosen for their insights into the experimental process.

3.1. PD Research in Technical and Synthetic Air

PD research in dry air remains limited due to its inadequacy as a substitute for SF_6. This is attributed to its significantly lower dielectric strength and increased overall equipment dimensions, resulting from the higher filling pressure to match the performance of SF_6. Nevertheless, the lack of GWP makes it an attractive alternative for insulation purposes [11]. The scope of relevant literature narrows further when considering DC voltage stress. In their review of the current outlook on PD research under DC voltage in SF_6 and dry air, C. Li et al. [27] argued there is insufficient literature to accurately explain the mechanism behind PD phenomena in different scenarios. Nonetheless, works such as [12] have correlated PD characteristics, such as PDIV, PD apparent charge magnitude, and PD repetition rate, in technical air with physical properties, such as gas pressure, voltage polarity, and defect type. However, the paper by A. Pirker et al. carries over the inherent shortcomings of small-scale experiments. Due to the scale effect, the results might not be easily extrapolated to full-scale GIS [10].

Still, A. Pirker et al. [12] provide valuable insights into PD behavior under pressures up to 5 Bar. Using the data points shown in Figure 3.1, the authors made a few overarching conclusions on the effect of higher gas pressure. First, increased gas pressure corresponds to a rise in PDIV, as shown in Figure 3.1a, with polarity effects more pronounced in free metallic particle defects than in protrusions. Second, raising the gas pressure reduces the PD apparent charge magnitude and PD repetition rate, with the effect more profound in the positive polarity, as observed in Figure 3.1b.

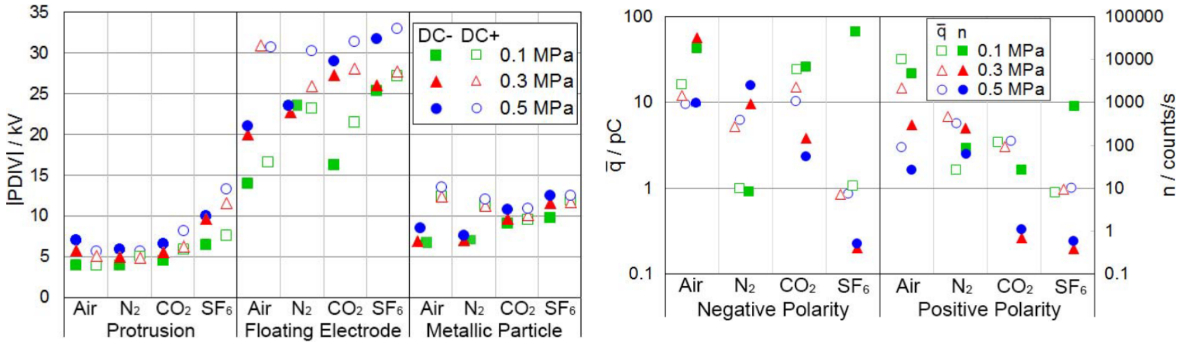

(a) PDIV under DC voltage with positive and negative polarity with different gas types and gas pressures

(b) Mean apparent charge $\overline{q}$ and repetition rate n of the protrusion at 1.1 PDIV at positive and negative DC voltage with different gases and gas pressures

Figure 3.1: Behavior of PDIV, PD apparent charge magnitude, and PD repetition rate at DC voltage with different defects under technical air among other gases at 0.1, 0.3, and 0.5 MPa [12]

To the author's knowledge, two studies have investigated PD activity in synthetic air under DC voltage inside a unit representative of full-scale GIS. While both conducted their experiments in a ±320 kV HVDC GIS unit, K. Juhre et al. [41] examined the free metallic particle defect at 6.5 Bar, contrary to the protrusion studied by H. Götz et al. [15] under 5 Bar. The latter confirmed the statement regarding the effect of gas pressure on PDIV by A. Pirker et al. [12]. However, both offered limited additional insights into trends regarding PD apparent charge magnitude, PD repetition rate, or defect pattern recognition. Instead, H. Götz et al. focused on current measurements as a promising technique for investigating PD behavior by comparing single PD impulses between SF_6 and synthetic air. Meanwhile, K. Juhre et al. used PD measurements to assess defect detectability and ultimately confirm the feasibility of synthetic air use in an HVDC GIS unit rated for ±320 kV.

Defect recognition in technical air remains a significant challenge. K. Juhre et al. [41] provided one of the few existing NoDi* patterns for defects in technical air, whereas most other studies, such as [24], tend to focus on defects in SF_6. A detailed discussion of these studies is presented in Section 3.4.

To expand on the findings of previous research [12], [15], [24], [41] and investigate potential correlations between NoDi* patterns in technical air and SF_6, this work conducted PD measurements on various defect types and at different gas pressures, at least during the preliminary test phase.

3.1.1. Considerations in Dry Air GIS

On a side note, the endeavor to replace SF_6 with dry air brings along certain challenges, specifically to the design of the GIS units. The higher filling pressures associated with dry air lead to a substantial increase in overall equipment dimensions. Manufacturers such as ABB and Siemens Energy have produced prototypes of ±320 kV and ±550 kV HVDC GIS but have inconsistent guidelines and unclear specifications for designing such insulators, necessitating further investigative efforts [42]. No definitive answer or literature study has been found that produced an exact percentage increase in the dimensions of individual GIS units solely due to the switch to dry air.

3.2. PD Research Regarding Long-Term Measurement

Alongside the scarcity of literature on PD measurements in technical and synthetic air under DC voltage, there is a fundamental lack of research on the long-term aspect. T. Vu-Cong et al. [10] provided an exception with their study that serves as the cornerstone of this work. In a full-scale ±320 kV HVDC GIS unit, the authors conducted repeated PD measurements on a protrusion defect subjected to SF_6 and SF_6 alternative gases, C_5FK–dry air and C_4FN–CO_2. It is important to note that the voltage application duration was inconsistent among the different gas types, ranging from seven to twenty days in certain test scenarios, as observed in Figure 3.2.

Using conventional methods of PD measurement, T. Vu-Cong et al. [10] produced the results presented in Figure 3.2 and Figure 3.3, highlighting trends regarding PD apparent charge magnitude and repetition rates for the three insulating gases in question. As observed in Figure 3.2, the PD apparent charge magnitude consistently increased with the voltage application time, irrespective of the gas type or polarity. The initial rise was relatively steep during the first few days, after which stabilization occurred. The stabilization time, however, depended on the specific gas and voltage polarity and ranged from three to ten days in some cases. Likewise, the repetition rate depended on the gas type and voltage polarity and either increased or decreased before stabilizing at the same point as the apparent charge.

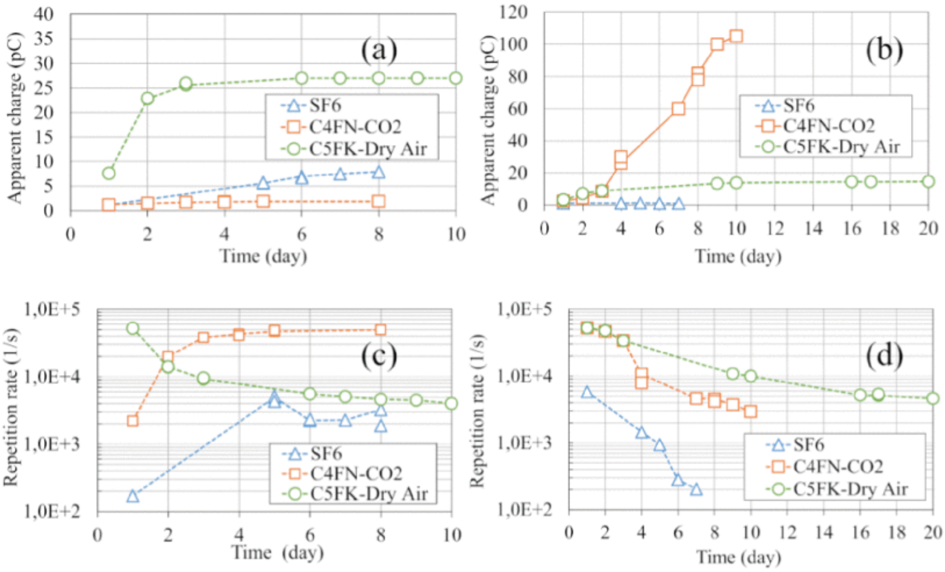

Figure 3.2: PD evolution as a function of voltage application time for SF_6, C_5FK–dry air, and C_4FN–CO_2; [a] and [b] represent PD apparent charge magnitude; [c] and [d] indicate PD repetition rate; [a] and [c] express negative polarity; [b] and [d] express positive polarity [10]

The data presented in Figure 3.2 was further analyzed using NoDi* plots, as illustrated in Figure 3.3, to aid defect recognition. These plots captured the PD activity at specific timestamps, offering a glimpse into the PD evolution over time. T. Vu-Cong et al. [10] improved upon the standard array of magnitude and time difference combinations by introducing a weighted PSA set, $\Delta q_i/\Delta t_i(\Delta t_i)$. The proposed addition aimed to better distinguish between PD activities with similar physical characteristics, such as corona and surface discharges.

The NoDi* plots in Figure 3.3 exhibited the same trends observed in Figure 3.2, where the PD apparent charge magnitude increased at the expense of the repetition rate. More notably, the PD pattern recorded on day eight in the C_5FK–dry air mixture resembled the pattern reported by K. Juhre et al. [41] for the standing motion of a free metallic particle defect in technical air, as shown in Figure 3.6a.

This similarity supports two key arguments. First, it reinforces the conclusion by T. Vu-Cong et al. [10] that the dominant factor influencing PD activity is the buffer gas, technical air, rather than C_5FK. Given that C_5FK constitutes only 10% of the mixture, the long-term study serves as a more direct comparison to the results of this work. Second, the resemblance between the NoDi* pattern of the protrusion defect and the standing motion pattern suggests the possibility of misidentification, warranting further investigation. This issue was also observed in this work and is further examined in Section 6.3.

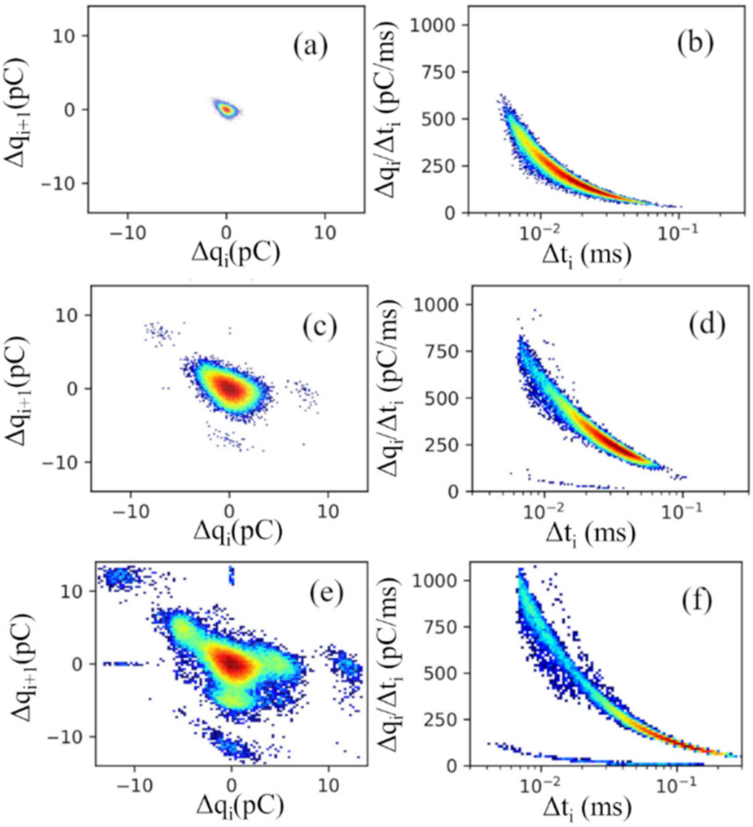

Figure 3.3: PSA plots of C_5FK–dry air with the protrusion defect under +150 kV DC timestamped at initial day [a,b], day three [c,d], and day eight [e,f]

To explain the observed increase in PD apparent charge magnitude over time, T. Vu-Cong et al. [10] tested two hypotheses. The first focused on changes in the gas composition near the protrusion tip, attributed to the generation of decomposition byproducts during prolonged voltage application. To test this, the experiment involved interrupting the voltage for several days to allow gas recombination and, in a separate instance, replacing the existing gas. Despite these actions, the PD apparent charge magnitude remained at levels observed before the voltage interruption and gas exchange, indicating that gas composition alone was not the main contributing factor.

The second hypothesis centered on physical changes to the protrusion defect itself. Visual inspection before and after prolonged voltage application revealed erosion, material deposition, and an increase in the tip radius from the initial 25 μm to 40-50 μm, depending on the gas type. Since active volume is directly related to PD apparent charge magnitude, COMSOL simulations were used to verify that an increase in tip radius corresponds to a larger active volume, peaking in the 40-50 μm range, as shown in Figure 3.4a. Thus, the increase in PD apparent charge magnitude was attributed to the change of the protrusion tip radius rather than specific gas properties or composition. Conversely, the overall reduction in the repetition rate was credited to the diminished electric field stress at the eroded tip, making electron avalanche initiation more difficult. [10]

Fixated on the change in the tip radius, T. Vu-Cong et al. [10] modeled the progression using Equation 3.1 and validated the theoretical curve with experimental measurements of the tip radius before and after prolonged voltage application, as depicted in Figure 3.4b. In this equation, $r(t)$ is the tip radius in micrometers at a given point in time; C is the constant that depends on the test conditions and protrusion material; t is the time in hours. The constant, C, must be derived for every new test condition, given the complex dependencies of the electric field on space charges, polarity, and gas nature.

$$r(t) = C \cdot \sqrt[3]{t} \tag{3.1}$$

The theoretical curves displayed in Figure 3.4b offer key insights into the erosion mechanism. The growth rate was relatively high in the first few days and progressively decreased in the following days. This evolution of the tip radius coincided with the observed increase in PD apparent charge magnitude and subsequent decrease in PD repetition rate [10].

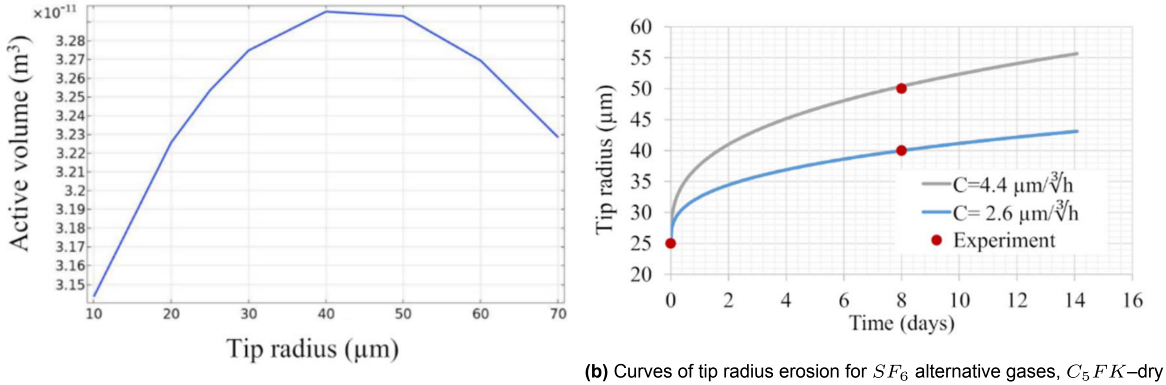

(a) Active volume as a function of protrusion tip radius for SF_6 using COMSOL simulation

(b) Curves of tip radius erosion for SF_6 alternative gases, C_5FK–dry air and C_4FN-CO_2, based on analytical data points and validated by experiments

Figure 3.4: Investigation into tip radius progression over time and resulting change in active volume size [10]

Additional key factors in the long-term study included the length and material composition of the protrusion. The study [10] acknowledged that the protrusion length was relatively long compared to typical defect sizes in GIS units. Furthermore, tungsten was selected as the protrusion material when, in reality, defects are often composed of weaker materials. These softer metals are more prone to erosion, which would significantly influence the erosion rate and subsequent PD behavior over time.

This work extended the long-term investigation by T. Vu-Cong et al. [10] twofold. First, tungsten was replaced with aluminum to represent real-world scenarios. Second, this work used a metallic particle as the protrusion defect and placed it on the ground electrode rather than the HV conductor to examine possible correlations. Using the metallic particle further aided in investigating the similarities between the NoDi* patterns of the protrusion defect and the standing motion of the free metallic particle defect.

Regarding metallic particles, existing literature tends to focus primarily on their role in free metallic particle defects. As no equivalent long-term study exists, these papers serve rather to expand upon the dependencies of PD phenomena and particle motion on particle geometry and test conditions in non-uniform electric fields.

3.3. Research into Free Metallic Particle Defects

Research into PD behavior related to free metallic particle defects under DC voltage has been extensively covered in studies [13], [22], [43], [44]. Among them, works [12], [16], [39]–[41], [45] have specifically explored the thresholds and conditions under which the bouncing and firefly phenomena occur. A. Pirker et al. [24] conducted a comprehensive analysis detailing the occurrence likelihood for specific particle types. For instance, spiral particles tend to exhibit the firefly behavior under low-pressure environments with negative polarity, transitioning to the bouncing behavior under positive polarity. Increasing the gas pressure eliminates the firefly effect entirely. Conversely, rounded particles, such as ball bearings, consistently perform the bouncing motion from lift-off voltage to BDV, regardless of the voltage polarity and pressure. The findings align with the summary of works by C. Li et al. [27], which confirmed that the bouncing behavior is more prevalent in rounded particles, followed by the firefly phenomenon in sharp-edged particles.

Unlike any of the previously mentioned works, P. Wenger et al. [46] provided a more detailed classification within the firefly motion by identifying three distinct modes: vertical hopping with either small or large jumping amplitudes, wobbling with small or large jumping amplitudes, and levitating firefly. The authors elaborated on the specific particle behaviors associated with each mode and stressed the impact of the space charge regions on the PD apparent charge magnitude. The study demonstrated that subtle variations in the motion of the free-moving particles can be effectively distinguished by combining UHF pulses and high-speed imaging with the PSA method, as illustrated in Figure 3.5. The insights from the study, particularly the relationship between PD pulses and particle motion in the time domain, are later applied in this work to distinguish between the different firefly motion patterns effectively. Additionally, the paper mentioned that for lamella particles, such as aluminum shavings, the increase in the tip radius over other particle types leads to a more homogeneous field distribution, less PD activity, and a less pronounced space charge region. Although the experiments in the study were conducted in SF_6, the fundamental particle motions and underlying principles remain unchanged. However, differences in PD apparent charge magnitude, PDIV, and PD repetition rate are expected, as empirically confirmed by A. Pirker et al. [12] in Figure 3.1.

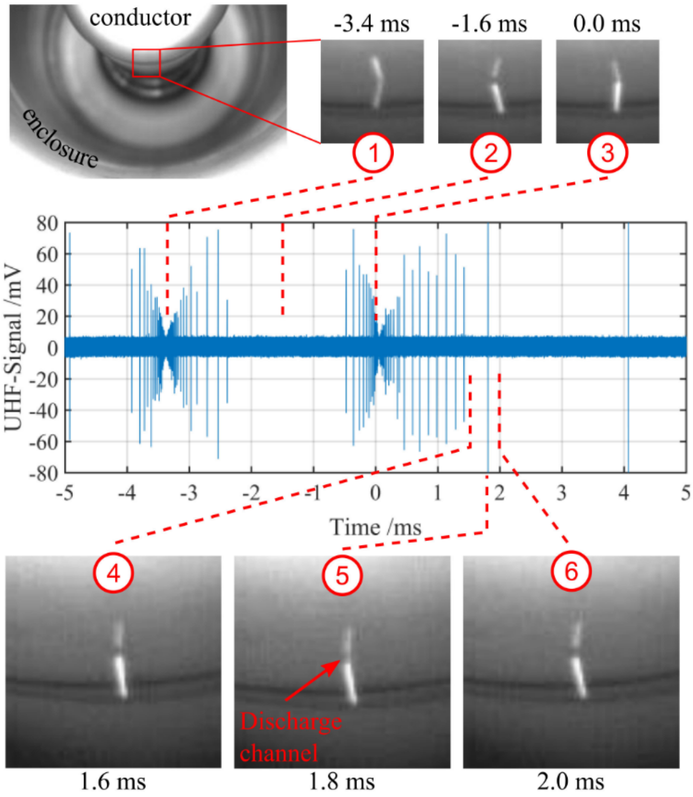

Figure 3.5: Correlation of the particle motion and UHF PD pulses from a 4 mm wire-shaped particle during large jumping firefly motion at U_{DC} = −230 kV [46]

While most papers agree on the conditions for the firefly and bouncing behavior, discrepancies exist regarding metallic particle size. Metallic particles examined include wires, ball bearings, and spiral and lamella-shaped particles. Works [12], [13], [24], [25], [39], [41], [43], [44], [47] disclose information on particle dimensions. Rounded particles generally range from 1 to 4 mm in diameter and are primarily made of steel. Likewise, spiral and lamella-shaped particles vary from 1 to 5 mm long and are composed of aluminum or steel. Wire particles are typically 1 mm in diameter and differ by 1.5 to 4.5 mm in length. To the author's knowledge, T. Berg et al. [45] was the only study that explicitly justified their choice of spiral particles up to 4 mm long, citing them as representative of most particles found in HVDC GIS systems. Other studies lacked such justification, instead resorting to an assortment of metallic particles to analyze the resulting PD behavior or standardizing their particles by weight [46].

Not all papers focus on PD activity when investigating free metallic particles. Many researchers have dedicated considerable effort to understanding the movement characteristics of free metallic particles in non-uniform electric fields. Among them, J. Sun et al. [47] examined the effect of the electrode configuration inhomogeneity on the horizontal force acting on free metallic particles within a GIS system. Particle collisions with the HV conductor increase the particle charge and the horizontal force component, ultimately driving the particle to overcome the influence of the electric field and escape its control. The termination position, or the location of the particle's final collision with one of the electrodes, is influenced by the electrode spacing and the radius curvature of the HV conductor.

The study by J. Sun et al. [47] highlights a significant challenge with ball electrode configurations compared to GIL setups: particle contamination. In non-uniform electric fields, particles are often ejected from the electrode region, ending up in a final position that may be difficult to access or observe. In contrast, GIL configurations tend to have a uniform electric field along the length of the HV conductor and rely on an injector apparatus to introduce particles after the desired voltage is applied [41]. Various containment methods have been explored in ball-electrode experiments to mitigate these challenges. Studies [36], [43], [44], [48] have employed stainless steel lids, wire leashes, and glass containers. The wire leash, in particular, ensured that the firefly particle motion was achieved by preventing contact with the HV conductor. Unfortunately, the leash material led to charging and tangling, significantly affecting particle motion. Additionally, multiple particles have been tried in similar setups to advance research on particle dynamics and PD behavior [45].

Aiming to address the lack of long-term analysis concerning free metallic particle defects, such particle containment measures are needed in this work to allow for repeated particle motion. The particle contamination setup employed in this work is explored in detail in Section 4.1.2. With the research on free metallic particle defects addressed, the current state of defect recognition is presented, including the corresponding NoDi* plots and a concise overview of machine learning models implemented in academic research.

3.4. PD Research Concerning Defect Recognition

Research into PD defect classification has seen renewed interest due to the integration of HVDC technology into modern energy grids. Much to the credit of PD measurements under AC voltage, the physical phenomena behind PD processes in DC voltage conditions are fairly understood. Repeated experiments have properly cataloged the expected values for the PD apparent charge magnitude associated with protrusion and free metallic particle defects, ranging from 1 to 100 pC. [16] However, significant challenges remain as the IEC 60270 standard emphasizes the lack of meaningful testing and acceptance criteria for assessing HVDC components.

One approach lies in the PSA methods that include density functions for parameters such as t_i, q_i, Δt, and Δq, along with their relationships to successive values, as visualized through NoDi* patterns. Another approach more tailored towards machine learning algorithms is using statistical techniques that involve extracting features such as variance, skewness, and the scale parameter of the Weibull function. Despite the clear differences in the NoDi* patterns between defects and the high success rate of trained machine models, the status quo regarding the guidelines on PD measurements under DC voltage has remained unchanged. [24], [39]

The available compendium of NoDi* patterns spans a wide array of test parameters, including voltage polarity, gas pressure, gas type, and electrode configuration, all of which influence the applicability of the datasets. Among these, gas type and electrode configuration are particularly crucial. To the author's knowledge, K. Juhre et al. [41] provided the only NoDi* pattern for a defect tested in synthetic air within a full-scale GIS unit, as depicted in Figure 3.6a. Unfortunately, this NoDi* plot provides only information on the standing motion of a free metallic particle and relies on data from a UHF PD sensor rather than the conventional method.

In contrast, other studies, such as those by A. Pirker et al. [24], explore the bouncing and firefly motions of particles, as shown in Figure 3.6b. However, these studies utilize SF_6, different particle types, and small-scale electrode configurations. Despite these differences, the NoDi* patterns effectively highlight the distinctions between bouncing and firefly motions. The authors also underscored the overlap in patterns across particle types, such as wires and spirals, emphasizing the challenges in achieving unambiguous defect classification. Likewise, they mentioned that at positive polarity and low gas pressures, the firefly effect alternates with the bouncing motion on the ground electrode, which marks a departure from the findings reported in other, more established works, such as [16].

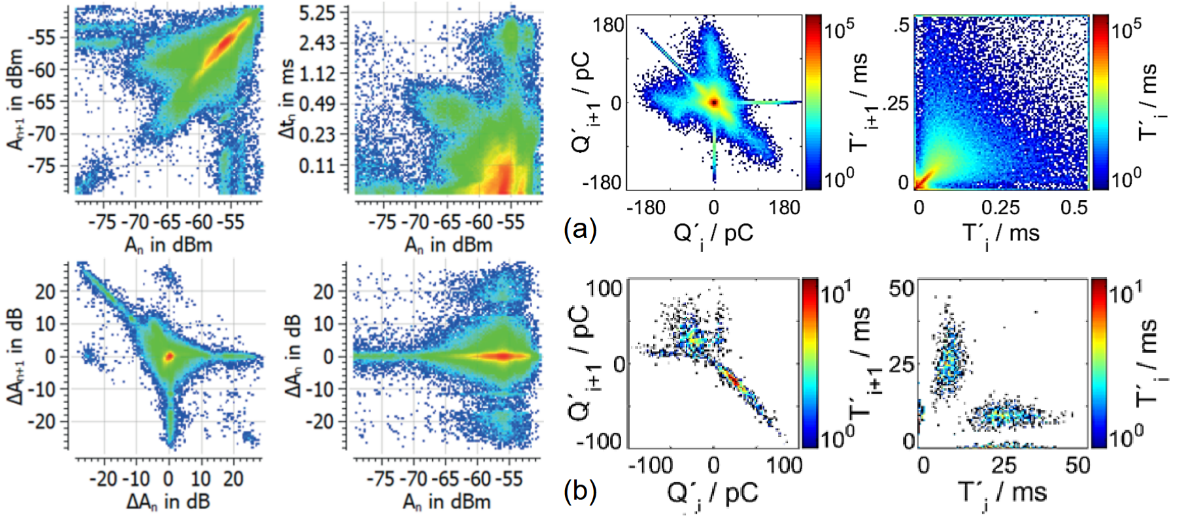

(a) PSA plot for standing motion of 4 mm moving particle at -268 kV in clean air under 0.65 MPa of pressure [41]

(b) NoDi* pattern of 2 mm long spiral particle in SF_6 in firefly (a) at -30 kV under 0.2 MPa and bouncing (b) at 25 kV under 0.6 MPa [24]

Figure 3.6: PSA plots on the three main phenomena experienced by free metallic particle defects under DC voltage stress: standing (a), and bouncing and firefly (b)

As defect patterns vary significantly, even among similar defects, it is vital to develop a comprehensive database to establish characteristic features and create a reliable tool for distinguishing between them. Several works [22], [39], [40], [48] have implemented and compared various machine-learning algorithms, including neural networks, decision trees, and support vector machines. The following section briefly discusses these approaches and their respective success rates.

3.4.1. Machine Learning Methods

Artificial neural networks were initially considered as a tool to analyze the NoDi* plots generated in this work, aiming to evaluate the impact of long-term data on defect classification. However, the literature review uncovered the study by M. Dalstein et al. [48] in particular. The authors revealed that classification methods such as k-nearest neighbors, support vector machines, and logistic regression experienced a significant drop in accuracy from 95% to as low as 2% when not trained on long-term data. Conversely, other works, such as [39], demonstrated that machine learning models could achieve accuracy upwards of 90% using a variety of inputs, including raw PD pulse data, statistical parameters, and pixel data from NoDi* plots, without a notable performance loss in algorithms such as artificial neural networks and decision trees. Additionally, studies like [40] have compiled extensive datasets of PD measurements from typical defects to train these classification methods effectively.

Given these advancements, this work refrains from future endeavors into machine learning models and continues to focus on expanding the collection of PD measurements in technical air. The following section will discuss the methodology employed in this work.

4

Methodology

This chapter covers the essential steps in setting up the test cell, PD measurement equipment, and other aspects of the measurement procedure. Key intermediate steps, such as defect fabrication, PD calibration, and gas filling, are briefly covered to provide a comprehensive overview of the preparation process. Lastly, the chapter addresses the analytical tools used to assess and classify the defects.

4.1. Test Setup

The HVDC test setup underwent several iterations before reaching the final configuration, as depicted in Figure 4.1. Due to delays in the delivery of the GIS test cell, initial experiments were conducted using small-scale setups with rod-plane and rod-bowl configurations, as detailed in Appendix B, to develop a deeper understanding of the PD measurement procedure. Once Siemens Energy delivered the GIS test cell, the assembly of the full-scale setup began. As shown in Figure 4.1, an HVDC test setup compliant with the IEC 60270 standard was constructed to investigate PD behavior associated with protrusion and free metallic particle defects within GIS.

Voltage generation was achieved using a self-contained HVDC source with polarity reversal capability, eliminating the need for voltage rectification, as further discussed in Section 4.1.4. A 1 MΩ resistor was placed between the HVDC source and the test circuit to protect the source, suppress switching noise, and block incoming PD current pulses, as recommended by the study [30].

The PD measurement system comprised the Omicron MPD 800 and UHF 800 measurement systems. The UHF 800 setup was relatively straightforward, involving a direct connection to the UHF port of the GIS test cell. However, the conventional measurement method using the Omicron MPD 800 required additional components. A 100 pF coupling capacitor was connected in series with the CPL1 quadripole to accommodate the large capacitance of the GIS test cell. Furthermore, a voltage divider with a 280 MΩ resistor was implemented to facilitate voltage measurements, as capacitors behave as open circuits under DC voltage. Both PD detection methods are discussed in detail in Section 4.1.3.

The schematic in Figure 4.1 further distinguishes the test setup by defining an HV area, corresponding to the section of the test setup under HV potential. The HVDC source was situated outside the HV area, owing to its self-contained nature as illustrated in Figure 4.10 and Figure 4.11. The single-device solution allowed for smooth operation without the need for power transformers to ramp up the voltage and featured direct and remote control by the operator. The Omicron MPD and UHF 800 devices were interfaced with an external computer via the MCU2 device using optical fiber cables. Safety precautions were also taken to prevent personnel from entering the HV area during live experiments, as outlined in Section 4.2. One of the numerous safety measures is immediately evident in the schematic with the 10 MΩ resistor in series with an automatic grounding unit to ensure the proper discharge of capacitance in the system.

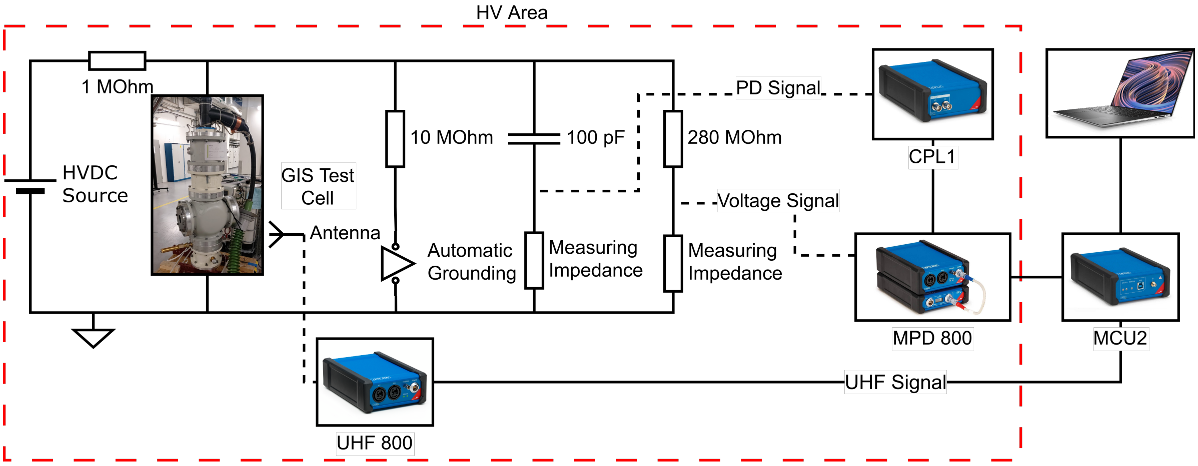

Figure 4.1: HVDC test setup diagram for PD detection using Omicron MPD 800 and UHF 800

To clearly define the HV area and shield the test setup from external EM interference, the entire setup was housed inside a Faraday cage, as shown in Figure 4.2. The Faraday cage was situated in the cell-divided lab belonging to the Department of Electric Energy, providing ample space to accommodate the GIS test cell and the necessary equipment to perform HV experiments.

The GIS test cell was strategically placed in a corner of the lab to allow proper suspension and support of the bushing. A simple piece of twine was wrapped around a wooden crossbeam and fastened to the lowest point in the bushing. Likewise, the terminal of the GIS test cell bushing was connected to the rest of the measurement circuit through an additional pillar to maintain level alignment and reduce electric field concentrations. The added height also increased the distance between the HVDC source and the GIS test cell bushing terminals. Moreover, sufficient clearance was maintained on either side of the test circuit to meet the minimum breakdown distance requirement.

A mounting bracket was installed for the gas canister, and a server rack was provided to house the necessary HV equipment. Likewise, the optical fiber cables were routed overhead to the operator desk to minimize tripping hazards.

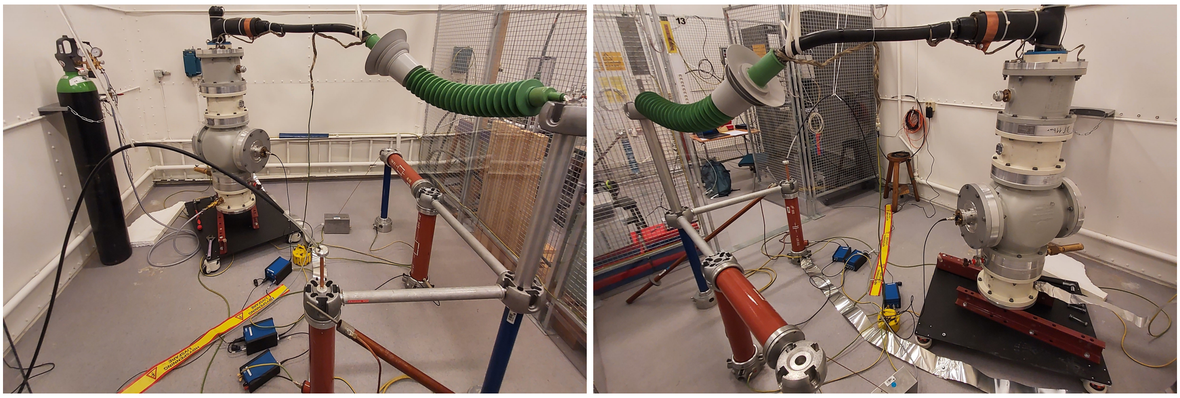

(a) Front view

(b) Backside view

Figure 4.2: Pictures of the final test setup used for the long-term tests with both Omicron MPD 800 and UHF 800 visible

The ambient noise level was a constant challenge throughout the entire experiment phase. The location of the test setup meant that interference from other ongoing experiments affected the readings from the highly sensitive PD detection equipment. Furthermore, noisy power supplies and improper grounding techniques contributed to the initial noise reading of 6–7 pC. To address these issues, several modifications were implemented, including replacing the noisy power supplies and improving the grounding connections with aluminum foil, as illustrated in Figure 4.3. These adjustments successfully reduced the noise floor to approximately 0.2 pC with the HVDC source at idle.

As recommended, the aluminum foil was directly connected to the grounded Faraday cage for both the coupling capacitor and the GIS test cell. This approach created a lower impedance path due to the skin effect and mitigated ground loops, which would otherwise interfere with the PD measurements. Likewise, the grounding stick was directly connected to the Faraday cage to avoid transferring discharge currents to other parts of the test circuit.

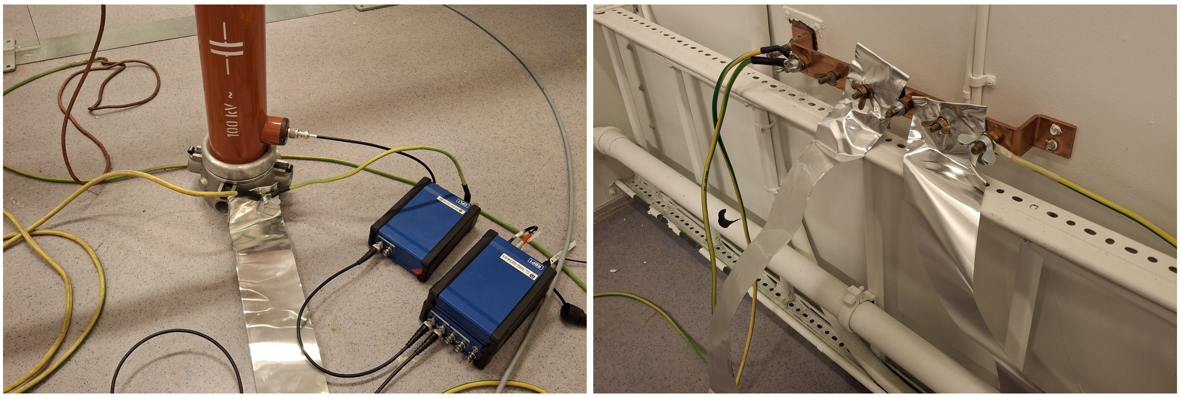

(a) Configuration of the ground connection with the coupling capacitor **(b)** Configuration of the ground connections to the Faraday cage

Figure 4.3: Pictures of the implementation of the aluminum foil to lower the noise level and improve PD sensitivity

The following sections delve deeper into the individual components of the test setup, beginning with the GIS test cell and expanding outward to encompass the surrounding systems and components.

4.1.1. Test Cell

As part of the EU Project Mission, Siemens Energy supplied the GIS test cell shown in Figure 4.4. The specifications provided by Siemens Energy are as follows:

- Maximum AC Voltage: 72.5 kV
- Maximum DC Voltage: 100 kV
- PD free up to 87 kV
- Lighting Impulse: 325 kV
- Maximum pressure of 15 Bar absolute

While the maximum pressure rating posed no issue, the maximum operating DC voltage, unfortunately, fell short of those levels associated with HVDC. Nevertheless, the GIS test cell enables long-term testing and full-scale functionality utilized by other works.

The GIS test cell has several features, including the aforementioned terminal bushing for external connections, an antenna port for UHF PD capture, a viewing window for optical cameras, a valve for gas filling, and a safety valve to prevent explosive decompression. The unit was mounted on a wheeled platform, which could be secured in place using rubber stoppers. As outlined in the handbook by Siemens Energy, special handling procedures were followed to ensure the integrity and longevity of the equipment. Gloves were worn at all times to prevent contamination of the interior with bodily oils. Additionally, the rubber seal was inspected after every opening to ensure it was adequately lubricated to extend its lifespan. Before pressurization, the screws were tightened to 70 Nm to ensure an airtight seal.

The technical drawing of the electrode configuration is provided in Figure 4.5 and consists of a ball and plane electrode, similar to the ones tested by J. Sun et al. [47], with both the radius of curvature and gap distance at 50 mm. Both electrodes have threads inside to allow for easy removal if another electrode shape is desired.

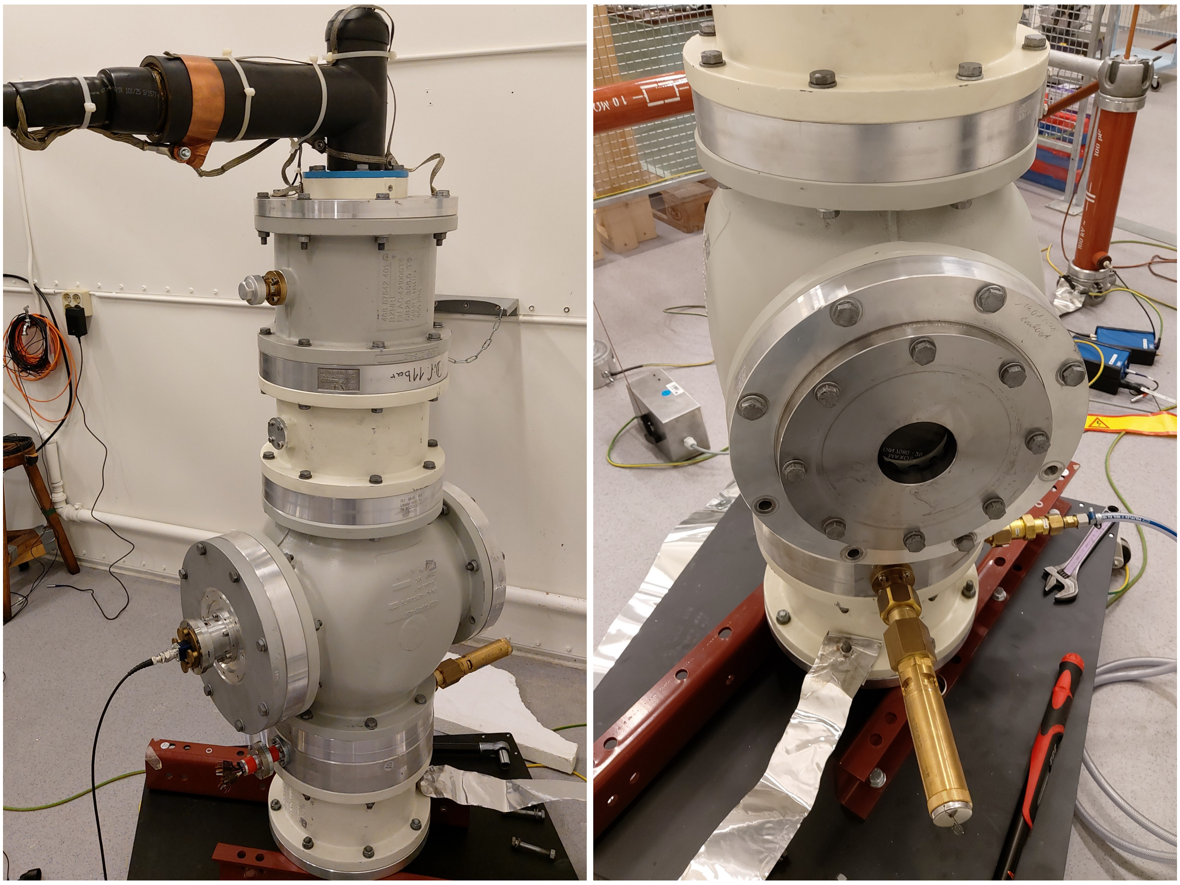

(a) View of the HV bushing and the antenna port connection

(b) View of the viewing window and safety valve

Figure 4.4: Closeup pictures of the GIS test cell provided by Siemens Energy

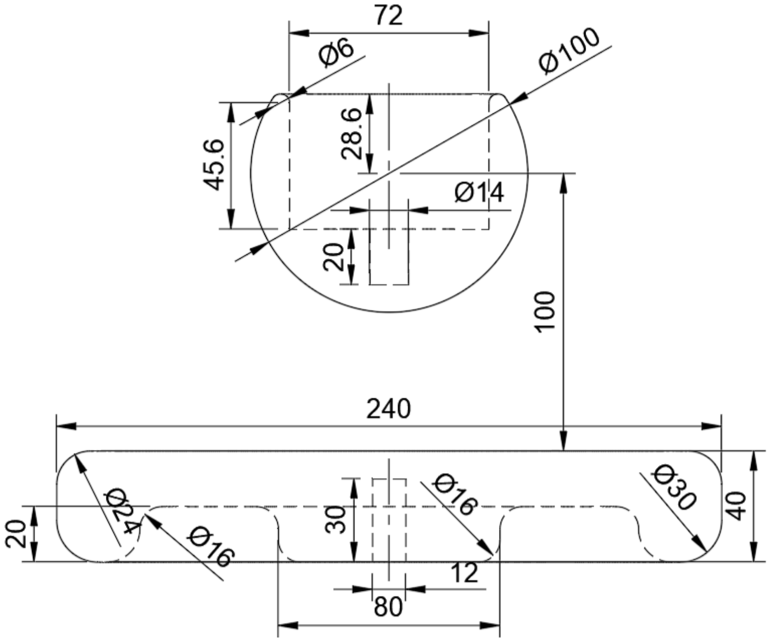

Figure 4.5: Technical drawing of the electrode configuration with 50 mm gap distance

After tightening the screws, the GIS test cell was filled with gas using the built-in gas valve, as illustrated in Figure 4.6b. The gas flow was controlled using a pressure regulator, shown in Figure 4.6a. Siemens Energy recommended incorporating a precision manometer between the gas regulator and the filling connection of the GIS test cell to ensure accurate pressure monitoring. However, since the test pressure for these experiments did not exceed 3 Bar absolute, the provided pressure regulator was deemed sufficient for the gas-filling process. The decision to test at significantly lower pressures than the industry trend of 11 Bar absolute was attributed to pressing time constraints and further addressed in Section 6.4.

Discussions with Siemens Energy addressed concerns regarding potential ozone production due to the high electric field concentrations. The well-ventilated lab environment and the availability of ozone sensors alleviated these concerns. As a result, it was deemed safe to release the gas into the lab space upon the completion of each experiment.

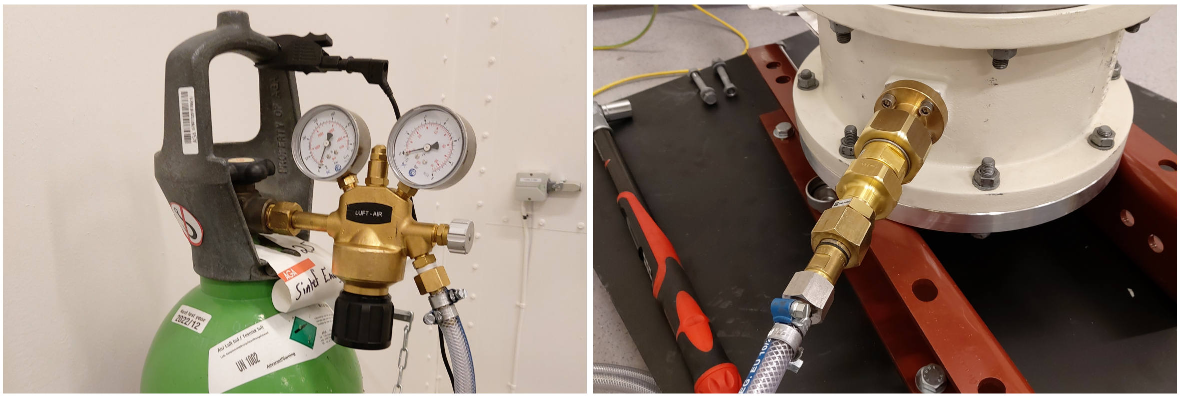

(a) Gas canister filled with technical air and connected to the GIS test cell with pressure regulator

(b) Gas filling connection of the GIS test cell with a manual closing valve to isolate test environment

Figure 4.6: Pictures of the technical air-filling setup

After addressing the foundational aspects of the GIS test cell, the following section will delve into the specific defects tested within its confines.

4.1.2. Defect Characterization

The characterization of the two defect types utilized in this work proved to be rather intricate, owing to the multitude of variables, including materials, geometries, and dimensions, as well as the complex interplay of different phenomena, such as electric field concentrations, space charge accumulation, and decomposition byproducts. To navigate these complexes, the flow chart shown in Figure 4.7 was developed to catalog the interactions and dependencies, ultimately providing a framework to analyze how PD activity and PDIV are influenced. Certain elements, such as the electrode configuration and the voltage applied across the gap distance, are constant. Likewise, two feedback loops were present: erosion at the defect tip from the electrochemical etching of the decomposition byproducts in the insulating gas affected both the tip radius and overall defect height, resulting in a change in the electric field concentrations.

The flow chart applies to both defect types, though certain correlations, such as the relationship between the liftoff voltage and protrusion defect, are not immediately evident. Initially, the protrusion defect was intended to be fabricated directly into the HV conductor by drilling a hole and inserting an industrial-grade needle. However, after further consideration, permanent modifications to the electrode configuration were deemed impractical. Instead, a metallic particle was bent and taped to the ground electrode to simulate the standing motion of a free metallic particle defect, effectively mimicking a protrusion defect. Consequently, determining the appropriate height of the protruding particle became a crucial aspect of the setup for the protrusion defect.

Here, the liftoff voltage and particle mass come into play for both defects. Previous studies have explored various particle types, including wire, spiral, and rounded shapes. Of all the possible candidates, the choice came down to the lamella-shaped aluminum shavings produced as a byproduct of CNC machining. These strands exhibit uneven thickness and surface roughness, resembling the particles formed through the abrasion between different components in a GIS system. The long aluminum strands have a uniform width and were cut to various lengths to create test particles. As liftoff is achieved when the Coulomb force acting on the particle exceeds the gravitational force, the particle should be sufficiently light to enable such motion, given the voltage applied. Likewise, it is crucial to maintain a margin between the liftoff voltage and the operating voltage to ensure continuous particle motion for effective PD measurement.

Since the liftoff voltage varies significantly across different test setups, a particle length of 4 mm was selected as a starting point to determine the liftoff voltage empirically, as further explored in preliminary test runs in subsection 5.2.1. This choice aligned with the findings of T. Berg et al. [45], which indicate that 4 mm is a commonly observed particle length in free metallic particle defects in GIS. Thus, the bent particle in the protrusion defect was set to a height equal to the final length of the free metallic particle to replicate the standing motion. The final height used for the particle in the protrusion defect is covered in Section 5.3.

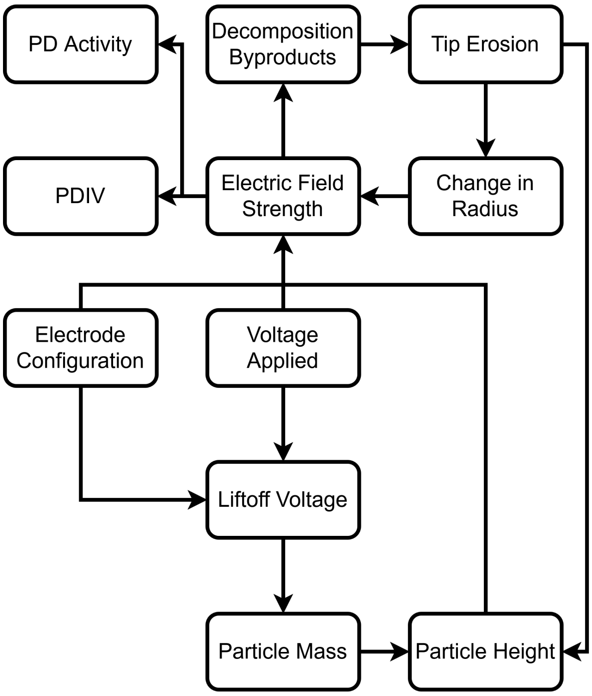

Figure 4.7: Flow chart to understand the interactions and dependencies of different phenomena related to protrusion and free metallic particle defects

The free metallic particle defect warranted additional investigation. Most studies focus on NoDi* patterns derived from the behavior of a single particle. Studies [44], [45] have examined multiple particles under HV conditions to analyze their collective behavior. To expand on this approach, the long-term experiment with the free metallic particle defect included particles with longer lengths than the finalized one. This allowed for a comparative analysis of PD behavior and the resulting NoDi* patterns, identifying potential overlaps and deviations between different particle sizes. The full set of free metallic particles used in this work is further detailed in Section 5.2.

Given the long-term nature of the experiments, particle containment was a key consideration to ensure that the free metallic particles remained within the HV area and exhibited the desired PD behavior of bouncing and firefly motion. As illustrated in Figure 4.8, multiple iterations were conducted to refine the containment method. The primary objective was to capture the particles without significantly distorting the electric field distribution.

The concave shape of the stainless steel lid, shown in Figure 4.8a, aided in redirecting ejected particles back toward the center of the electrode configuration. Similarly, the raised edges of the copper hoop in

Figure 4.8b improved particle capture but often resulted in particles becoming trapped in dead zones. The copper hoop was ultimately stacked on top of the stainless steel lid, combining the benefits of both designs. The edges of both components were treated with a plastic rim to create a rounder profile, reducing localized field enhancement. Copper tape was applied to the rounded edges to enhance conductivity and promote electric field homogeneity.

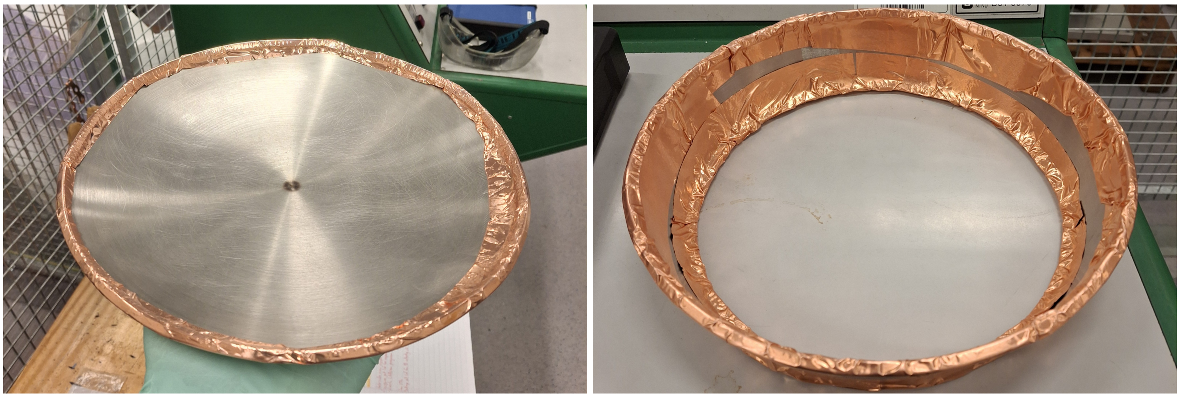

(a) Stainless steel lid with plastic rim and copper tape treatment

(b) Aluminum hoop with plastic rim and copper tape treatment

Figure 4.8: Pictures of the particle containment devices

Other particle contamination setups were explored based on findings from the literature review; however, each potential configuration presented challenges that could not be resolved, such as the static charging of glass and the tangling of the particle leash. Additionally, practical constraints, including time limitations and the narrow opening of the GIS test cell, influenced the choice of a more feasible approach to implementing particle contamination.

The implementation of the protrusion and free metallic particle defects is further discussed in the test procedure in Section 4.3 and later in the results in Chapter 5. With the defect characterization complete, the PD detection equipment can be examined.

4.1.3. PD Detection Equipment

Acquiring both conventional and non-conventional PD detection systems was rather straightforward as both were sourced from the same manufacturer, Omicron. Each system adhered to the IEC 60270 standard and was provided as a complete kit, including all necessary cables, battery packs, and software, ensuring seamless integration into the test setup.

As illustrated in Figure 4.9b, the Omicron MPD 800 was employed for conventional PD and direct voltage measurements. The accompanying MPD software facilitated the calibration of both readings. For the voltage measurement, the software included an option to select an HV resistor as the voltage input source and select the corresponding resistor value, eliminating the need for independent voltage verification. Nevertheless, a 5 kV voltage measurement was manually verified across the resistor using a multimeter to ensure accuracy. For the PD measurement, an external Omicron CAL 542 calibrator was connected across the GIS test cell and configured to output between 5 and 100 pC, to which the software automatically computed the corresponding calibration factor. The software also enabled adjustments to both the frequency range of the MPD 800 and the gain of the incoming PD signal. The frequency range was kept to the IEC recommendations (f_m = 250 kHz and Δf = 300 kHz) for consistency among other works. Further details can be found in the user manual [35].

The Omicron UHF 800 interfaced through the same software, allowing simultaneous monitoring of outputs from both devices. However, the recommended sensitivity test was not performed as the GIS test cell had only one UHF port. Although suggestions were made to connect a frequency generator to a self-made antenna inserted through the access port, this approach was ultimately ruled out. Despite lacking the correct factor in the software, the UHF 800 was utilized to verify that PD activity originated within the GIS test cell rather than from external sources. When properly tuned, the UHF 800 has been shown to produce PSA plots comparable to those obtained through conventional methods [43]. Through preliminary testing, the operator became familiar with the baseline noise levels and could, therefore, determine the presence of PD activity. However, the copper hoop used for particle containment partially blocked PD signals at lower intensities in the free metallic particle defect.

The software provided additional functionality, including options to set the noise threshold, trigger a PD counter for pass/fail testing, and export individual PD pulses as .CSV files for further analysis using the PSA plotter developed specifically for this work. The self-made PSA plotter is further elaborated in Section 4.4. With the lack of a phase angle reference, the Omicron software displays the PD pulses linearly on a time scale. Unfortunately, the program lacked an automatic PD recording feature, requiring the operator to be onsite to initiate recording manually.

Battery life was another concern for the MPD 800 and UHF 800 devices. Connected to a single battery pack, the UHF 800 possessed approximately 10 hours of recording time, while the MPD 800 pushed the limit closer to 18 hours. While both devices could be powered via the wall socket to extend the operational time, it was discovered that the ambient noise levels tripled. Instead, two battery packs were daisy-chained for the MPD 800, while the remaining third was connected to the UHF 800. Only three battery packs were sourced as the MPD and UHF 800 devices utilize a different connector than their predecessors. As a result, during the long-term testing, PD measurements were conducted in short intervals, after which the devices were placed in standby mode to conserve power.

Finally, the viewing window in the test cell was not utilized as the particle containment measure obstructed a clear line of sight.

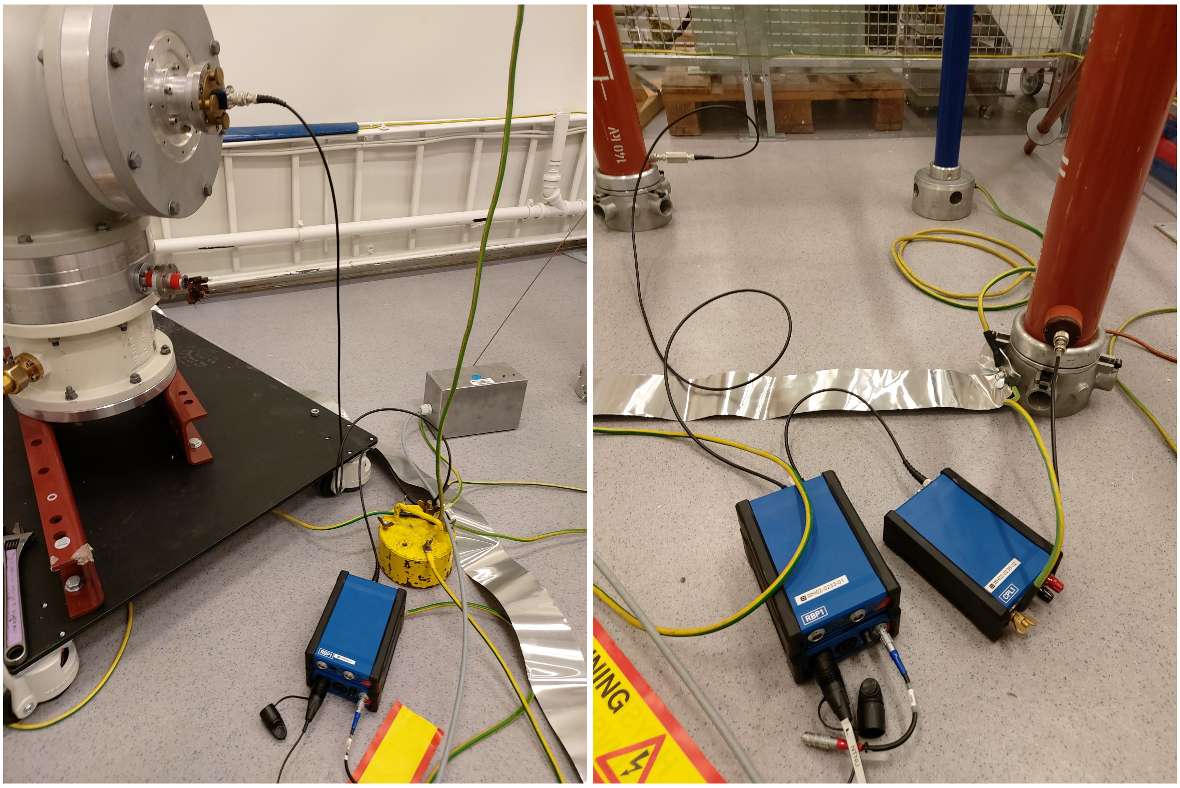

(a) Non-conventional method with the Omicron UHF 800

(b) Conventional method with the Omicron MPD 800

Figure 4.9: Pictures of the PD detection equipment

With the PD measurement equipment covered, the last remaining critical component of the test setup, the HVDC source, can be reviewed.

4.1.4. HVDC Source

Several HVDC sources were tested in parallel throughout different iterations of the test setup. The Spellman SL2000 (30 kV) and FUG HPC 140-35000 (35 kV) units exhibited varying performance during initial trial runs. Both units suffered from high noise levels, with the Spellman particularly affected by switching resonance occurring in 50 kHz intervals. Even when replaced with a 70 kV variant, the Spellman continued to exhibit the same issue, as shown in Figure 4.10.

In contrast, the FUG unit demonstrated significant improvement when upgraded to a more powerful 65 kV model, as illustrated in Figure 4.11. This transition led to a notable reduction in noise levels and introduced a convenient manual polarity reversal feature via a knob. Unlike the FUG, the Spellman required disassembly and internal reconfiguration for polarity reversal, making it less convenient for frequent adjustments. The exact noise levels for each source are summarized in the results in Table 5.1.

The initial configuration of the FUG HVDC source uncovered a technical fault. The master knob controlling the voltage output was malfunctioning, causing significant voltage fluctuations beyond 3 kV. To circumvent this, all communication with the FUG was handled remotely via a National Instruments GPIB controller. A custom LabVIEW program was developed to manage voltage commands, providing a more stable and precise control interface. The program's front-end interface is depicted in Figure 4.13.

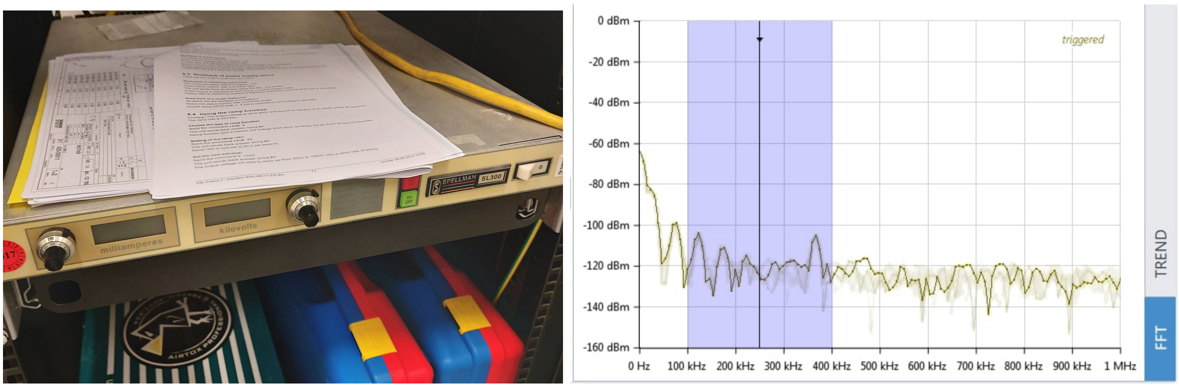

(a) Picture of the physical unit **(b)** Noise level at 10 kV with no defect

Figure 4.10: Pictures of the Spellman 70 kV HVDC source and the corresponding frequency spectrum from the MPD 800

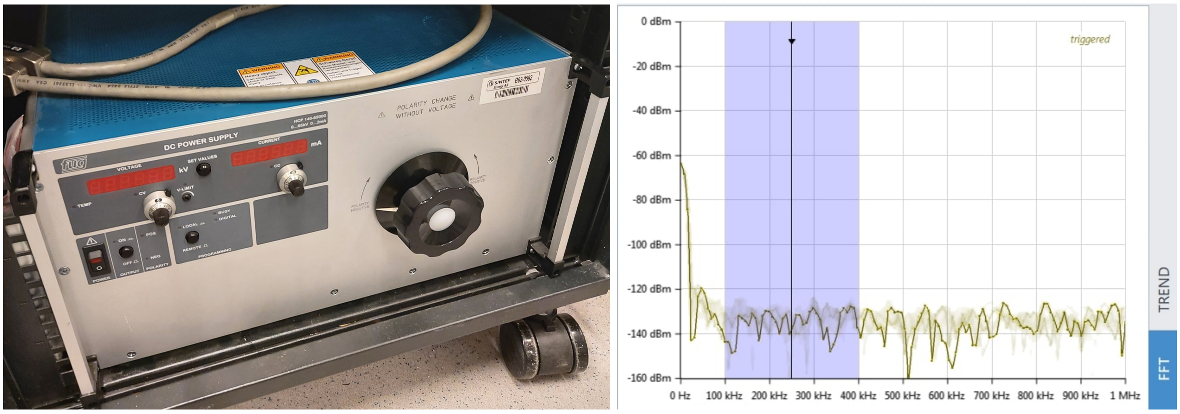

(a) Picture of the physical unit **(b)** Noise level at 10 kV with no defect

Figure 4.11: Pictures of the FUG 65 kV HVDC Source and the corresponding frequency spectrum from the MPD 800

Preliminary testing with both defect types confirmed that the 65 kV range of the FUG HVDC source was sufficient to capture all the desired PD phenomena and particle motion. While higher-rated HVDC sources were available, they were deemed unnecessary for this study.

The custom LabVIEW program used to send voltage commands to the HVDC source was part of a larger array of safety measures undertaken in this work, as further explained in the following section.

4.2. Safety Precautions

Safety was a major concern, considering the pressurized and HV nature of the GIS test cell. A risk assessment was completed to identify potential risks involved with the experiments, ranging from electrical to mechanical. To prevent possible injury and undesirable incidents, the following precautions were implemented:

- The HVDC sources were powered through the master switch as shown in Figure 4.12a and were automatically disconnected if the door was opened
- The master switch as shown in Figure 4.12a controlled protection features such as the door lock check, automatic grounding, and live experiment light
- A grounded cage surrounded the entire test setup
- The metal rack containing the HVDC sources was grounded to protect the operator
- An automatic grounding stick was installed to discharge any residual voltage from the circuit, particularly from the coupling capacitor, as illustrated in Figure 4.1
- An earthing probe was used to ground every HV component upon reentry into the HV area
- HV components were adequately grounded, with the GIS test cell grounded separately using aluminum foil
- LEXAN uncoated polycarbonate sheets were installed to shield the operator in the event of explosive decompression or particle projectile
- A pressure relief valve was mounted on the test cell to avoid explosive decompression
- Gas filling was performed in pairs, with both individuals wearing helmets with face shields and ear protection
- Warning lights were installed on the grounded cage to indicate when the experiment was live and/or pressurized
- Appropriate signage was posted outside the grounded cage as shown in Figure 4.12b
- Warning tape was placed on critical areas to prevent injury to equipment, i.e., to prevent personnel from stepping on optical fiber cables
- Safety shoes were worn at all times while inside the HV area

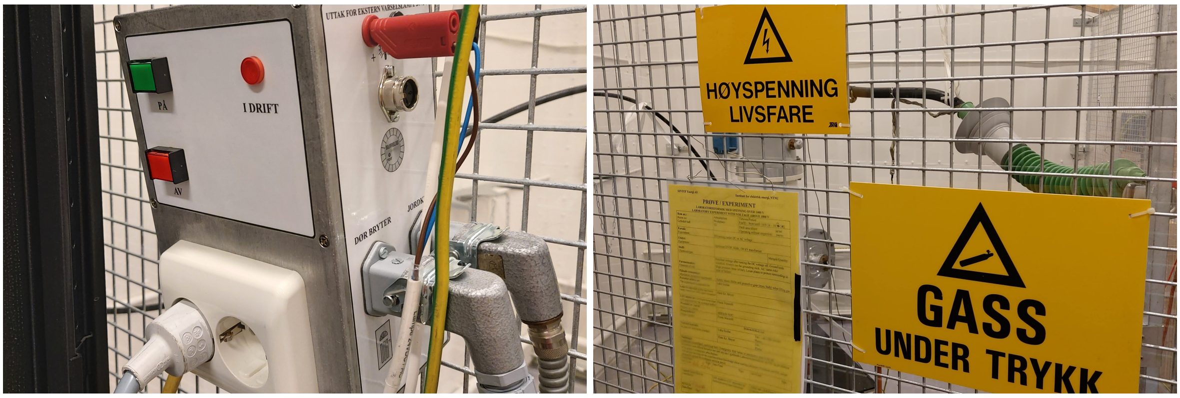

(a) Main switch connected to automatic grounding, HVDC power source, door lock, and live experiment light

(b) Appropriate signage informing natural of experiments and attached risk assessment

Figure 4.12: Examples of safety precautions implemented

Given the long-term nature of the experiments, one safety feature was paramount: an automatic shutdown mechanism during a breakdown. Since the experiment was often left unsupervised for extended periods, an uncontrolled HVDC source posed a significant risk to personnel and equipment. To mitigate this, the LabVIEW program was designed to continuously monitor the current and trigger an automatic shutdown if the user-defined limit was exceeded. As illustrated in Figure 4.13, the operator can activate the overcurrent protection and view the current measurement in real time. As an added safety feature, voltage commands cannot be transmitted when the current protection is activated.

The LabVIEW program was developed from scratch, as shown in Figure C.1 and Figure C.2. Given that the HVDC source can only process commands sequentially, multiple conditional cases were implemented to prevent simultaneous data transmission and reception, which could otherwise lead to miscommunication between the HVDC source and the computer. By default, the HVDC source returns a confirmation message when it has successfully received a command.

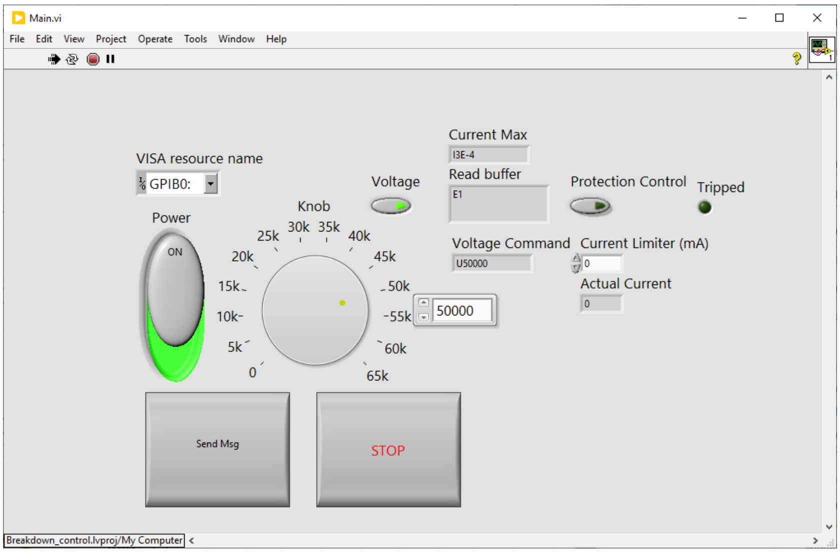

VISA resource name: GPIB0:
Current Max: I3E-4
Read buffer: E1
Voltage Command: U50000
Current Limiter (mA): 0
Actual Current: 0
Knob: 50000

Figure 4.13: Frontend of LabVIEW program used to send voltage commands and execute overcurrent protection

With all the systems and components of the test setup thoroughly described, the next section introduces the test procedure.

4.3. Test Procedure

In line with the test setup and safety precautions, the test procedure was a critical component of the experimental process, ensuring consistency and comparability between the two defect types. Before conducting the long-term experiments, several preliminary test runs were performed to achieve a PD-free setup and verify sufficient PD activity under different test conditions, as detailed in Chapter 5.

To establish a PD-free setup, the electrode configuration without any defects was gradually subjected to the maximum operating level of 65 kV. As voltage ramp-up simulates AC voltage conditions, PD activity can be potentially triggered and cause false positive PDIV readings. If PD activity was detected, the voltage was held steady while the setup was left undisturbed for 5–10 minutes to allow space charges to reach equilibrium. Such a duration was chosen to reflect the relatively small time constant of the system, or the time it takes for the field to transition from capacitive to resistive. The number of PD pulses per minute was then recorded, with PDIV defined as the voltage at which three or more PD pulses occurred within 30 seconds [39]. Due to the rather noisy surroundings, the more lenient threshold reported in the literature was chosen. During testing, the pressure had to be increased beyond ambient as significant PD activity was observed at 57.5 kV, indicating a potential risk of breakdown. Upon increasing the pressure inside the GIS test cell to 3 Bar absolute, no significant PD activity was detected.

As previous studies have examined the effects of test conditions such as gas pressure and defect type on PDIV, the role of PDIV in this work was different. The primary objective was to establish a sustained stream of PD pulses, ensuring a representative defect pattern and continuous PD activity over several days. Preliminary test runs revealed that the PD apparent charge magnitude decreases significantly overnight, making it essential to maintain continuous discharge behavior throughout the experiment. Therefore, determining the PDIV for each defect type was crucial in ensuring a sufficient margin between the PDIV and the 65 kV operating limit of the HVDC source.

These preliminary tests also provided insight into the expected number of PD pulses for each defect type. The decision to maintain 30-second-long PD measurements was based on the work by A. Pirker et al. [24] and early observations that such measurement intervals captured several million PD pulses. PD measurement files with over ten million individual pulses placed a substantial computational strain on the PSA plotter developed for this work.

Based on these findings, the test procedure for long-term experiments underwent several revisions and optimizations. The final version is outlined in the following steps:

1. Press the red button on the master switch, as shown in Figure 4.12a, to activate automatic grounding if there is an ongoing experiment.
2. Open the door to the Faraday cage and ground the HV potential side of every HV component using the grounding stick.
3. Leave the grounding stick connected to the HV potential side of the measurement circuit, specifically to one of the metal caps on the red capacitor or resistor pillars.
4. Conduct a general visual inspection of the measurement equipment and surrounding components for any irregularities, such as loose connections, displaced parts, or contamination.
5. Wear the helmet with the face shield and approach the GIS test cell to begin the gas release process if the system is pressurized from a previous experiment.
6. Ensure that the gas canister and release valves are closed before opening the valve connected to the GIS test cell.
7. Open the release valve cautiously to vent the insulating gas from the GIS test cell into the surrounding lab space; use ear protection if needed.
8. Leave the valves open to ensure pressure equilibrium when opening the access port.
9. Wear gloves if not already done and loosen the screws of the access port using two socket wrenches with 19 mm hex sockets.
10. Handle the access port hatch with care and gently lay it down onto styrofoam to prevent damage.
11. Inspect the seal for dryness, cracks, or any signs of degradation that could affect gas tightness.
12. Use a lint-free cloth to wipe down interior surfaces and apply a dab of isopropanol to another cloth to clean the electrodes of any buildup.
13. Unscrew the ground electrode if performing a protrusion defect test, then secure the bent particle with electrical tape, ensuring its height matches the desired height; reattach the electrode, making sure the particle does not bump into the HV electrode.
14. Insert the stainless steel lid first if performing the free metallic particle defect test, ensuring the particle(s) are pre-positioned. Then, place the copper hoop, centering both items as best as possible on the ground electrode. The copper hoop may need to be slightly bent to clear the 240 mm access port.
15. Secure the access port hatch, ensuring the seal is properly positioned, and thread the screws into each hole before tightening.
16. Tighten the screws to 70 Nm in a star pattern to ensure uniform pressure distribution, then recheck all screws.
17. Open the gas canister valve after ensuring the release valve is closed while keeping the valve to the GIS test cell open. Fill the GIS test cell to the desired gas pressure, monitoring the process through the pressure regulator.
18. Close all remaining valves, including the gas canister valve, once the desired gas pressure is reached.
19. Exchange or plug in the Omicron UHF and MPD 800 device battery packs to ensure sufficient power.
20. Open the Omicron software and turn on the PD measurement devices.

21. Perform the calibration step of the MPD 800 adherent to the IEC 60270 standard by disconnecting all grounding devices and connecting the calibrator CPL 542 directly across the GIS test cell, ideally at the bushing terminal and grounded enclosure. Set the output value to 5 pC on the calibrator and press the ”compute” button in the calibration tab of the Omicron software. Repeat with values up to the maximum of 100 pC for a linearity check.
22. Disconnect the calibrator and reconnect all previously disconnected grounding devices.
23. Check for any forgotten items inside the HV area and return the grounding stick to its designated spot before leaving the cage.
24. Press the green button to initiate the experiment by supplying power to the HVDC source and disconnecting the automatic grounding from the test circuit.
25. Initialize communication between the HVDC source and the computer through the LabVIEW program, then increase the voltage incrementally by 1 $\frac{kV}{s}$ until PDIV is reached. Maintain a constant voltage for 5-10 minutes to ensure a stable reading before recording the value; proceed to the final desired voltage value.
26. Activate the overcurrent protection function in the LabVIEW program to safeguard the system.
27. Wait 15-20 minutes and observe test conditions, then record PD measurements for 30 seconds and export the data as a .CSV file.
28. Power down the PD measurement equipment using the Omicron software to conserve battery life.
29. Perform steps 27 and 28 twice daily for the duration of the long-term experiment, ensuring consistent data collection.
30. Repeat steps 1-12 at the end of the experiment, followed by removing either the protrusion defect from the ground electrode or the free metallic particles from the stacked hoop lid setup.

The PD measurement schedule within the test procedure was designed with flexibility in mind to accommodate external experimental activities beyond the operator’s control. For instance, morning PD measurements sometimes had to be rescheduled to the afternoon when surrounding conditions were quieter, reducing interference and improving data reliability. Similarly, the gas-filling process left room for improvement. For example, while vacuum pumps were available for evacuating and flushing the GIS test cell with fresh technical air, their use was deemed unnecessary at such low pressures as it did not significantly benefit the measurement conditions.

The next section deals with the analytic methods used to examine the changes in particle composition and PD behavior over time.

4.4. Analysis Methods

The analytical methods employed in this study were systematic, ensuring a comprehensive assessment of both defect types. Each particle was weighed, measured, and examined under a microscope to document its physical properties before testing. After completing the long-term experiments, the same weighing and microscopic examination process was repeated to detect any changes in mass, structure, or surface condition resulting from prolonged PD activity.

The PD measurement data collected from the Omicron MPD and UHF 800 devices were processed using the custom-built PSA plotter, which aided defect classification and PD pattern verification. The tool facilitated detailed visual and statistical analysis, ensuring the recorded PD activity was consistent with expected defect behavior.

Since NoDi* plots formed the primary basis for observations and conclusions in this work, the methodology was guided by key insights from A. Pirker et al. [24]. For instance, PD patterns are mirrored at the origin when polarity is reversed, stochastic PD pulses result in symmetrical patterns, and alternating pulses lead to asymmetrical patterns. Additionally, periodically recurring pulses form distinct clusters.

While other studies have explored integrating neural networks with NoDi* patterns, this work prioritized the experimental aspect, contributing to the field by developing and implementing the PSA plotter. The specific features and capabilities are detailed in the following subsection.

PSA Plotter

As PD measurements rely heavily on trend analysis, a structured database of results and references, such as NoDi* patterns, is essential for tracking and identifying critical PD behavior that could indicate potential breakdown conditions. The PSA plotter was developed to provide a robust and flexible platform for generating NoDi* plots and other relevant visualizations. The code for the PSA plotter is presented in Appendix A, with proper documentation and version control maintained through GitHub (`https://github.com/CodeMisUser/NoDiPlots_Database.git`).

The PSA plotter was designed with user convenience in mind, incorporating several key features:

- Directly import PD measurement files from Omicron software, regardless of the device used (MPD 800 or UHF 800)
- Display the PD measurement duration and the total number of PD pulses in each plot
- Compute and visualize any of the four NoDi* pattern types
- Generate density function and time scale plots of the PD apparent charge magnitude and time differences
- Split PD measurements into user-defined time intervals for more detailed analysis
- Select from various NoDi* plot grid sizes, ranging from 100-by-100 to 25-by-25
- Set custom upper and lower bounds for NoDi* plots to define the visible data range

If the PSA plotter does not fully meet the needs of the user, the processed NoDi* plot data can be exported as a .txt file, enabling data flexibility. This allows for easy integration with other analysis tools such as MATLAB, optimizing storage space and eliminating the need to repeatedly import large Omicron files, especially for long-duration measurements. Additionally, saving the data in a 25-by-25 grid size format enhances compatibility with neural network training applications.

The Omicron software handles the file format requirements. The delimiter must be set to ”semicolon,” and the ”Be Compatible with Microsoft Excel” option should be enabled to ensure proper formatting.

The PSA plotter further has a GUI window to allow a better user experience, as illustrated in Figure 4.14.

No file selected

File length: (empty) (s)

Enter desired length(s): (Start) (End)

☐ Whole File

Select a plot option: Q(i+1) and Q(i)

Select a grid size: 100

Enter X and Y scale

☐ Save Array

Figure 4.14: Picture of the GUI interface of the PSA plotter

With the methodology established, the results of this work are presented in the next chapter.

5

Experimental Results

This chapter presents the results obtained from the preliminary and long-term experiments, including the NoDi* patterns and the physical examination of particles through weighing and microscope imaging. The findings provide insights into the behavior of PD activity under different defect conditions and test parameters.

The entire test setup was verified without defects inside the GIS test cell, establishing a baseline as further detailed in section 5.1. This was done to measure the ambient noise level, which was determined to have a maximum value of approximately 0.6 pC at the operating voltage of 65 kV. The free metallic particle defect was analyzed first, as it was necessary to determine the appropriate particle length for the protrusion defect experiments.

It is essential to clarify that all voltage polarities mentioned in this chapter are relative to the HVDC source. Therefore, in the case of the protrusion defect, the metallic particle will have the opposite polarity of the stated one. Additionally, all pressure values provided in this section are absolute.

5.1. Verification of Test Setup

The objective of this stage in the experimental process was to establish the ambient noise level and identify any potential sources of interference. The noise levels, summarized in Table 5.1, were measured using the MPD 800 across a range of voltage levels, with tests conducted at 3 Bar absolute to assess conditions at higher operating voltages. Readings were taken 5–10 minutes after voltage stabilization to ensure reliable results and denote a representative average of the values encountered.

A key outcome of these tests was the selection of the FUG 65 kV unit over the Spellman 70 kV unit as it successfully met the target noise level of under 0.7 pC, which is considered acceptable according to literature. Additionally, the tests revealed other critical factors that influenced PD measurements. For example, plugging the laptop into a wall socket and any physical disturbance of the test cage caused spikes in the PD readings recorded by the MPD 800.

Table 5.1: Noise levels of the different HVDC sources with no defect present at 3 Bar absolute measured with MPD 800

Spellman 70 kV HVDC Source			FUG 65 kV HVDC Source	
Voltage (kV)	IEC Standard (f_m = 250 kHz, Δf = 300 kHz)	Expanded (f_m = 666.67 kHz, Δf = 1 MHz)	IEC Standard (f_m = 250 kHz, Δf = 300 kHz)	Expanded (f_m = 666.67 kHz, Δf = 1 MHz)
20	1.16 pC	0.37 pC	0.34 pC	0.29 pC
30	1.38 pC	0.45 pC	0.36 pC	0.31 pC
40	1.60 pC	0.55 pC	0.43 pC	0.36 pC
50	1.80 pC	0.78 pC	0.45 pC	0.38 pC
60	1.99 pC	0.97 pC	0.51 pC	0.40 pC

The same round-robin approach to noise level measurements was applied to the free metallic particle defect, as shown in Table 5.2. However, for the protrusion defect, a more general pass/fail assessment was conducted instead of a more detailed noise-level evaluation. The next section focuses on the first defect type: the free metallic particle defect.

5.2. Free Metallic Particle Defect

The free metallic particle defect was one of the two defect types investigated in this study. Given the range of possible particle characterizations, a diverse selection of particles was tested, as illustrated in Figure 5.1, to gain a deeper insight into the interactions and dependencies associated with different particle lengths. In the long-term experiments, a combination of these particles was exposed to 65 kV for one week to assess their behavior over extended durations.

Before initiating the fully-fledged long-term experiment, an iterative approach was employed to identify metallic particles capable of achieving liftoff under the given conditions while maintaining continuous PD activity for measurement. The particles labeled 2 through 10, as shown in Figure 5.1, were derived from an initial 4 mm particle, labeled Particle 1, as shown in Figure 5.1a. The subsequent nine particles varied in length, with the longest measuring 10 mm. The width remained constant at 3.5 mm, while the thickness fluctuated around an average of 0.1 mm on some sides and 0.25 mm on others, as further confirmed by microscope imaging. The corresponding weights of each particle were obtained using a precision scale with 0.01 mg accuracy and are listed under each image in Figure 5.1.

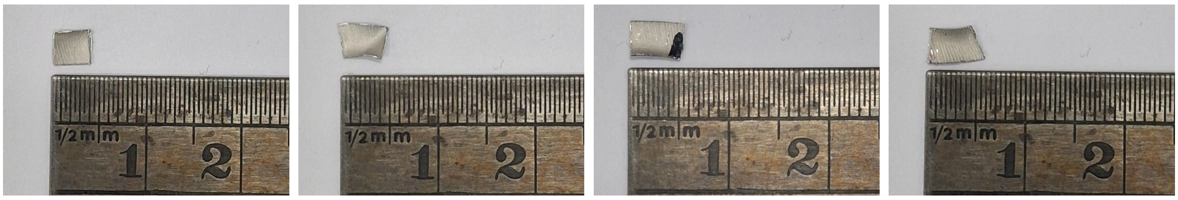

(a) Particle 1 (4 mm; 8.69 mg) **(b)** Particle 2 (4 mm; 9.29 mg) **(c)** Particle 3 (5 mm; 11.62 mg) **(d)** Particle 4 (5 mm; 11.17 mg)

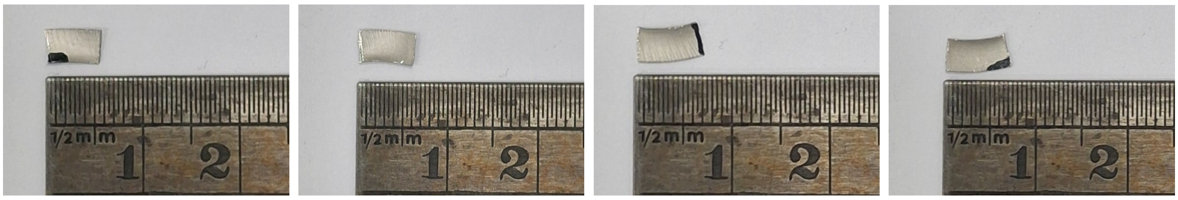

(e) Particle 5 (6 mm; 12.41 mg) **(f)** Particle 6 (6 mm; 13.27 mg) **(g)** Particle 7 (7 mm; 13.81 mg) **(h)** Particle 8 (7 mm; 14.56 mg)

(i) Particle 9 (8 mm; 17.38 mg) **(j)** Particle 10 (10 mm; 20.99 mg)

Figure 5.1: Measurements and weights of particles used in the free metallic particle defect experiments

The extensive preparation of the free metallic particle defect aimed at ensuring the successful observation of the firefly motion. This phenomenon exhibits significantly more variation than the bouncing motion, necessitating further investigation. Due to time constraints towards the end of the study, the long-term experiment was conducted using only one voltage polarity. Positive polarity was selected for the long-term tests to facilitate particle containment, as firefly motion tends to occur at the ground electrode rather than the HV conductor [24], [46]. Nonetheless, some preliminary test runs were performed under negative polarity for comparison.

The following section details the iterative approach, presenting the finalized setup and the selected particles used later for the long-term experiment.

5.2.1. Preliminary Test Phase with Different Particle Containment Setups

In addition to sourcing the optimal metallic particle, the preliminary test runs aimed to gain a deeper understanding of the final particle trajectory after repeated collisions with the HV conductor or ground electrode, depending on the voltage polarity. This information was used to evaluate the particle containment measures to ensure stable PD activity throughout the experiment.

Three distinct particle containment setups were designed, tested, and analyzed. The first setup involved a repurposed stainless steel lid procured from a secondhand store. The outer lip was removed to allow entry into the GIS test cell, and the sharp rim edges were treated with a plastic liner and wrapped with copper tape to reduce unwanted PD activity.

The second setup utilized an aluminum bowl, which was modified by removing both the top and bottom to achieve a band with a 50 mm width. The top and bottom edges were treated to minimize edge effects, as with the stainless steel lid. The original and modified copper hoop were differentiated by an additional application of copper tape along the interior as illustrated between Figure 4.8b and Figure 5.7a.

The third setup combined the stainless steel lid and copper hoop into one unit, integrating their advantages to improve particle containment. Each of these setups was tested for PD activity, and the corresponding noise level measurements by the MPD 800 at specific voltage levels are summarized in Table 5.2. The displayed values are meant to be representative of the averages encountered.

Table 5.2: Noise levels of the different test setups for the free metallic particle defect with no particle present

Voltage Level (kV)	Stainless Steel Lid (1 Bar Absolute)	Original Copper Hoop (1 Bar Absolute)	Modified Copper Hoop (1 Bar Absolute)	Stacked Copper Hoop and Lid (3 Bar Absolute)
10	0.38 pC	0.37 pC	0.35 pC	0.33 pC
20	0.43 pC	0.41 pC	0.39 pC	0.35 pC
30	0.45 pC	0.47 pC	0.48 pC	0.41 pC
40	0.47 pC	0.50 pC	0.48 pC	0.42 pC
50				0.45 pC
60				0.45 pC
65				0.41 pC

Moreover, the parameters used in each preliminary test run are presented in Table 5.3. The calibration factors are established using the calibrator before each PD test run and are then applied by the Omicron software to convert measured values into the final representative ones to be used by the operator. It is important to note that the third test setup was tested under two different configurations: the first with only Particle 1 (4 mm) and the second with all ten particles shown in Figure 5.1.

Table 5.3: Testing schedule concerning the three test setups for the preliminary test phase of the free metallic particle defect

	Pressure Absolute (Bar)	Polarity	PDIV (kV)	Voltage Tested (kV)	Calibration Factor		Particle(s) Tested	Report Label
Stainless Steel Lid	3	-	45.1	49.1	6.13678	Day 1	Particle 1 (4 mm)	Session 1
	3	-	45.1	52.1	6.13678	Day 2	Particle 1 (4 mm)	Session 2
	3	-	45.1	53.1	6.13678	Day 2	Particle 1 (4 mm)	Session 3
	3	-	45.1	60.1	6.13678	Day 2	Particle 1 (4 mm)	Session 4
Modified Copper Hoop	1	-	37.1	43.1	6.22012	Day 4	Particle 1 (4 mm)	Session 5
Stacked Copper Hoop and Lid	3	-	46.1	47.1	6.13058	Day 4	Particle 1 (4 mm)	Session 6
	3	+	43.1	65.1	6.13058	Day 4	Particle 1 (4 mm)	Session 7
	3	+	43.1	50.1	6.13058	Day 4	Ten Particles Voltage Overnight	Session 8
	3	+	43.1	50.1	6.13058	Day 5		Session 9

Setup with the Stainless Steel Lid

The objective of the first setup shown in Figure 5.2a was to empirically determine the liftoff voltage of the starting particle of 4 mm length. As depicted in Table 5.3, the GIS test cell was pressurized to 3 Bar absolute, and the voltage was increased by $1\frac{kV}{s}$ as specified in the test procedure. The particle achieved liftoff at 52 kV and, unfortunately, underwent a trajectory that resulted in a final resting place in the bottom of the GIS test cell as observed in Figure 5.2b.

(a) Particle inside GIS test cell with stainless steel lid **(b)** Final resting place of particle (below electrode configuration)

Figure 5.2: Pictures of the first setup of the preliminary free metallic particle defect test phase with the stainless steel lid and Particle 1 (4 mm)

The following four figure sets illustrate the PD behavior before and after particle liftoff. To facilitate visual comparison, the plots in each set are scaled according to a reference plot within the group.

The magnitude difference NoDi* plots in Figure 5.3a, Figure 5.4c, Figure 5.5a, and Figure 5.6a are scaled to an upper and lower range of 250 pC. This scale reflects the peak values observed during the firefly motion captured at -52 kV in Figure 5.4c. To examine the PD activity near the center of the pattern, the magnitude difference NoDi* plots in Figure 5.3b, Figure 5.4d, Figure 5.5b, and Figure 5.6b are scaled to 8 pC, aligning with the limits of the last PD measurement at -60 kV in Figure 5.6b. Similarly, the time difference NoDi* plots in Figure 5.3c, Figure 5.4e, Figure 5.5c, and Figure 5.6c are scaled to 0.1 seconds to capture the most relevant details in each case.

Although PD measurements were conducted at additional voltage levels, these four selected sessions provide a representative overview of the observed behavior. The first session at -49 kV is presented in Figure 5.3. Standing motion was observed in the detailed view in Figure 5.3b, but not firefly.

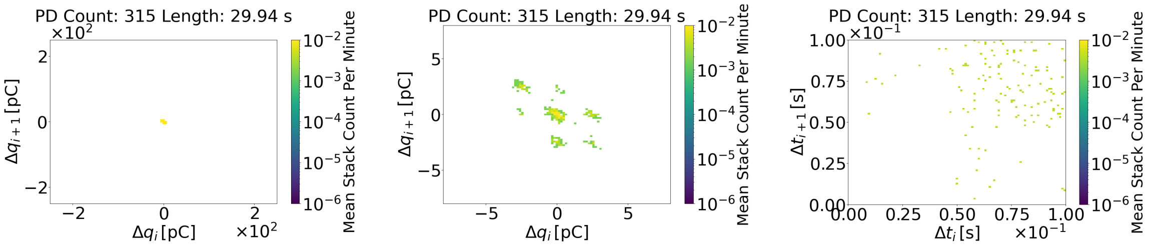

(a) MPD Magnitude difference NoDi* plot **(b)** Closeup of magnitude difference plot [a] **(c)** MPD time difference NoDi* plot

Figure 5.3: Plots of the first setup of the preliminary free metallic particle defect with stainless steel lid and Particle 1 (4 mm) at -49 kV and 3 Bar absolute with standing motion - Session 1

The voltage increase to -52 kV successfully induced particle liftoff. Although no visual recording equipment was available to confirm this definitively, the combined data from the MPD and UHF measurements was sufficient. The NoDi* pattern in Figure 5.4c closely resembles the firefly motion documented in previous studies in Figure 3.6b, albeit with more prominent diagonals. The closeup of the time difference NoDi* plot in Figure 5.4f further supports this conclusion.

A significant increase in both discharge magnitude and the number of PD events, compared to the previous measurement at -49 kV in Figure 5.3, indicates a substantial shift in the test environment, equating to the movement of the particle. Additionally, the detailed view of the MPD measurement in Figure 5.4b indicates the firefly motion with large jumping amplitudes, initially noted by P. Wenger et al. [46]. Further validation of the firefly motion is provided by the UHF data, as shown in Figure 5.4g and the detailed view in Figure 5.4h. The UHF measurements are plotted as a magnitude difference NoDi* plot in Figure 5.4i and resemble the standing motion of the free metallic particle on the HV conductor as depicted in other studies as shown in Figure 3.6a. The UHF data in Figure 5.4g aligns with the PD activity observed at the start of the MPD measurement in Figure 5.4a.

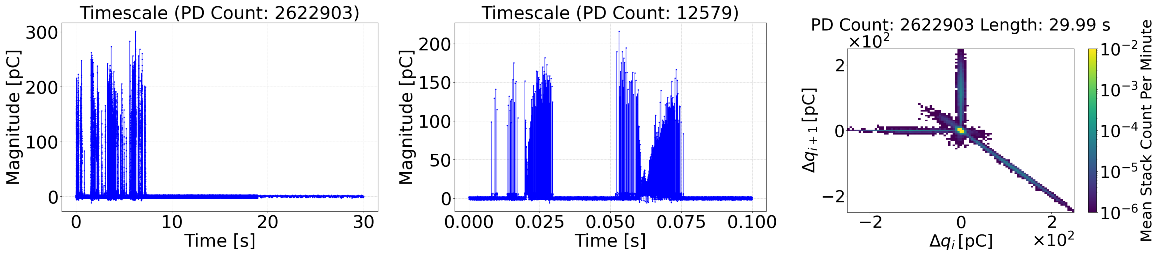

(a) MPD measurement over entire period **(b)** Closeup of peaks [a] **(c)** MPD Magnitude difference NoDi* plot [a]

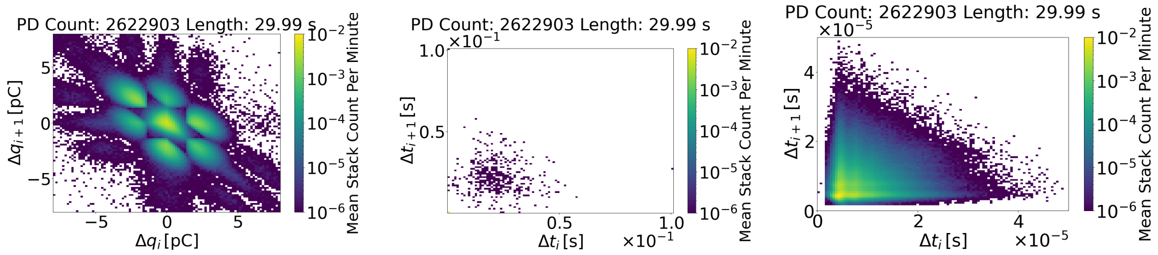

(d) Closeup of magnitude difference plot [c] **(e)** MPD time difference NoDi* plot [a] **(f)** Closeup of time difference plot [e]

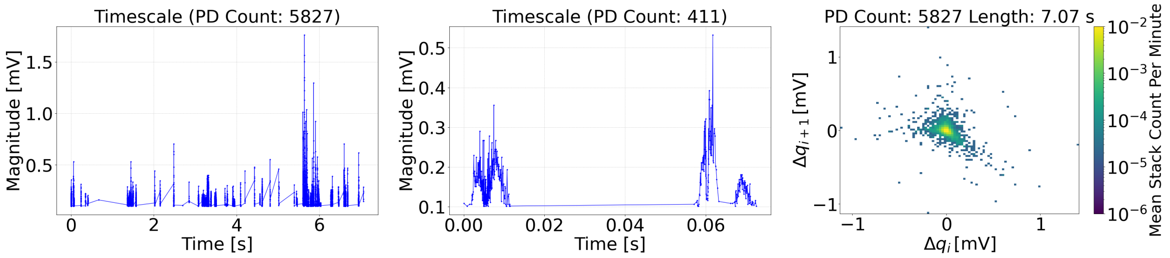

(g) UHF measurement over entire period **(h)** Closeup of UHF measurement [g] **(i)** UHF magnitude different NoDi* plot [g]

Figure 5.4: Plots of the first setup of the preliminary free metallic particle defect with stainless steel lid and Particle 1 (4 mm) at -52 kV and 3 Bar absolute with firefly motion - Session 2

When no further PD activity was observed, the voltage was increased to determine whether the particle had moved. At -53 kV, the NoDi* plots in Figure 5.5 provided a snapshot of the test conditions. The close-up view of the magnitude difference NoDi* plot in Figure 5.5b exhibited the standing motion, suggesting that the particle remained within the electrode configuration. Further observation of the UHF data stream until voltage turnoff revealed no further PD activity, inferring that the particle had been displaced from the electrode configuration during the previous firefly motion. Visual inspection upon opening the GIS test cell confirmed the final resting place to be well outside the high-field areas.

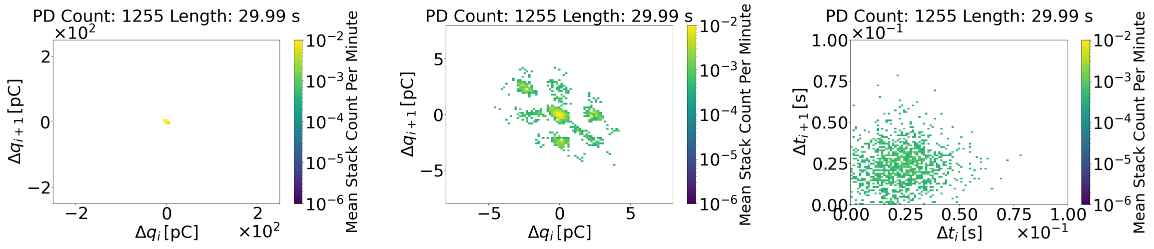

(a) MPD magnitude difference NoDi* plot **(b)** Closeup of magnitude difference plot [a] **(c)** MPD time difference NoDi* plot

Figure 5.5: Plots of the first setup of the preliminary free metallic particle defect with stainless steel lid and Particle 1 (4 mm) at -53 kV and 3 Bar absolute with standing motion - Session 3

Increasing the voltage to the final value of -60 kV further revealed the growing trend in PD activity, as shown in Figure 5.6b. A combination of factors suggests the observed PD activity was primarily associated with space charge regions surrounding the stainless steel lid rather than the free metallic particle defect. The lack of detection on behalf of the UHF device and the substantially low repetition rate support this hypothesis. Likewise, the complete symmetry around the origin in Figure 5.6b further indicates that the resulting stochastic PD behavior is likely influenced by space charge interactions rather than the presence of a free metallic particle.

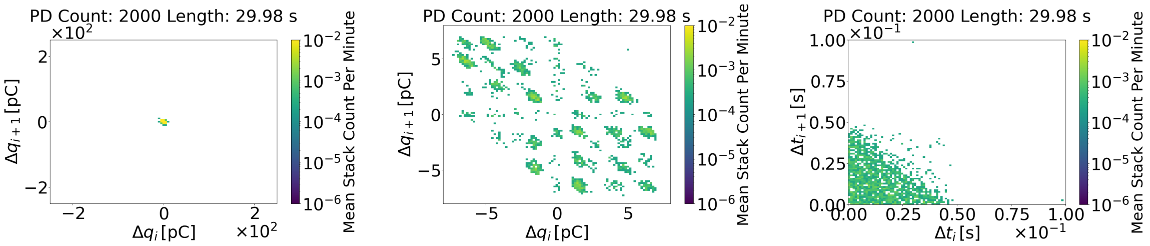

(a) MPD magnitude difference NoDi* plot **(b)** Closeup of magnitude difference NoDi* plot **(c)** MPD time difference NoDi* plot

Figure 5.6: Plots of the first setup of the preliminary free metallic particle defect with stainless steel lid and Particle 1 (4 mm) at -60 kV and 3 Bar absolute - Session 4

As the stainless steel lid ultimately failed to contain the particle, the second setup with the copper hoop was developed and tested. The next section demonstrates the capabilities of the copper hoop.

Setup with Copper Hoop

The copper hoop underwent modifications from its original iteration, as illustrated in Figure 4.8b. The initial application of copper tape resulted in uneven layers, raising concerns that particles could become trapped. Thus, a single continuous layer of copper tape was applied to the interior surface of the hoop, ensuring a smoother surface for deflecting incoming particles and promoting a more uniform electric field distribution.

Following these adjustments, Particle 1 (4 mm) was placed inside the GIS test cell, as depicted in Figure 5.7a, and the voltage was gradually increased until liftoff was achieved. The application of voltage over time resulted in the final resting place of the particle in a dead zone, as shown in Figure 5.7b.

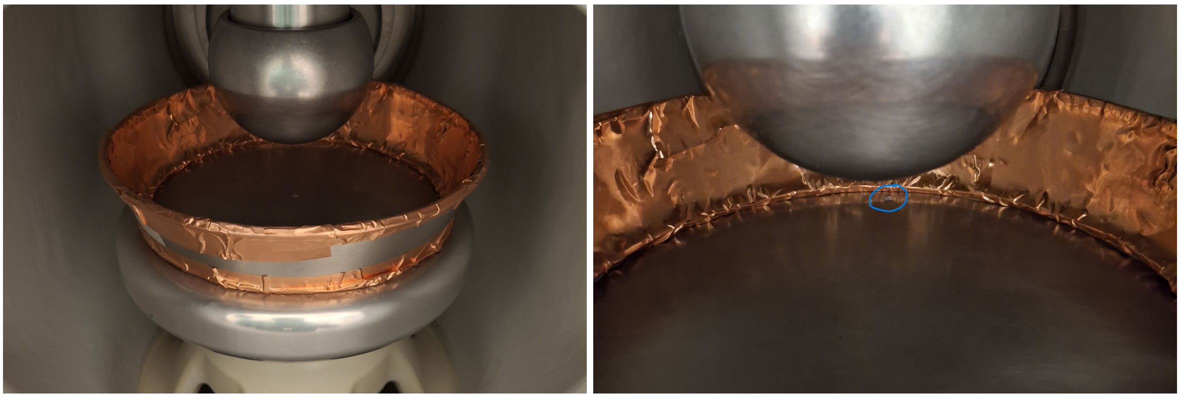

(a) Particle inside GIS test cell with modified copper hoop **(b)** Final resting place of particle (in dead zone)

Figure 5.7: Pictures of the second setup of the preliminary free metallic particle defect test phase with the modified copper hoop and Particle 1 (4 mm)

The second test setup produced a more defined defect pattern than the first, as illustrated in Figure 5.8d, when the particle achieved liftoff at -43 kV and 1 Bar absolute. Despite applying the same voltage polarity, the orientation of the diagonals was mirrored, compared to the previous NoDi* pattern in Figure 5.4c. As the liftoff occurred during voltage ramp-up, the resulting PD apparent charge magnitude values, shown in Figure 5.8a, were among the highest recorded across all experiments.

The firefly pattern in Figure 5.8d deviated significantly from previously observed patterns, exhibiting notably larger PD apparent charge magnitudes and sharper defined diagonal groupings. In contrast, the firefly motion described in literature, as illustrated in Figure 3.6b, displays a broader dispersion of PD activity within the center, accompanied by more filled diagonal pairs. The timescale plot in Figure 5.8a and the detailed view in Figure 5.8b provided further insight into this phenomenon. Positive and negative peaks exceeding 500 pC indicate firefly motion occurring at the HV conductor and the ground electrode. Additionally, analysis of the UHF data in Figure 5.8c further validates the presence of the firefly motion. However, the gap between the two peak groupings suggests that the copper hoop effectively acted as a shield, blocking EM waves generated by PD activity when the particle was not near the HV conductor.

Following the firefly motion, PD activity decreased to the ambient noise levels, aligning with the values observed during the PD-free check in Table 5.2. While it did block EM waves generated by the particle when it was in the vicinity of the ground electrode, the copper hoop demonstrated better management of space charge regions than the stainless steel lid as hardly any PD pulses were detected above the noise level, i.e. ten to twenty pulses per thirty seconds with no discernible pattern.

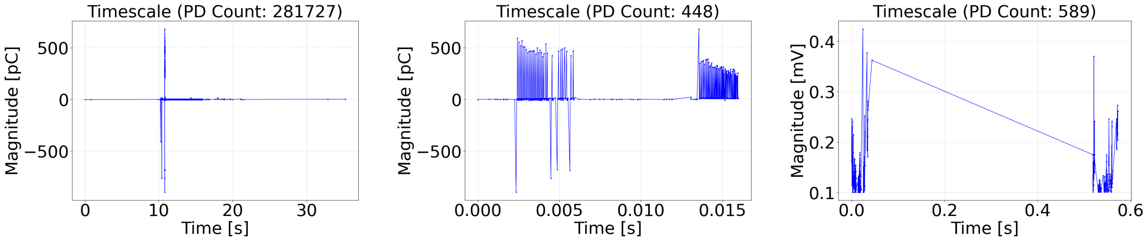

(a) MPD measurement over entire period

(b) Closeup of peaks [a]

(c) UHF measurement over entire period

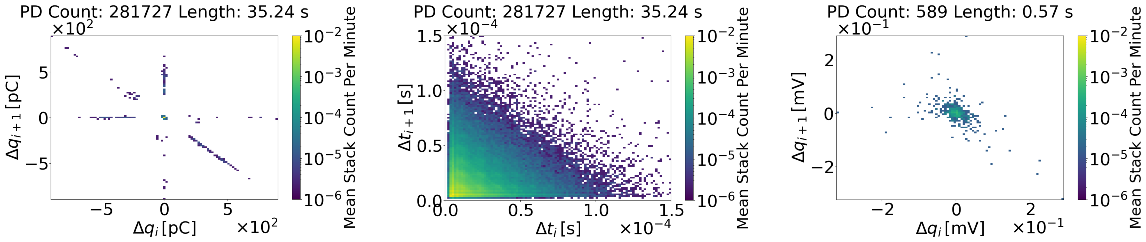

(d) MPD magnitude difference NoDi* plot [a]

(e) MPD time difference NoDi* plot [a]

(f) UHF magnitude difference NoDi* plot [c]

Figure 5.8: Plots of the second setup of the preliminary free metallic particle defect with the modified copper hoop and Particle 1 (4 mm) at -43 kV and 1 Bar absolute with firefly motion - Session 5

The particle containment configuration was further amended to address the lingering dead zones. The next section tackles the third setup, dealing with the stacked configuration.

Setup with Copper Hoop Stacked on Stainless Steel Lid

The third and final setup combined the copper hoop with the stainless steel lid, aiming to leverage the benefits of both designs. As with the previous setups, Particle 1 (4 mm) was subjected to various voltages to achieve liftoff. The test configuration is shown in Figure 5.9a, where Particle 1 (4 mm) was initially placed in the middle of the setup. The particle's final resting position is shown in Figure 5.9b. Polarity reversal was also tried as a potential method to initiate particle motion once the particle fell into a dead zone, but with no success.

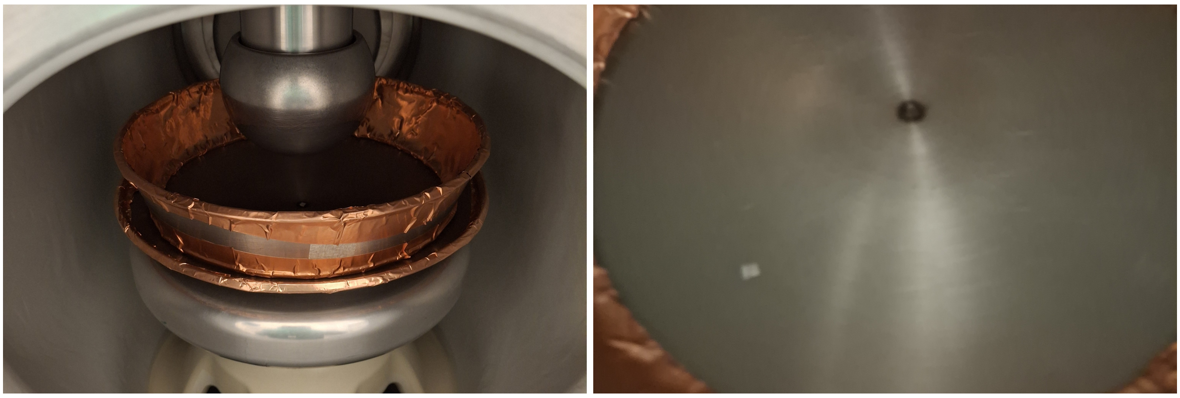

(a) Particle inside GIS test cell with stacked lid and hoop

(b) Final resting place of particle

Figure 5.9: Pictures of the third setup of the preliminary free metallic particle defect test phase with the stacked lid and hoop, and Particle 1 (4 mm)

The particle achieved liftoff at -47 kV during voltage ramp-up and at 3 Bar absolute. However, unlike the previous one in Figure 5.8d, the NoDi* pattern in Figure 5.10d reverted to the orientation initially observed in the first setup in Figure 5.4c. Since the orientation of the diagonals indicates voltage polarity, the observed tendency of the diagonals to flip under the same polarity can be attributed to the AC-like conditions under which the particle achieves liftoff. Regardless, the NoDi* pattern in Figure 5.10d unambiguously confirms that the particle underwent firefly motion.

A more detailed time-domain analysis of the MPD measurement, shown in Figure 5.10b, offers one of the clearest depictions of the characteristic PD activity associated with firefly motion. The distinct dip and subsequent rise in PD activity further validate this hypothesis. Additionally, the noise suppression benefits observed in the second setup with the copper hoop carried over to the third setup, as evidenced by the UHF measurement in Figure 5.10c. As experienced before in the second setup, the use of the copper hoop resulted in the dampening of EM waves, causing the UHF measurement to appear truncated and limiting the number of available data points.

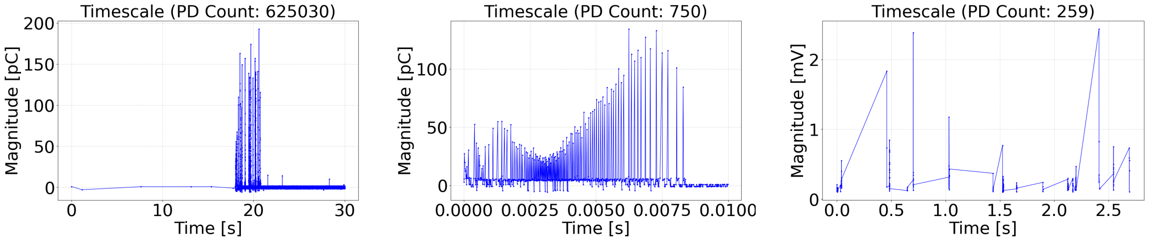

(a) MPD measurement over entire period

(b) Closeup of peaks [a]

(c) UHF measurement over entire period

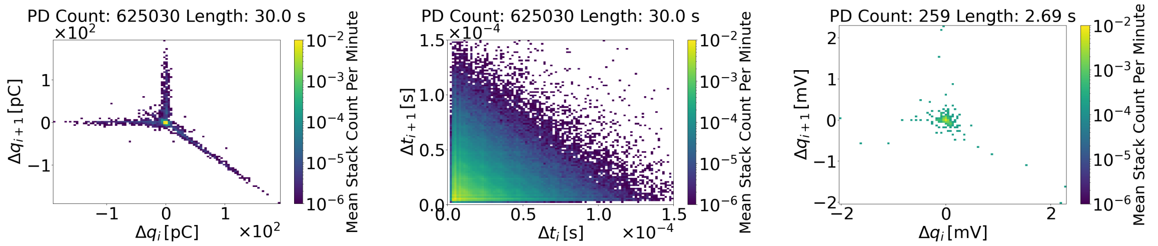

(d) MPD magnitude difference NoDi* plot [a]

(e) MPD time difference NoDi* plot [a]

(f) UHF magnitude difference NoDi* plot [c]

Figure 5.10: Plots of the third setup of the preliminary free metallic particle defect with stacked lid and copper hoop, and Particle 1 (4 mm) at -47 kV and 3 Bar absolute with firefly motion - Session 6

The voltage was increased to -65 kV, but no further PD activity followed upon voltage stabilization. Thereafter, the voltage was carefully reduced to zero, and the polarity of the HVDC source was reversed before gradually increasing the voltage back to the maximum operating level of 65 kV. While no particle motion was detected, PD activity exceeded the ambient noise levels, generating a NoDi* pattern, as shown in Figure 5.11b. This pattern suggests that the particle emitted PD pulses and has registered as a protrusion defect on the MPD instrument. The UHF device did not detect any PD activity.

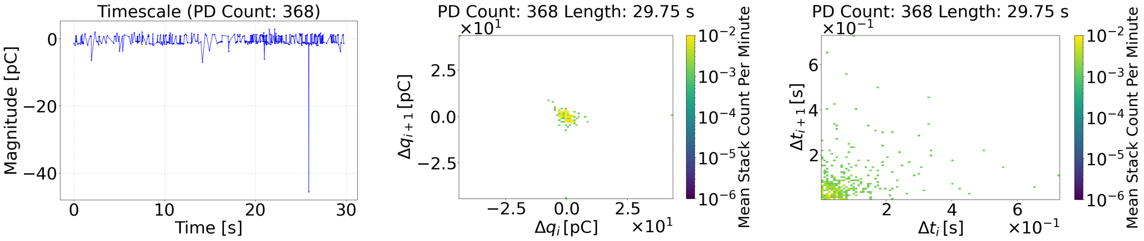

(a) MPD measurement over entire period **(b)** MPD magnitude difference NoDi* plot **(c)** MPD time difference NoDi* plot

Figure 5.11: Plots of the third setup of the preliminary free metallic particle defect with stacked lid and copper hoop, and Particle 1 (4 mm) at 65 kV and 3 Bar absolute - Session 7

The test run using the third test setup with the single particle provided the basis for another revision. While the particle was successfully contained and settled in a favorable position where it could emit PD pulses, its motion was not re-engaged, resulting in only a single observable firefly motion cycle. The intended outcome was to achieve continuous or, at a minimum, periodic particle motion. To address this, the decision was made to introduce the remaining nine particles from Figure 5.1 to promote a more gradual particle liftoff, leveraging the increased mass of the larger particles to delay their movement.

The revised version of the third test setup is depicted in Figure 5.12a. The ten particles were subjected to continuous voltage application at 50 kV overnight to better replicate the conditions expected in the long-term experiment. The final resting positions of the particles are shown in Figure 5.12b. Only two particles were ejected from the hoop and lid containment system.

(a) Placement of all ten particles **(b)** Final resting place of eight particles (with copper hoop removed)

Figure 5.12: Pictures of the third setup of the preliminary free metallic particle defect test phase with the stacked lid and hoop, and all ten particles

The voltage increase to 50 kV produced a significant response from the particles. PD measurements were conducted from the early afternoon into the evening on the first day of testing. During this period, a continuous stream of PD activity was recorded, interrupted by bursts of PD pulses with magnitudes significantly exceeding the background level, as evidenced by the peaks in Figure 5.13a. The UHF measurement in Figure 5.13d also displayed heightened activity. The NoDi* pattern in Figure 5.13b strongly indicated firefly motion as well as the one from the UHF data in Figure 5.13e. However, additional analysis was required to determine whether the motion of the larger particles and their subsequent PD activity overshadowed those of the smaller ones due to the differences in potential charge accumulation.

For a more consistent visual comparison, the magnitude difference NoDi* plots in Figure 5.13b, Figure 5.14b, Figure 5.15b, Figure 5.16d, and Figure 5.17b were scaled to a uniform limit of 310 pC. Similarly, the time difference NoDi* plots in Figure 5.13c, Figure 5.14c, Figure 5.15c, Figure 5.16e, and Figure 5.17c were uniformly scaled to a limit of 0.1 ms.

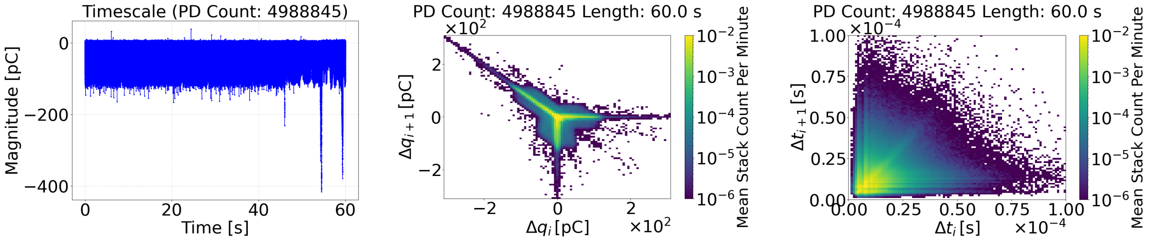

(a) MPD measurement over entire period **(b)** MPD magnitude difference NoDi* plot [a] **(c)** MPD time difference NoDi* plot [a]

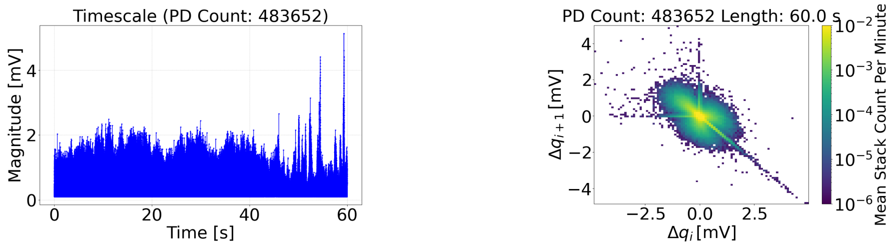

(d) UHF measurement over entire period **(e)** UHF magnitude difference NoDi* plot [d]

Figure 5.13: Plots of the third setup of the preliminary free metallic particle defect with stacked lid and copper hoop, and ten particles at 50 kV and 3 Bar absolute with firefly motion - Session 8

To investigate whether the motion of one set of particles overshadowed the residual PD activity, the PD measurement in Figure 5.13 was segmented into two sections: the first half capturing the baseline PD level and the second half containing the sharp peaks exceeding 400 pC. The initial thirty-second segment, representing the constant PD level, is presented in Figure 5.14. Conversely, the latter thirty-second segment, characterized by pronounced PD peaks, is shown in Figure 5.15.

Deconstructing the longer PD measurement revealed several interesting insights. Despite the shorter duration, the magnitude difference NoDi* plots still exhibit patterns characteristic of firefly motion. However, in the first segment shown in Figure 5.14b, the hovering motion nearly obscured the discernible firefly motion. Furthermore, the latter segment in Figure 5.15b emphasizes the effect of the sharp peaks, which reinforced the existing diagonals from the former thirty-second segment. This suggests that the intensified PD activity associated with the firefly motion dominates the final, longer pattern. Nevertheless, the defect classification remains unaffected as firefly motion prevails in both segments, though the precise nature warrants further investigation.

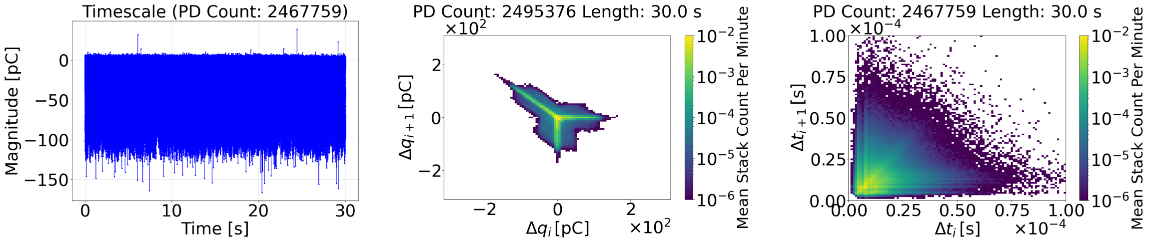

(a) MPD measurement over first half **(b)** MPD magnitude difference NoDi* plot **(c)** MPD time difference NoDi* plot

Figure 5.14: Plots of the third setup of the preliminary free metallic particle defect with stacked lid and copper hoop, and ten particles at 50 kV and 3 Bar absolute with firefly motion (first half of data from Session 8 in Figure 5.13a)

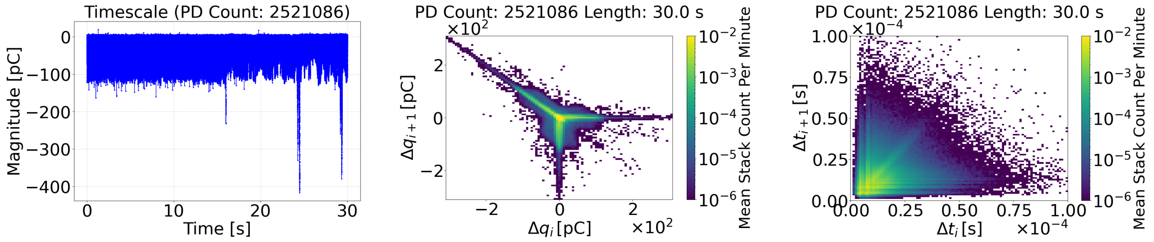

(a) MPD measurement over second half **(b)** MPD magnitude difference NoDi* plot **(c)** MPD time difference NoDi* plot

Figure 5.15: Plots of the third setup of the preliminary free metallic particle defect with stacked lid and copper hoop, and ten particles at 50 kV and 3 Bar absolute with firefly motion (second half of data from Session 8 in Figure 5.13a)

A more detailed analysis of the second segment was conducted, as illustrated in Figure 5.16, to isolate the peaks and examine the specific characteristics of the firefly motion. The magnitude difference NoDi* plot in Figure 5.16d captures only the PD activity directly related to firefly motion, suggesting that the previous two plots were influenced by PD activity associated with the hovering motion of the free metallic particle. Further distinction between the hovering and standing motion patterns is provided in the long-term experiment.

The timescale plot in Figure 5.16a further supports this conclusion, clearly depicting distinct PD behaviors representative of different firefly motion types. As shown in Figure 5.16a, the orange box highlights firefly motion with small jumping amplitudes, where the particle discharged before accumulating significant charge due to its proximity to the HV conductor. The green box corresponds to an interval where the particle exhibited firefly motion with large jumping amplitudes, as the increased distance from the HV conductor allowed it to charge more before discharge. The final purple area signifies a sequence of rapid collisions of the particle with the HV conductor, followed by large jumping amplitudes, as further detailed in Figure 5.16b. Naturally, it could not be determined whether it was the same particle witnessed in each stage.

This refined analysis of the sharp peaks observed in the original sixty-second segment in Figure 5.13 uncovers a complex interplay of particle motion, with certain patterns emerging over others.

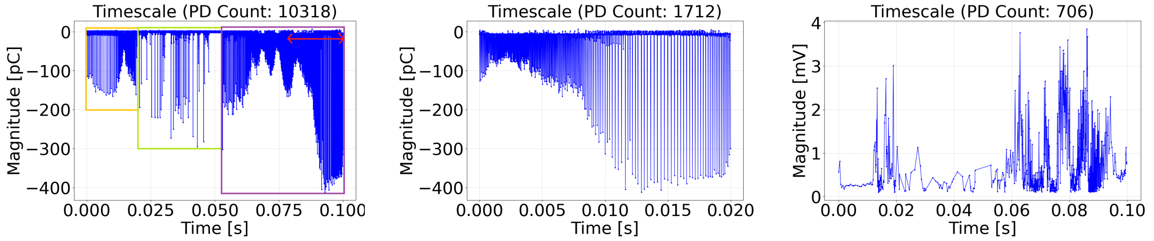

(a) MPD measurement of entire segment **(b)** Closeup of segment with red arrow [a] **(c)** UHF measurement of entire segment

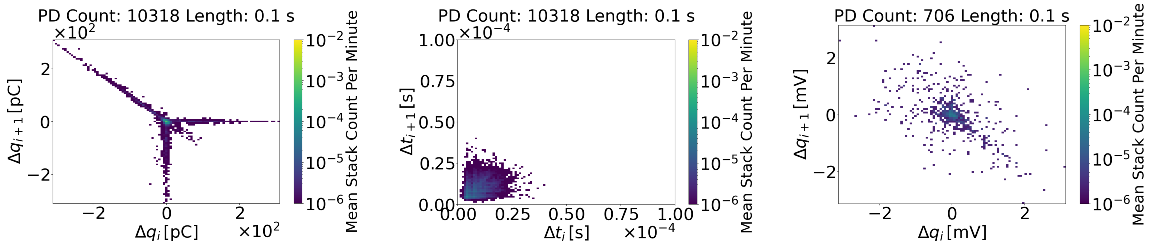

(d) MPD magnitude difference NoDi* plot [a] **(e)** MPD time difference NoDi* plot [a] **(f)** UHF magnitude difference NoDi* plot [c]

Figure 5.16: Plots of the third setup of the preliminary free metallic particle defect with stacked lid and copper hoop, and ten particles at 50 kV and 3 Bar absolute with firefly motion (100 ms segment of the second set of peaks in Figure 5.15a)

The voltage application continued overnight, and the PD measurement recorded in the morning is presented in Figure 5.17. The magnitude difference NoDi* plot in Figure 5.17b does not exhibit firefly motion, a conclusion further supported by the absence of UHF activity. However, the plot does display characteristics resembling the standing motion, consistent with the plot in the single particle test run in Figure 5.11b and observations from previous studies [24]. A comparison between Figure 5.17a and Figure 5.14a reveals that the residual PD activity has decreased fourfold overnight, suggesting that higher voltage levels may be required to sustain particle motion.

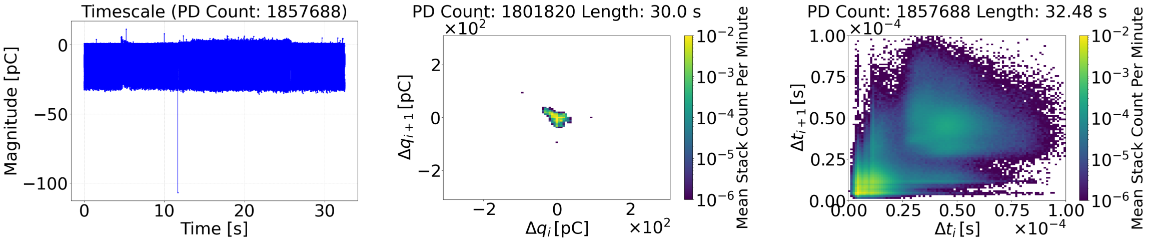

(a) MPD measurement over entire period **(b)** MPD magnitude difference NoDi* plot **(c)** MPD time difference NoDi* plot

Figure 5.17: Plots of the third setup of the preliminary free metallic particle defect with stacked lid and copper hoop, and ten particles at 50 kV and 3 Bar absolute after overnight voltage application with standing motion - Session 9

The test run with the third setup and all ten particles marked the final preliminary trial before the long-term experiment, offering valuable insights into particle behavior while fulfilling key objectives. The predefined particle length range was empirically verified with the given test conditions, with particles between 4 mm and 10 mm achieving liftoff. Firefly motion was successfully observed, and the particle containment system provided sufficient reinforcement to allow repeated motion. Additionally, the UHF device effectively captured PD activity near the HV conductor despite the blocking of EM waves by the copper hoop, and the overall noise level remained within an acceptable range.

However, the 5 mm particles, Particles 3 and 4, were ejected despite the containment system. To establish a comparison baseline, these particles were removed, leaving eight particles in the configuration for the long-term experiment. Similarly, removing the 5 mm particles increased the size and weight disparity between the 4 mm and 6 mm particles, potentially leading to distinct NoDi* patterns. The results of the long-term experiment are presented in the following section.

5.2.2. Long-Term Test Run

With the preliminary test runs completed, the long-term free metallic particle defect experiment was initiated, incorporating all the insights gained from previous trials. Particles 1–2 and 5–10 were placed on the stacked copper hoop and stainless steel lid configuration, as shown in Figure 5.18a, and subjected to a continuous voltage of 60 kV for one week. PD measurements were recorded twice daily throughout the experiment duration. By the end of the testing period, only the largest 10 mm particle remained, as illustrated in Figure 5.18b.

(a) Placement of eight particles inside GIS test cell **(b)** Final resting place with only Particle 10 visible

Figure 5.18: Pictures of the long-term free metallic particle defect experiment setup with the stacked lid and copper hoop and eight particles

The first three days were differentiated by periods with consistent PD activity ranging from 30 to 40 pC and periods interrupted by peaks reaching 100 to 150 pC. The MPD magnitude difference NoDi* plots in Figure 5.19d, Figure 5.20d, Figure 5.21b, Figure 5.22d, Figure 5.23d, Figure 5.24b, Figure 5.25b, Figure 5.26b, Figure 5.27b, and Figure 5.27e are scaled to 150 pC. Meanwhile, the MPD time difference NoDi* plots in Figure 5.19e, Figure 5.20e, Figure 5.21c, Figure 5.22e, Figure 5.23e, Figure 5.24c, Figure 5.25c, Figure 5.26c, and Figure 5.27f are scaled to 0.15 ms.

Day One

The morning measurement session recorded firefly motion as confirmed by the NoDi* pattern in Figure 5.19d, while a more detailed view in Figure 5.19b offers a better glimpse into the duration and type of the motion. The groupings of the large PD apparent charge magnitude peaks signify the firefly motion with small jumping amplitudes. The UHF data in Figure 5.19c captured the firefly motion with the initial large peak along with the subsequent standing motion on the HV conductor.

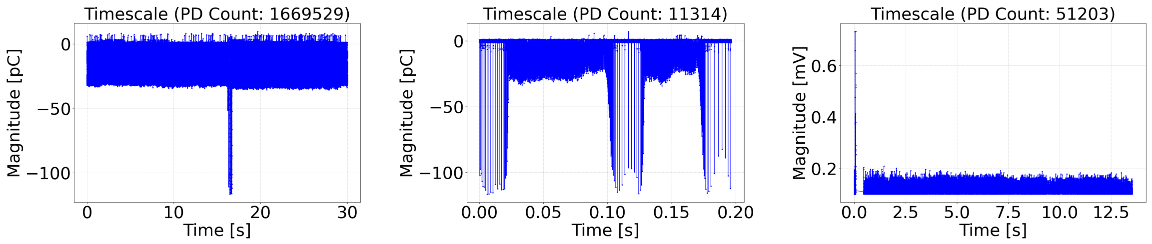

(a) MPD measurement over entire period **(b)** Closeup of peaks [a] **(c)** UHF measurement over entire period

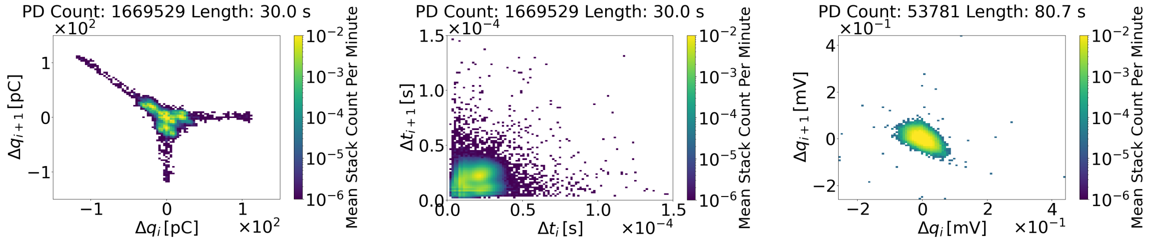

(d) MPD magnitude difference NoDi* plot [a] **(e)** MPD time difference NoDi* plot [a] **(f)** UHF magnitude difference NoDi* plot [c]

Figure 5.19: Plots of the long-term free metallic particle defect experiment with eight particles at 60 kV and 3 Bar absolute with firefly motion - day one first (morning) measurement

The afternoon session took place an hour after the morning session due to external experiments interfering later in the day and offered insight into the hovering motion, as seen in Figure 5.20b. The hovering motion occurs when the particle reaches an equilibrium between Coulomb and gravitational forces while remaining far enough from the HV conductor for space charge regions to significantly influence its charge accumulation. This explains the relatively low PD apparent charge magnitude values observed. Additionally, the UHF data, coupled with the absence of diagonals in the magnitude difference NoDi* plot in Figure 5.20d, further supports the hovering motion conclusion.

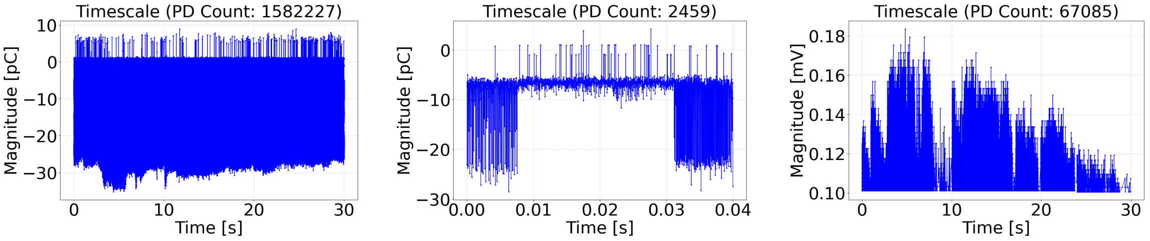

(a) MPD measurement over entire period **(b)** Closeup of MPD measurement [a] **(c)** UHF measurement over entire period

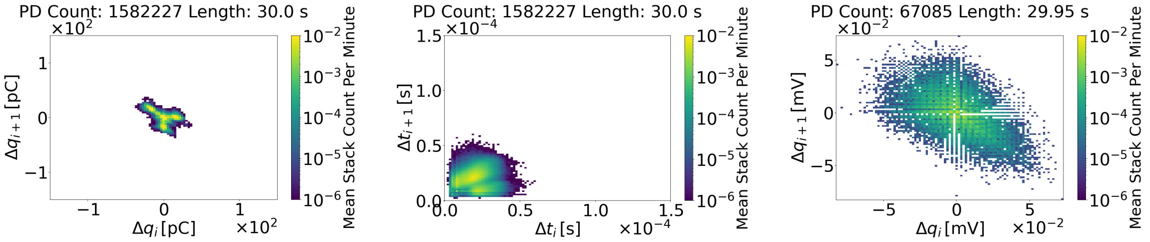

(d) MPD magnitude difference NoDi* plot [a] **(e)** MPD time difference NoDi* plot [a] **(f)** UHF magnitude difference NoDi* plot [c]

Figure 5.20: Plots of the long-term free metallic particle defect experiment with eight particles at 60 kV and 3 Bar absolute with hovering motion - day one second (afternoon) measurement

On days with either the hovering or standing motion, the UHF measurements were not always available as the UHF equipment tends to capture the PD activity occuring near the HV conductor.

Day Two

The order of the particle motion switched on the second day of PD measurement, with firefly motion occurring in the afternoon rather than the morning. Despite the lack of firefly motion in the morning measurement, the overall magnitude of the PD activity in Figure 5.21a increased slightly compared to the previous day in Figure 5.20a. The NoDi* pattern in Figure 5.21b suggests standing motion as further analysis of the timescale in Figure 5.21a and the lack of UHF activity does not support either hovering or firefly motion.

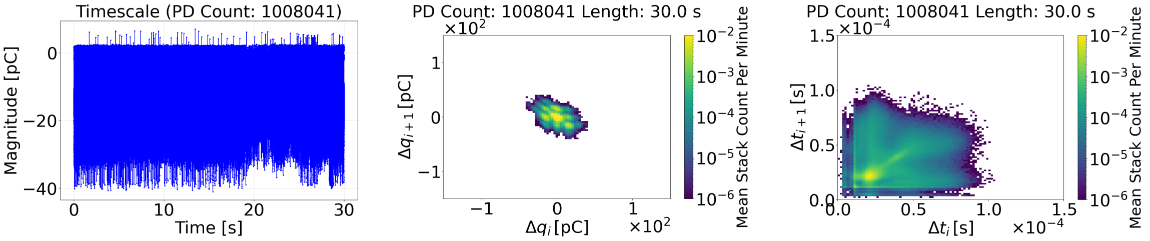

(a) MPD measurement over entire period **(b)** MPD magnitude difference NoDi* plot **(c)** MPD time difference NoDi* plot

Figure 5.21: Plots of the long-term free metallic particle defect experiment with eight particles at 60 kV and 3 Bar absolute with standing motion - day two first (morning) measurement

The afternoon session saw a resurgence of firefly motion with increased intensity, as reflected in the number of PD pulses detected in the MPD and UHF measurements. The MPD measurement shown in Figure 5.22a recorded the highest values among all the long-term sessions, suggesting that a particle other than the one observed on the first day in Figure 5.19a interacted with the HV conductor.

While the UHF measurement in Figure 5.22c also showed significant activity, it did not reach the highest values recorded in the long-term experiment. Nonetheless, the larger magnitude values, compared to those from the previous day in Figure 5.19c and Figure 5.20c, further support the hypothesis that a different particle underwent firefly motion. Additionally, the prolonged duration of the firefly motion, as illustrated in Figure 5.22b, compared to the first measurement on the first day in Figure 5.19b, reinforces this hypothesis.

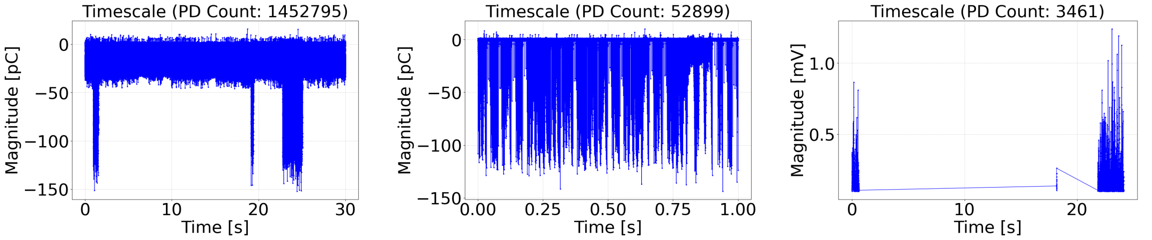

(a) MPD measurement over entire period **(b)** Closeup of third set of peaks [a] **(c)** UHF measurement over the entire period

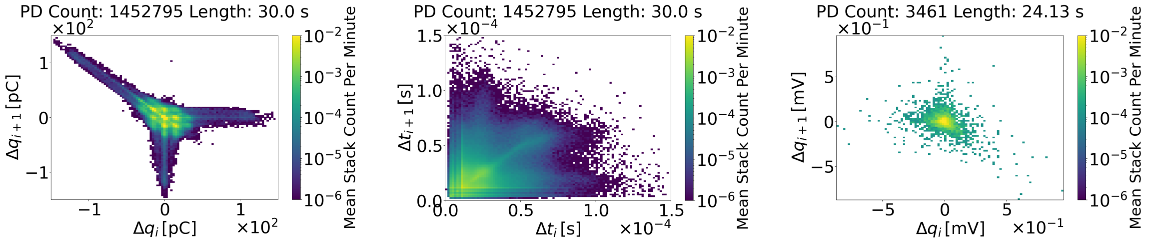

(d) MPD magnitude difference NoDi* plot [a] **(e)** MPD time difference NoDi* plot [a] **(f)** UHF magnitude difference NoDi* plot [c]

Figure 5.22: Plots of the long-term free metallic particle defect experiment with eight particles at 60 kV and 3 Bar absolute with firefly motion - day two second (afternoon) measurement

The assumption that a different particle was observed at the HV conductor during each session is based on the fact that only the 10 mm particle remained within the particle containment system. Additionally, as discussed later in Section 5.2.3, the particles exhibited minimal deformation, suggesting that their associated charge remained largely unchanged throughout the long-term voltage application, given that accumulated charge is proportional to length. Furthermore, the lack of firefly motion on Day Four could suggest that the lighter particles had already been ejected. However, further investigation through visual observation is necessary to confirm this hypothesis.

Day Three

On the third day of PD measurements, the occurrence of the firefly motion shifted again. The morning session recorded the longest firefly motion duration observed across all long-term PD measurement sessions, as shown in Figure 5.23a. Additionally, the UHF measurement in Figure 5.23c captured the highest magnitude values recorded throughout the experiment and aligned with peaks in Figure 5.23a, emphasizing the intensity of the PD activity. The extended duration of the firefly motion, coupled with the increased magnitude in the UHF measurement, suggests that a different particle than the one observed on the first day was responsible for the firefly motion. Still, the data regarding whether the particle differed from the one on the second day is inconclusive.

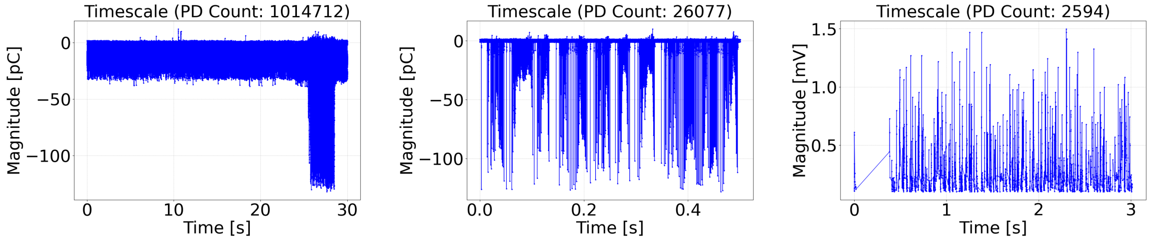

(a) MPD measurement over entire period **(b)** Closeup of peaks [a] **(c)** UHF measurement (MPD peak align)

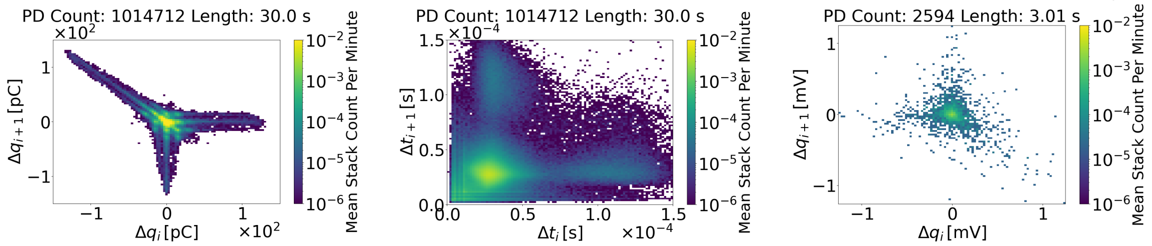

(d) MPD magnitude difference NoDi* plot [a] **(e)** MPD time difference NoDi* plot [a] **(f)** UHF magnitude difference NoDi* plot [c]

Figure 5.23: Plots of the long-term free metallic particle defect experiment with eight particles at 60 kV and 3 Bar absolute with firefly motion - day three first (morning) measurement

The afternoon saw the return of the standing motion, owing to the characteristic NoDi* pattern in Figure 5.24b and the lack of UHF activity. The residual PD activity also saw a slight decrease in overall values when compared to the previous day in Figure 5.21a.

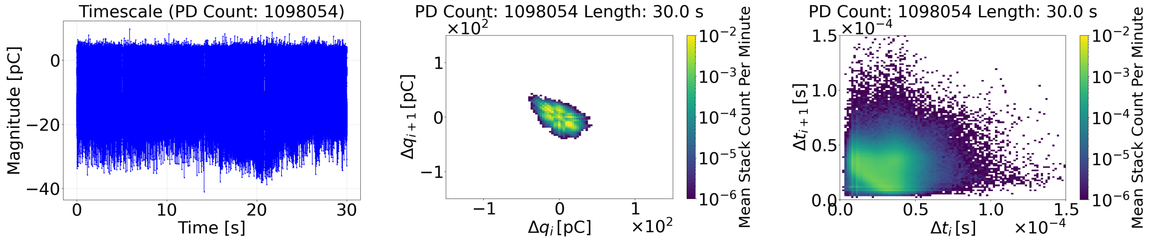

(a) MPD measurement over entire period **(b)** MPD magnitude difference NoDi* plot **(c)** MPD time difference NoDi* plot

Figure 5.24: Plots of the long-term free metallic particle defect experiment with eight particles at 60 kV and 3 Bar absolute with standing motion - day three second (afternoon) measurement

Day Four

The fourth day saw a complete lack of firefly motion and UHF activity across the two recorded sessions. The morning measurement experienced more of the standing motion as confirmed by the NoDi* pattern in Figure 5.25b and further analysis of the time scale plot in Figure 5.25a.

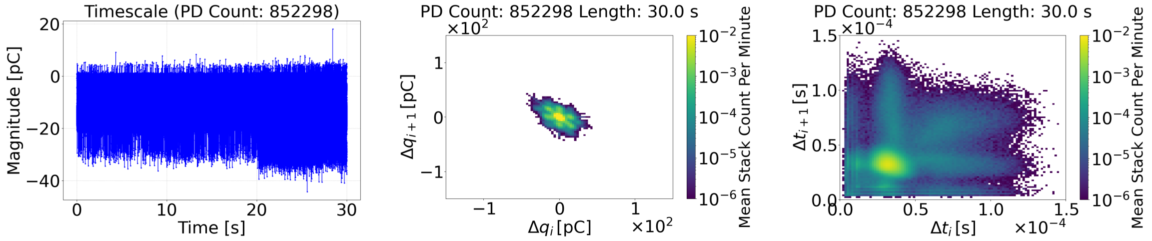

(a) MPD measurement over entire period **(b)** MPD magnitude difference NoDi* plot **(c)** MPD time difference NoDi* plot

Figure 5.25: Plots of the long-term free metallic particle defect experiment with eight particles at 60 kV and 3 Bar absolute with standing motion - day four first (morning) measurement

Although a similar NoDi* pattern was observed in Figure 5.26b, a closer examination of the time scale plot from the afternoon session in Figure 5.26a indicated the hovering motion. These two recorded sessions highlight an important distinction when identifying two commonly observed particle behaviors. While the NoDi* patterns for standing motion in Figure 5.25b and hovering motion in Figure 5.26b share a similar overall outline, they differ in the distribution of peak concentrations within their respective shapes. These findings underscore the need for further investigation into NoDi* patterns across different particle motions. Likewise, the complete absence of UHF data cannot be reliably used as a tool to distinguish between standing and hovering motion.

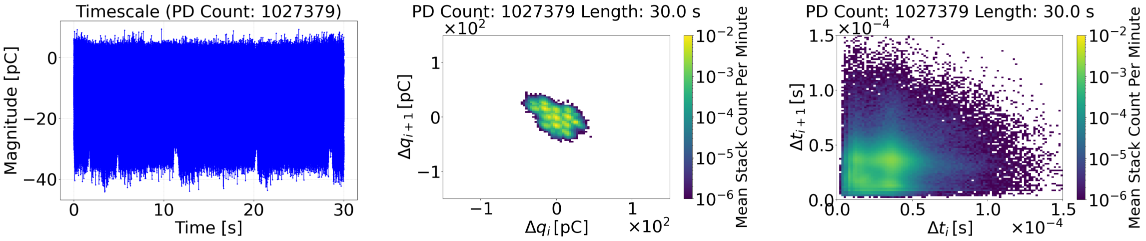

(a) MPD measurement over entire period **(b)** MPD magnitude difference NoDi* plot **(c)** MPD time difference NoDi* plot

Figure 5.26: Plots of the long-term free metallic particle defect experiment with eight particles at 60 kV and 3 Bar absolute - day four second (afternoon) measurement

Unfortunately, Day Four landed on a Friday, so PD measurement had to resume on the following Monday. Automatic reporting functionality was not implemented in the limited time allocated for the long-term experiments.

Day Seven

Day seven marked the final day of PD measurements in the long-term experiment on the free metallic particle defect due to the near-absence of PD activity. The lack of UHF activity was anticipated based on the previous three measurement sessions; however, the significant reduction in the number of PD pulses within the standard 30-second period suggested that all particles had settled. Extending the PD measurement duration to 120 seconds revealed the standing motion pattern, as illustrated in Figure 5.27e. This observation was further confirmed through a physical inspection of the test setup, which identified the presence of Particle 10 (10 mm).

These findings underscore an important consideration: while a 30-second measurement period was generally sufficient for generating NoDi* patterns in most PD measurements, it may impose limitations on defect classification in specific cases. Additionally, increasing the number of PD pulses does not always yield clearer plots, as demonstrated in the comparison between Figure 5.15b and Figure 5.16d, a topic further explored in the protrusion defect section.

The time difference NoDi* plot of the extended PD measurement in Figure 5.27f further suggests the ability of the remaining particle to generate rapid PD pulses. Meanwhile, the time scale plot in Figure 5.27d provides better insight into the magnitude of these discharges.

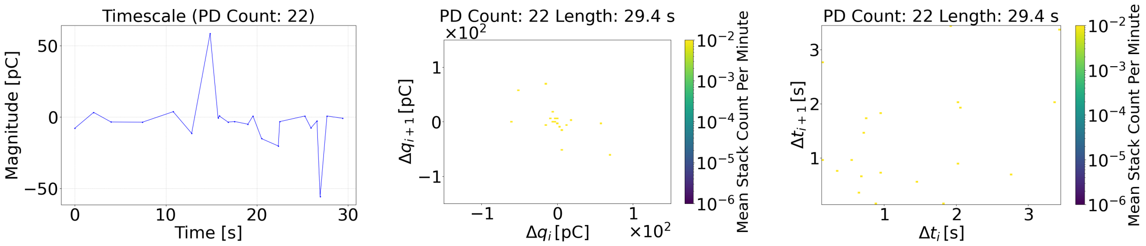

(a) MPD measurement over 30 s period **(b)** MPD magnitude difference NoDi* plot [a] **(c)** MPD time difference NoDi* plot [a]

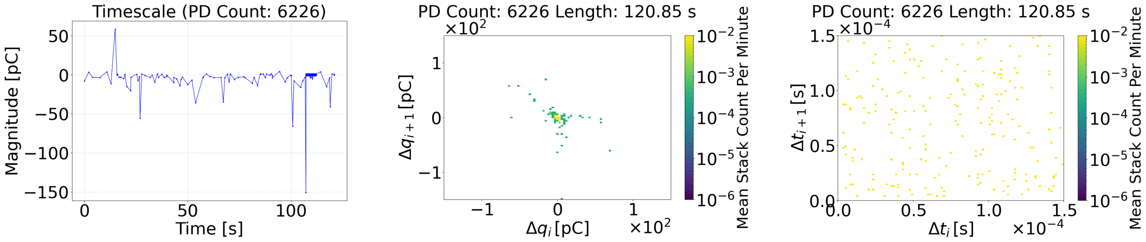

(d) MPD measurement over 120 s period **(e)** MPD magnitude difference NoDi* plot [d] **(f)** MPD time difference NoDi* plot [d]

Figure 5.27: Plots of the long-term free metallic particle defect experiment with eight particles at 60 kV and 3 Bar absolute with standing motion (30 s measurement [a], [b], and [c] and 120 s measurement [d], [e], and [f] - day seven

The particles were collected from their final resting places within the GIS test cell and taken to the microscope lab within the SINTEF facilities at NTNU. One particle was even found at the base of the UHF antenna, emphasizing the significant horizontal force experienced by the particle.

5.2.3. Particle Erosion

The long-term experiment would not be complete without microscopic analysis and a final weigh-in. All ten particles, as shown in Figure 5.1, were weighed, measured, and photographed under the microscope after the last PD measurement on day seven. It is important to note that Particles 3 and 4 were not included in the long-term experiment.

Upon examining the photographs of every particle, no immediate visual differences between the before and after states were apparent. Lighting in each photograph played a crucial role, as the absence of distinguishing features made it even more challenging to produce accurate comparative images. The microscope images of Particle 1 (4 mm) are shown in Figure 5.28a and Figure 5.28b, as it was exposed to voltage application for a longer duration than the other particles. In this particular case, an increase in the general surface roughness was observed, but no definitive change in the tip radius was evident, as noted in the protrusion defect by T. Vu-Cong et al. [10] in their long-term study.

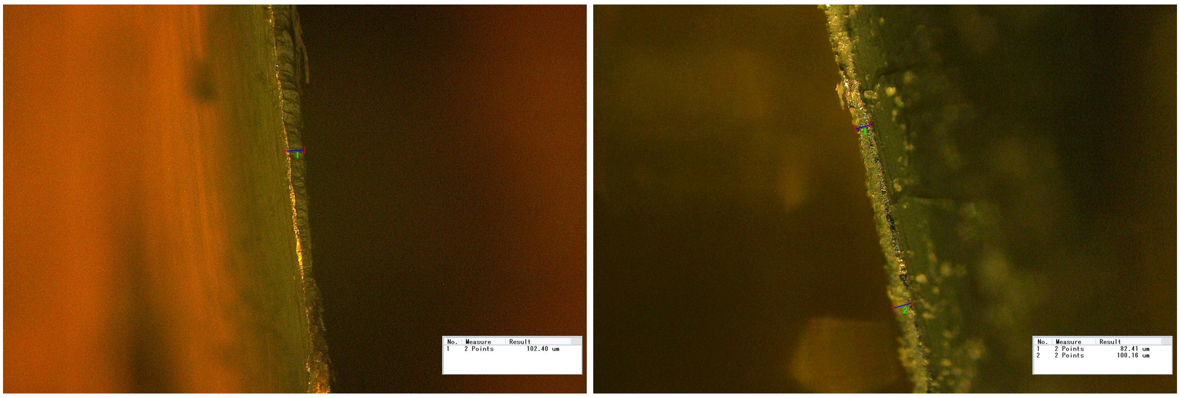

(a) Before the preliminary and long-term experiments **(b)** After the preliminary and long-term experiments

Figure 5.28: Microscope imaging of Particle 1 (4 mm) under 100x magnification

After microscope imaging, weight measurements were taken using a scale with 0.01 mg accuracy, with both the initial and final values presented in Table 5.4. Unlike the visual assessment of the microscope images, the recorded weight differences indicate a change in overall composition, with particles losing between 0.01 and 0.05 mg. Notably, Particle 1 (4 mm) exhibited the most significant weight loss, likely due to the prolonged voltage application.

Table 5.4: Weights of the particles after the long-term free metallic particle defect experiment

Weight (mg)	Particle 1 (4 mm)	Particle 2 (4 mm)	Particle 3 (5 mm)	Particle 4 (5 mm)	Particle 5 (6 mm)	Particle 6 (6 mm)	Particle 7 (7 mm)	Particle 8 (7 mm)	Particle 9 (8 mm)	Particle 10 (10 mm)
Before	8.69	9.29	11.62	11.17	12.41	13.27	13.81	14.56	17.38	20.99
After	8.64	9.25	11.61	11.18	12.38	13.25	13.78	14.54	17.37	20.97
Difference (%)	-0.05 (-0.57 %)	-0.04 (-0.32 %)	-0.01 (-0.08 %)	0.01 (0.08 %)	-0.03 (-0.24 %)	-0.02 (-0.15 %)	-0.03 (-0.21 %)	-0.02 (-0.13 %)	-0.01 (-0.06 %)	-0.02 (-0.09 %)

Although no tip radius erosion was observed, the free metallic particles must be considered separately from the protrusion defect. PD activity is more dispersed along the edges of free metallic particles due to their dynamic orientation caused by the subsequent motion. Consequently, the 20 to 25 µm changes in the tip radius reported in the long-term study by T. Vu-Cong et al. [10] at significantly higher voltages are not confined to a single region. Instead, weight measurements provide a more reliable indication of changes in particle composition and overall PD behavior. With this context, the next section focuses on the protrusion defect.

5.3. Protrusion Defect

The investigation of the protrusion defect builds upon the findings and insights gained from the study of the free metallic particle defect. A 4 mm length was selected as the optimal height for the protrusion. A free metallic particle of 4 mm has been observed to achieve the standing motion in the given electrode configuration and aligns with the most commonly encountered defect size in GIS systems [45].

To assess the long-term behavior of the protrusion defect, it was subjected to a sustained voltage of 65 kV for one week, followed by a detailed physical examination focusing on changes in the tip radius using microscope imaging. Before this long-term study, preliminary tests were conducted to analyze the effects of space charge accumulation and voltage reversal. These tests were carried out in two phases. The first involved a continuous 24-hour voltage application at 3 bar absolute pressure. The second consisted of a batch of tests under varying pressures and voltage polarities to evaluate their impact on PD behavior and confirm the trends expressed in Figure 3.1.

5.3.1. Preliminary Test Phase Concerning Overnight Voltage Application

The exact test parameters of each session within the first preliminary test phase are shown in Table 5.5. The detailed table provides approximate timestamps for each PD measurement meant to analyze space charge accumulation, especially after polarity reversal.

Table 5.5: Testing schedule for preliminary test phase concerning overnight voltage application of protrusion defect

Pressure Absolute (Bar)	Polarity (Sign)	PDIV (kV)	Voltage Tested (kV)	Calibration Factor	Time (HH:MM)	Time Difference	Day	Action	Report Label
3	+	52.5	55.1	6.10721	14:22		Day 1	Voltage Interrupted	Session 1
3	-	57.5	58.1	6.10721	11:30		Day 2		Session 2
3	-	57.5	63.1	6.10721	11:45	0:15	Day 2		Session 3
3	-	57.5	63.1	6.10721	12:15	0:30	Day 2		Session 4
3	-	57.5	63.1	6.10721	13:15	1:00	Day 2		Session 5
3	-	57.5	65.1	6.10721	13:45	0:30	Day 2		Session 6
3	-	57.5	65.1	6.10721	14:15	0:30	Day 2		Session 7
3	-	57.5	65.1	6.10721	15:15	1:00	Day 2		Session 8
3	+	52.5	64.1	6.10721	16:30	1:15	Day 2		Session 9
3	+	52.5	64.1	6.10721	18:00	1:30	Day 2		Session 10
3	+	52.5	64.1	6.10721	21:00	3:00	Day 2	Voltage Continued	Session 11
3	+	52.5	64.1	6.10721	9:00	12:00	Day 3		Session 12

To create the protrusion defect, a 10 mm aluminum particle, shown in Figure 5.29b, was carefully bent in half and secured to the ground electrode inside the GIS test cell using electrical tape, as illustrated in Figure 5.29a. The aluminum shaving originated from the same batch as those used for the free metallic particle defect, ensuring consistency in material properties. Special care was taken during the bending process to achieve a precise 4 mm height from the base of the ground electrode. However, the same level of caution was not observed when removing and attempting to straighten the particle, leading to breakage near the tip.

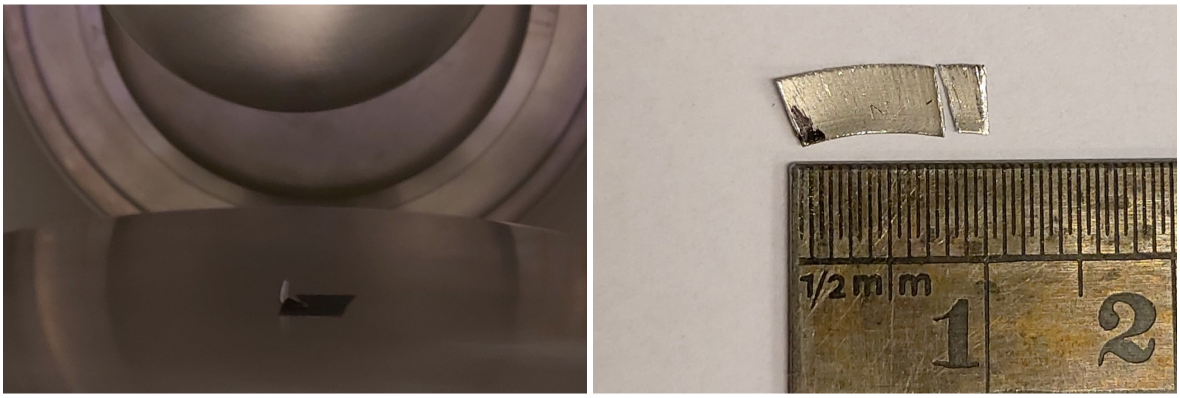

(a) Placement of the protrusion defect inside GIS test cell **(b)** 10 mm particle used (with broken tip visible)

Figure 5.29: Preliminary test phase concerning overnight voltage application of protrusion defect

For clarity and ease of comparison, the following three subsections categorize the measurement sessions listed in Table 5.5 based on the key aspects analyzed. The first section focuses on the primary results of the overnight voltage application. The subsequent sections examine the effects of polarity reversal, owing to the intermediate negative voltage application.

Positive Polarity with Overnight Application

After positioning the protrusion defect inside the GIS test cell, a voltage of 55 kV was applied for half a day, and the PD measurement shown in Figure 5.30 was recorded. Testing was then paused over the weekend. On the following Monday, a negative voltage was applied before switching back to a positive voltage later in the day. The PD measurement in Figure 5.31 represents the final reading before the setup was left to run continuously. Subsequently, the PD measurement in Figure 5.32 was taken after 12 hours of uninterrupted voltage application.

The magnitude difference NoDi* plots in Figure 5.30b, Figure 5.31b, and Figure 5.32b have been scaled to 70 pC. Meanwhile, the time difference NoDi* plots in Figure 5.30c, Figure 5.31c, and Figure 5.32c have been uniformly scaled to 1 ms.

The magnitude difference NoDi* pattern in Figure 5.30b closely resembles the standing motion particle pattern observed earlier in the free metallic particle defect in Figure 5.3b and reported in literature [41].

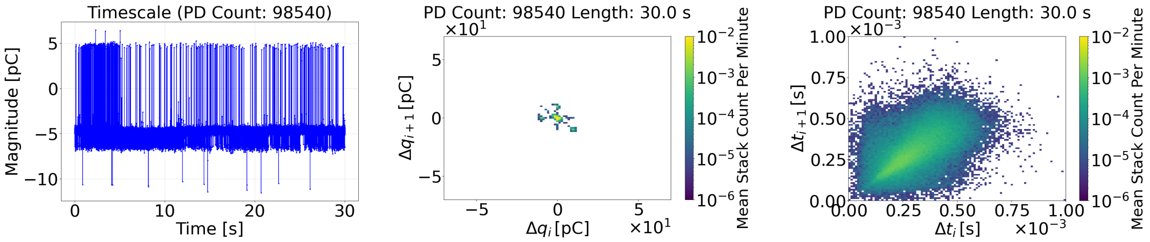

(a) MPD measurement over entire period **(b)** MPD magnitude difference NoDi* plot **(c)** MPD time difference NoDi* plot

Figure 5.30: Plots of the preliminary protrusion defect test run regarding overnight voltage application at 55 kV and 3 Bar absolute - session 1

After ten hours of continuous voltage application that was interrupted only for an hour during the polarity switch, the maximum PD apparent charge magnitude values at the end of the day, as shown in Figure 5.31a, remained relatively unchanged from the initial measurement on the first day in Figure 5.30a. However, the overall residual PD activity has increased, resulting in a more defined and filled-in NoDi* pattern in Figure 5.31b.

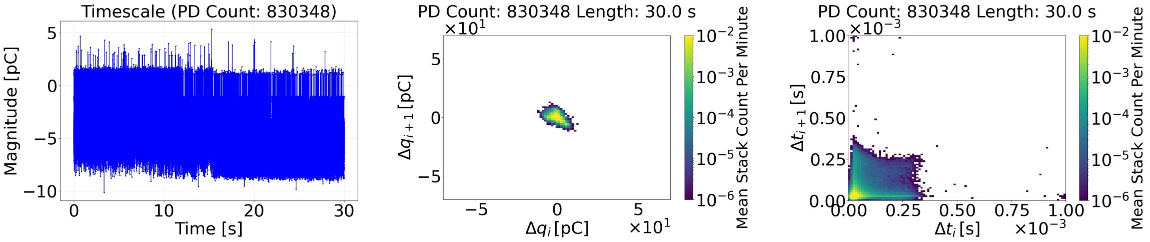

(a) MPD measurement over entire period

(b) MPD magnitude difference NoDi* plot

(c) MPD time difference NoDi* plot

Figure 5.31: Plots of the preliminary protrusion defect test run regarding overnight voltage application at 64 kV and 3 Bar absolute - Session 11

The final PD measurement of the preliminary overnight voltage application test phase exhibited a notable shift from the previous sessions. The magnitude difference NoDi* plot in Figure 5.32b showed a substantial increase in overall values, with some exceeding 70 pC, as illustrated in Figure 5.32a. Similarly, the UHF measurement reflected this trend, capturing significant PD activity, as seen in Figure 5.32e and Figure 5.32d. Even within the relatively short period, the PD apparent charge magnitude saw a substantial increase, reinforcing the findings of the long-term study by T. Vu-Cong et al. [10].

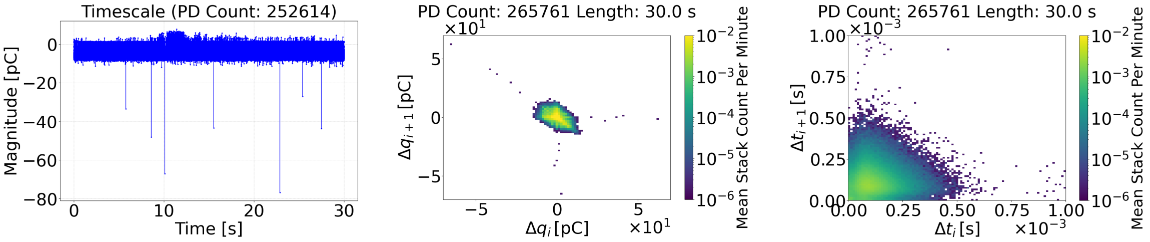

(a) MPD measurement over entire period

(b) MPD magnitude difference NoDi* plot [a]

(c) MPD time difference NoDi* plot [a]

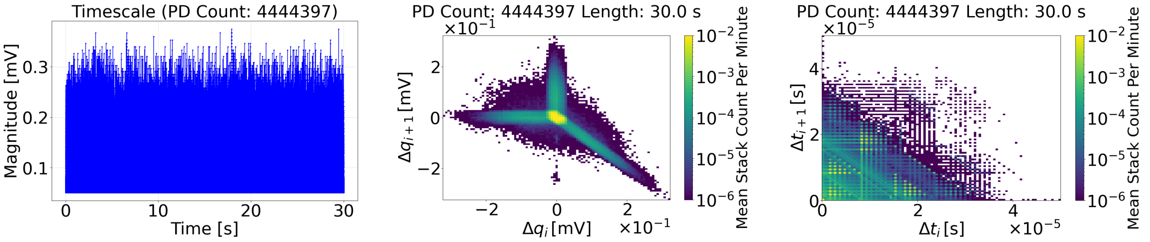

(d) UHF measurement over entire period

(e) UHF magnitude difference NoDi* plot [d]

(f) UHF time difference NoDi* plot [d]

Figure 5.32: Plots of the preliminary protrusion defect test run regarding overnight voltage application at 64 kV and 3 Bar absolute - Session 12

The next two subsections analyze the PD measurements under negative polarity and the effect of polarity reversal on the space charge regions surrounding the protrusion defect.

Negative Polarity

The voltage polarity was reversed between the initial and final positive voltage applications. After the positive voltage application on the first day, the voltage was interrupted over the weekend before applying negative voltage the following Monday. This voltage interruption aimed to mitigate the potential effects of space charge accumulation and decomposition byproducts.

The magnitude difference NoDi* plots in Figure 5.33b, Figure 5.34b, and Figure 5.35b have been scaled to 30 pC. Meanwhile, the time difference NoDi* plots in Figure 5.33c, Figure 5.34c, and Figure 5.35c have been uniformly scaled to 1 ms.

Switching to negative polarity after three days of voltage interruption produced notable results. A settling phenomenon was observed across three measurement sessions, separated by intervals of thirty and sixty minutes, respectively, accompanied by a decline in UHF activity. Within just thirty minutes, UHF activity was reduced by half, as seen in Figure 5.33d and Figure 5.34d.

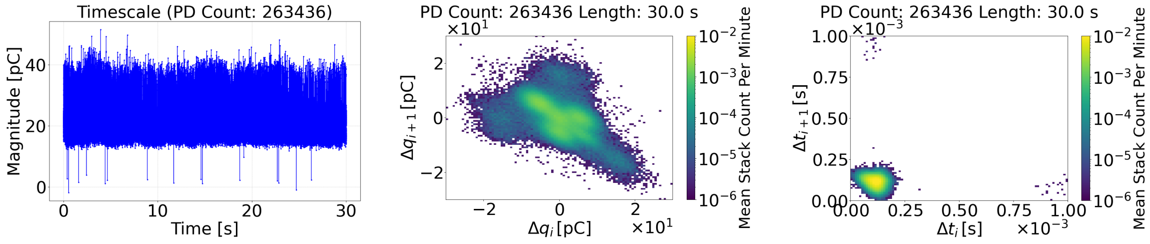

(a) MPD measurement over entire period **(b)** MPD magnitude difference NoDi* plot [a] **(c)** MPD time difference NoDi* plot [a]

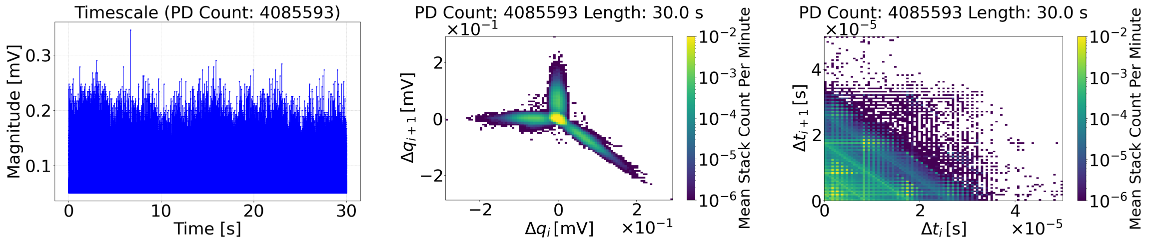

(d) UHF measurement over entire period **(e)** UHF magnitude difference NoDi* plot [d] **(f)** UHF time difference NoDi* plot [d]

Figure 5.33: Plots of the preliminary protrusion defect test run regarding overnight voltage application at -63 kV and 3 Bar absolute - Session 3

The fourth session produced a magnitude difference NoDi* plot shown in Figure 5.34b that resembles the standing motion of a free metallic particle defect, indicating that proper defect classification cannot always rely on the first PD measurement.

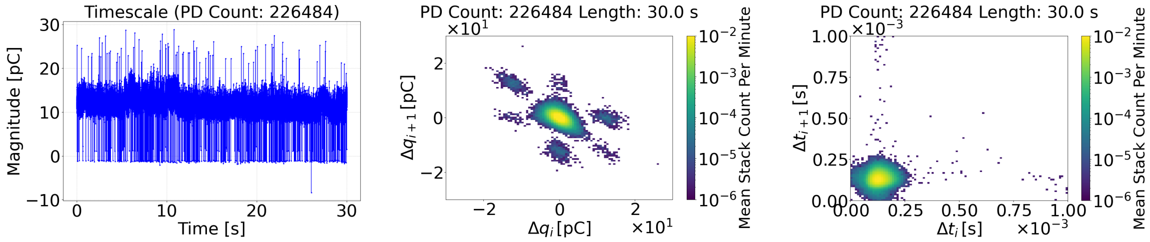

(a) MPD measurement over entire period **(b)** MPD magnitude difference NoDi* plot [a] **(c)** MPD time difference NoDi* plot [a]

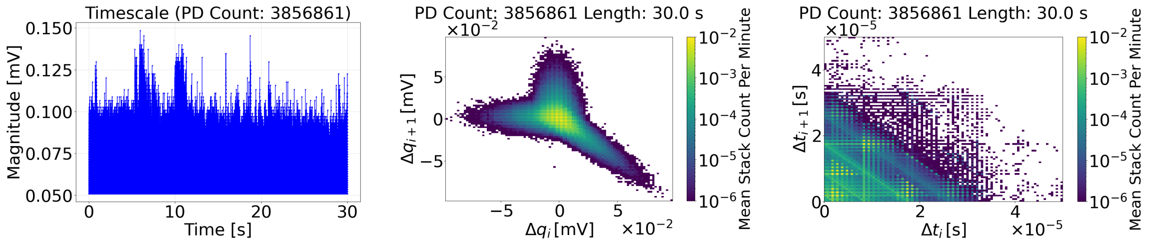

(d) UHF measurement over entire period **(e)** UHF magnitude difference NoDi* plot [d] **(f)** UHF time difference NoDi* plot [d]

Figure 5.34: Plots of the preliminary protrusion defect test run regarding overnight voltage application at -63 kV and 3 Bar absolute - Session 4

UHF activity was completely absent in the fifth session, and the magnitude difference NoDi* pattern in Figure 5.35b became further refined. The MPD measurement also exhibited a sharp reduction in the number of PD pulses, accompanied by a significant increase in the time interval between pulses. This trend is clearly illustrated in the wider view shown in Figure 5.35d.

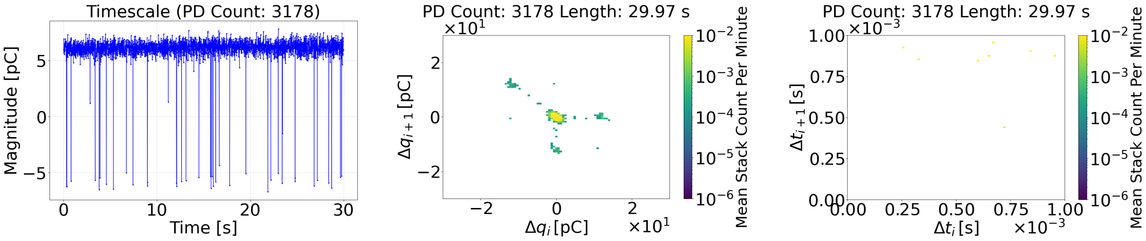

(a) MPD measurement over entire period **(b)** MPD magnitude difference NoDi* plot **(c)** MPD time difference NoDi* plot

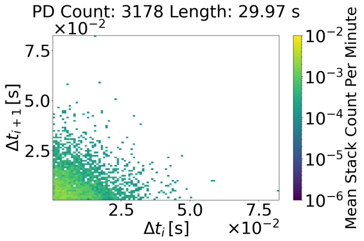

(d) Wider view of the time difference plot [c]

Figure 5.35: Plots of the preliminary protrusion defect test run regarding overnight voltage application at -63 kV and 3 Bar absolute - Session 5

The test runs with negative voltage application highlighted the influence of AC-like conditions and the subsequent redistribution of space charge until equilibrium was reached. At this point, the protrusion defect exhibited a characteristic standing motion pattern. The following subsection analyzes the NoDi* pattern immediately after a polarity reversal.

Voltage Polarity Reversal

The eighth, ninth, and tenth sessions in Figure 5.36, Figure 5.37, and Figure 5.38 provide a glimpse into the PD behavior before and after voltage reversal.

The magnitude difference NoDi* plots in Figure 5.36b, Figure 5.37b, and Figure 5.38b have been scaled to 40 pC. Meanwhile, the time difference NoDi* plots in Figure 5.37c, Figure 5.38c have been scaled to 0.2 ms. The time difference NoDi* plot in Figure 5.36c was not scaled as the time interval between PD pulses was too large.

The magnitude difference NoDi* plot in Figure 5.36b matches the characteristic pattern of the standing motion of a free metallic particle and shows considerable development from the plot of the previous session in Figure 5.35b, which occurred some two hours earlier. However, the change in the time difference plots between Figure 5.36c and Figure 5.35d is less noticeable.

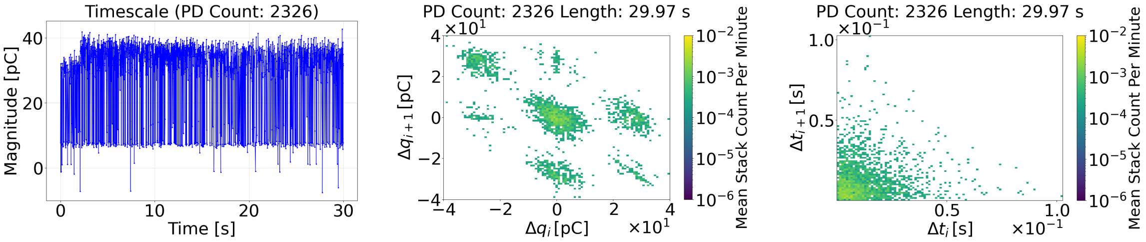

(a) MPD measurement over entire period **(b)** MPD magnitude difference NoDi* plot **(c)** MPD time difference NoDi* plot

Figure 5.36: Plots of the preliminary protrusion defect test run regarding overnight voltage application at -65 kV and 3 Bar absolute - Session 8

The voltage was switched to positive polarity in Session 9, as shown in Figure 5.37. The magnitude difference NoDi* plot in Figure 5.37b clearly illustrates the mirroring of the diagonals as a direct result of the polarity reversal. Notably, the magnitude values have also decreased significantly, likely due to the redistribution of space charge regions.

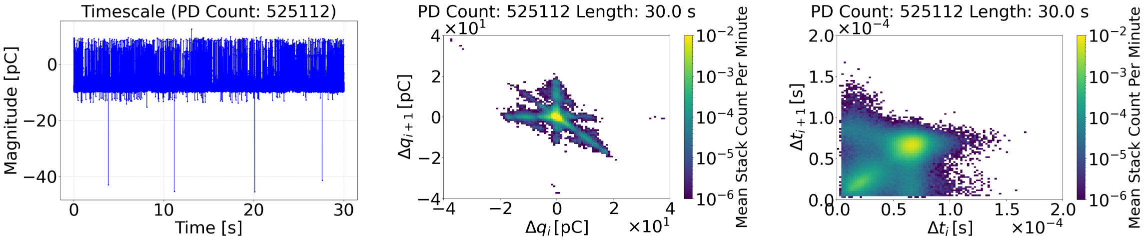

(a) MPD measurement over entire period **(b)** MPD magnitude difference NoDi* plot **(c)** MPD time difference NoDi* plot

Figure 5.37: Plots of the preliminary protrusion defect test run regarding overnight voltage application at 64 kV and 3 Bar absolute - Session 9

The continuation of the positive voltage application exhibited a similar trend to the negative voltage case. Initially, the PD apparent charge magnitude values experienced a decline before gradually increasing again over time. This resurgence became evident after an extended duration, with the most noticeable change occurring overnight. The magnitude difference NoDi* plot in Figure 5.38b continues to show the characteristic standing motion, albeit with a more filled-in shape.

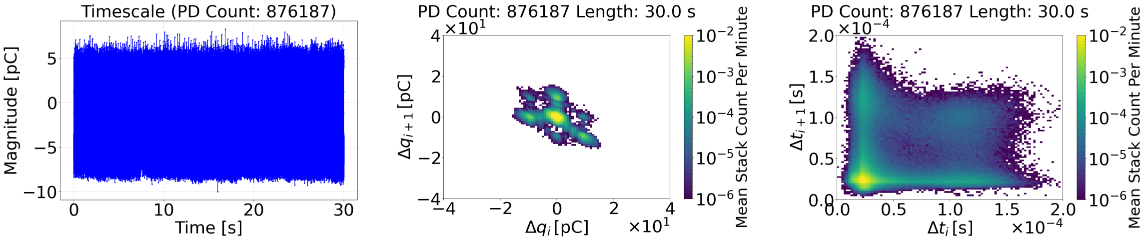

(a) MPD measurement over entire period **(b)** MPD magnitude difference NoDi* plot **(c)** MPD time difference NoDi* plot

Figure 5.38: Plots of the preliminary protrusion defect test run regarding overnight voltage application at 64 kV and 3 Bar absolute - Session 10

The next section discusses the second round of preliminary testing regarding the protrusion defect.

5.3.2. Preliminary Test Phase Concerning Overnight Voltage Interruption

The initial round of preliminary testing left certain aspects unexamined. Specifically, the combined effects of pressure variations and voltage interruptions were not fully addressed. To bridge this gap, a round-robin series of tests was proposed to investigate PD behavior comprehensively and identify any significant traits or characteristics that could be further explored in the long-term experiment.

A new 10 mm particle was fabricated, as depicted in Figure 5.39b, and placed inside the GIS test cell, shown in Figure 5.39a. Initially, microscope imaging was performed on the protrusion defects used in the preliminary tests, but the focus was on the side surfaces rather than the tip. This realization was incorporated into the long-term experiment, where the tip was examined under the microscope for a more detailed assessment.

(a) Placement of the protrusion defect inside GIS test cell

(b) 10 mm particle used

Figure 5.39: Preliminary test phase concerning overnight voltage interruption of protrusion defect

The specific test parameters for each PD measurement in the round-robin test series are detailed in Table 5.6. A total of four voltage interruptions were performed. However, the final two interruptions closely resembled those conducted during the overnight voltage application test phase and did not yield any new insights.

The two selected voltage interruptions included one at 1 Bar absolute and another that investigated the effects of voltage interruption before and after pressurizing the GIS test cell from 1 Bar to 3 Bar absolute.

Table 5.6: Testing schedule for preliminary test phase concerning voltage interruption of the protrusion defect

Pressure Absolute (Bar)	Polarity (Sign)	PDIV (kV)	Voltage Tested (kV)	Calibration Factor	Time (HH:MM)	Time Difference	Day	Action	Report Label
1	+	26.5	35.1	6.26274	15:00		Day 1		Session 1
1	+	26.5	35.1	6.26274	15:30	0:30	Day 1		Session 2
1	+	26.5	35.1	6.26274	16:00	0:30	Day 1	Voltage Interrupted	Session 3
1	+	26.5	35.1	6.26274	13:20		Day 2		Session 4
1	+	26.5	35.1	6.26274	13:50	0:30	Day 2		Session 5
1	+	26.5	40.1	6.26274	14:20	0:30	Day 2		Session 6
1	+	26.5	40.1	6.26274	14:50	0:30	Day 2	Voltage Interrupted	Session 7
3	+	51.7	55.1	6.26274	16:00		Day 3		Session 8
3	+	51.7	55.1	6.26274	16:10	0:10	Day 3		Session 9
3	+	51.7	52.5	6.26274	16:20	0:10	Day 3		Session 10
3	+	51.7	60.1	6.26274	16:40	0:20	Day 3		Session 11
3	+	51.7	62.1	6.26274	17:00	0:20	Day 3	Voltage Interrupted	Session 12
3	-	57.5	65.1	6.26274	17:00		Day 4		Session 13
3	-	57.5	65.1	6.26274	17:30	0:30	Day 4		Session 14
3	-	57.5	65.1	6.26274	18:00	0:30	Day 4		Session 15
3	-	57.5	65.1	6.26274	18:15	0:15	Day 4	Voltage Interrupted	Session 16
3	-	57.7	64.1	6.26274	13:35		Day 5		Session 17
3	-	57.7	64.1	6.26274	13:50	0:15	Day 5		Session 18

The magnitude difference NoDi* plots in Figure 5.40b, Figure 5.41b, Figure 5.41e, Figure 5.42b, Figure 5.43b, Figure 5.44b, and Figure 5.45b were scaled to 50 pC. Meanwhile, the time difference NoDi* plots in Figure 5.40c, Figure 5.40f, Figure 5.41c, Figure 5.41f, and Figure 5.42c were uniformly scaled to 0.06 ms. The time difference NoDi* plots in Figure 5.43c, Figure 5.44c, and Figure 5.45c were instead scaled to 1 ms.

Voltage interruption at 1 Bar absolute

The GIS test cell was pressurized to 1 Bar absolute and the voltage raised to 35 kV. As observed in the initial round of preliminary testing, UHF activity was detected after the voltage ramp-up, as illustrated in Figure 5.40d. The UHF NoDi* pattern in Figure 5.40e reveals an intriguing ongoing trend, where the UHF data increasingly resembles the firefly-like motion of a free metallic particle. Meanwhile, the MPD NoDi* pattern in Figure 5.40b exhibits the familiar standing motion, albeit with the characteristic concentration boundaries more seamlessly blended.

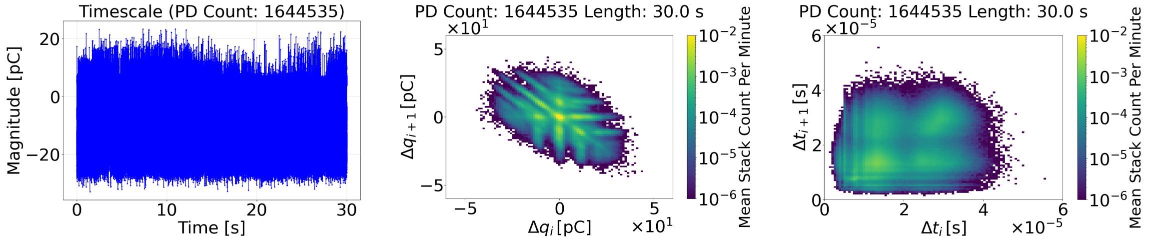

(a) MPD measurement over entire period **(b)** MPD magnitude difference NoDi* plot [a] **(c)** MPD time difference NoDi* plot [a]

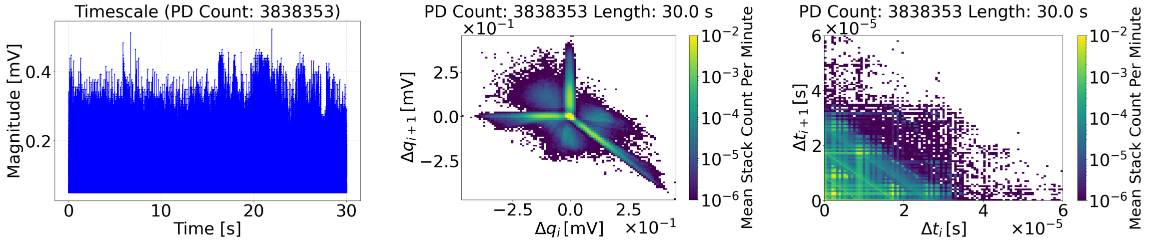

(d) UHF measurement over entire period **(e)** UHF magnitude difference NoDi* plot [d] **(f)** UHF time difference NoDi* plot [d]

Figure 5.40: Plots of the preliminary protrusion defect test run regarding voltage interruption at 35 kV and 1 Bar absolute - Session 3

The voltage was interrupted for one day and resumed the following day. Upon resuming the voltage, the UHF activity dissipated, and the characteristic standing motion pattern reappeared in the magnitude difference NoDi* plot, as shown in Figure 5.41b. This pattern confirms the correct voltage polarity. Furthermore, as illustrated in Figure 5.41e, extending the PD measurement duration does not necessarily enhance the definition of the pattern.

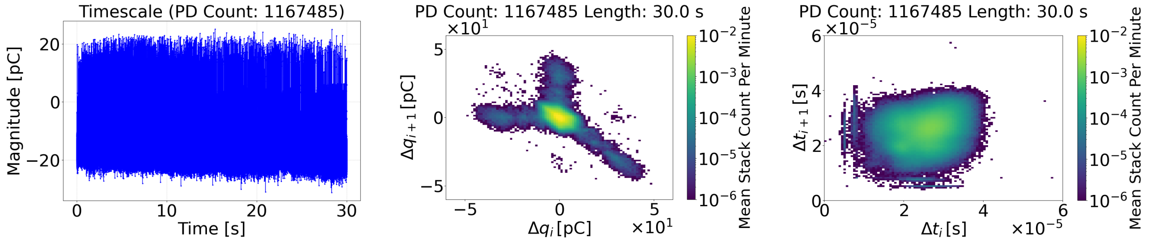

(a) MPD measurement of 30 s period **(b)** MPD magnitude difference NoDi* plot [a] **(c)** MPD time difference NoDi* plot [a]

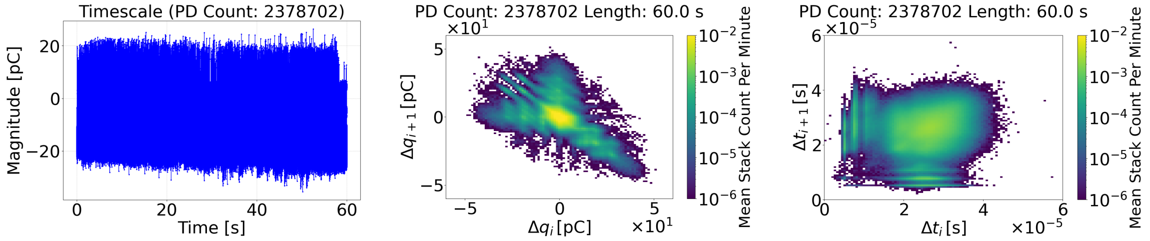

(d) MPD measurement of 60 s period **(e)** MPD magnitude difference NoDi* plot [d] **(f)** MPD time difference NoDi* plot [d]

Figure 5.41: Plots of the preliminary protrusion defect test run regarding voltage interruption at 35 kV and 1 Bar absolute - Session 4 (30 s segment [a], [b], and [c], and 60 s segment [d], [e], and [f])

The continuation of the voltage application shows the NoDi* pattern, as shown in Figure 5.42b, return to a similar shape and form as the one before the voltage interruption in Figure 5.40b, albeit with slightly larger magnitude values as noticed in Figure 5.42a. The time difference NoDi* plot in Figure 5.42c shows a larger dispersal than the one in Figure 5.40c to match the larger magnitude values.

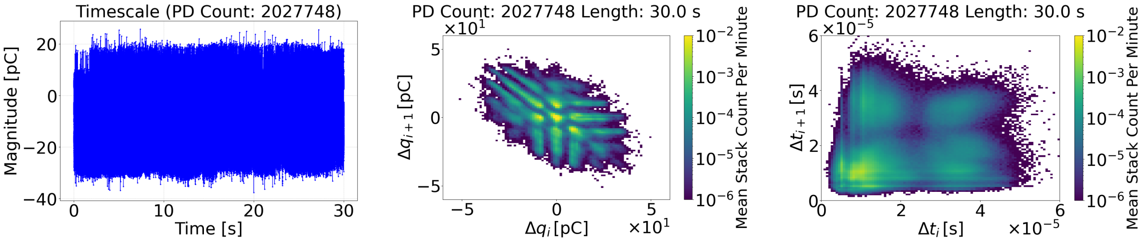

(a) MPD measurement over entire period **(b)** MPD magnitude difference NoDi* plot **(c)** MPD time difference NoDi* plot

Figure 5.42: Plots of the preliminary protrusion defect test run regarding voltage interruption at 35 kV and 1 Bar absolute - Session 5

The voltage interruption at 1 Bar absolute revealed that, despite maintaining the same polarity, a settling period occurs after the interruption. This behavior is attributed to the AC-like conditions present before the system gradually stabilizes and returns to previously observed values. Similarly, the initial PD measurement following the voltage interruption exhibited the familiar standing motion pattern, while later measurements revealed a progression toward a singular, unified concentration. This suggests that the space charge equilibrium gradually results in a more homogenized PD activity.

Voltage Interruption from 1 Bar to 3 Bar absolute

Another source of intrigue was the voltage interruption incorporating a pressure difference. The previous voltage application was raised to 40 kV and continued for 90 minutes before the PD measurement in Figure 5.43 was taken. The general shape of the magnitude difference NoDi* plot in Figure 5.43b remains relatively similar to the previous pattern in Figure 5.42b, albeit with slightly larger PD apparent charge magnitude values.

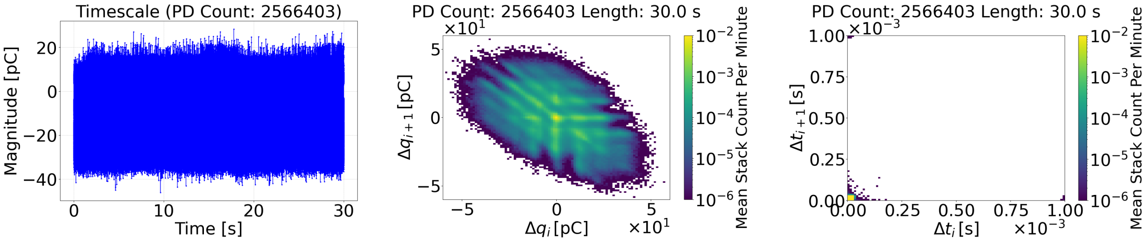

(a) MPD measurement over entire period **(b)** MPD magnitude difference NoDi* plot **(c)** MPD time difference NoDi* plot

Figure 5.43: Plots of the preliminary protrusion defect test run regarding voltage interruption at 40 kV and 1 Bar absolute - Session 7

After reducing the voltage to zero, the pressure inside the GIS test cell was increased to 3 Bar absolute before ramping the voltage up to 55 kV. The voltage increase to 55 kV was done to achieve a consistent margin between the PDIV and the voltage applied, given the pressure difference. The immediate result was a reduction in the PD apparent charge magnitude, as shown in Figure 5.44a, aligning with the findings of A. Piker et al. [12]. The wide dispersion of PD pulses suggests that the space charge regions had not yet reached equilibrium. Despite the lower PD apparent charge magnitudes, the standing motion pattern appeared more clearly defined compared to measurements taken at lower pressures.

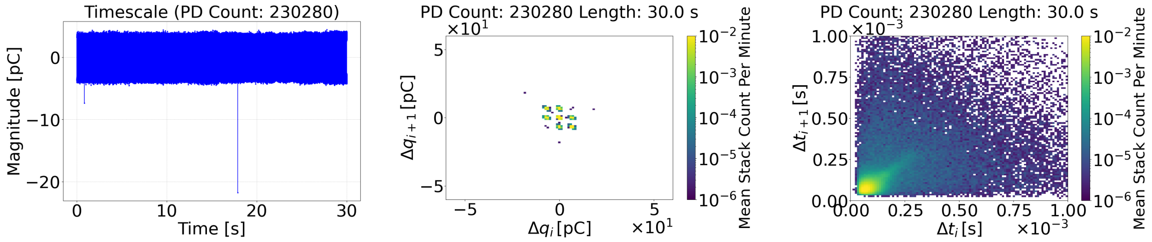

(a) MPD measurement over entire period **(b)** MPD magnitude difference NoDi* plot **(c)** MPD time difference NoDi* plot

Figure 5.44: Plots of the preliminary protrusion defect test run regarding voltage interruption at 55 kV and 3 Bar absolute - Session 8

Voltage increase to 60 kV provides a more filled-in NoDi* pattern in Figure 5.45b and a higher repetition rate, necessary for sustaining continuous PD activity throughout the long-term experiment. The time difference NoDi* plot in Figure 5.45c shows a better distribution of the space charge regions, owing to the lower dispersion of PD pulses compared to the previous one in Figure 5.44c.

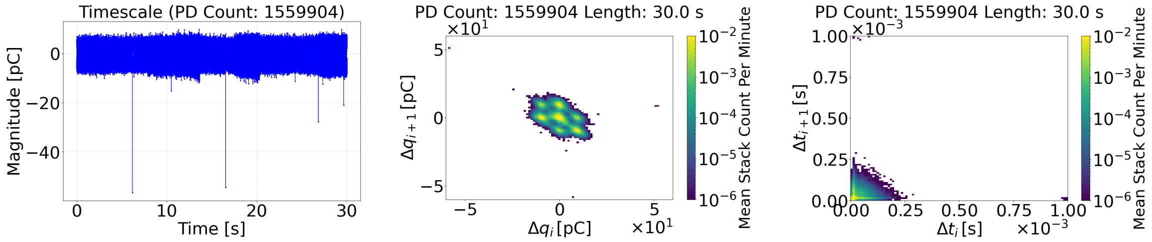

(a) MPD measurement over entire period **(b)** MPD magnitude difference NoDi* plot **(c)** MPD time difference NoDi* plot

Figure 5.45: Plots of the preliminary protrusion defect test run regarding voltage interruption at 60 kV and 3 Bar absolute - Session 11

The preliminary test runs offered valuable insights into the expected PD apparent charge magnitude values and the time required for space charge regions to stabilize. Furthermore, the trials highlighted the importance of maintaining high PDIV ratios to ensure continuous PD activity, evident in the preliminary test phase regarding overnight voltage application, where the number of PD pulses dropped by nearly 70%.

5.3.3. Long-Term Test Run

The long-term experiment on the protrusion defect concluded the empirical phase of this study. The preliminary overnight voltage application test provided an early indication that the investigation was on the right track as a noticeable increase in PD apparent charge magnitude was observed. Similarly, the tested height of 4 mm was adequate for generating significant PD activity, while securing the metallic particle with electrical tape did not interfere with defect classification. The protrusion defect successfully produced the expected standing motion pattern.

To assess the degree of tip radius erosion and the progressive evolution of PD behavior over an extended period, the protrusion defect shown in Figure 5.46a was subjected to 65 kV for one week. The defect was carefully bent to achieve a height of exactly 4 mm, with the test setup further illustrated in Figure 5.46b. After the experiment, a ruler measurement revealed that the protrusion was not perfectly centered, which likely contributed to the lower PD apparent charge magnitudes compared to the preliminary test runs.

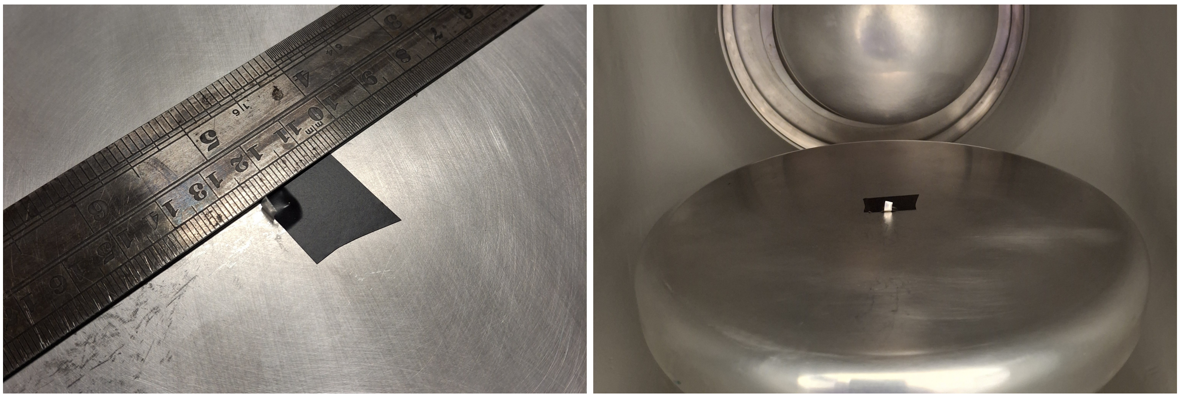

(a) Protrusion defect on the ground electrode with a ruler

(b) Protrusion defect inside GIS test cell

Figure 5.46: Pictures of the protrusion defect of the long-term experiment

The magnitude difference NoDi* plots in Figure 5.47b, Figure 5.48b, Figure 5.49b, Figure 5.49e, Figure 5.50b, Figure 5.50e, and Figure 5.51b are scaled to 20 pC. Meanwhile, the time difference NoDi* plots in Figure 5.47c, Figure 5.48c, Figure 5.49c, Figure 5.49f, Figure 5.50c, Figure 5.50f, and Figure 5.51c are uniformly scaled to 0.04 ms. No UHF activity was detected throughout the long-term experiment.

Day One

The first day produced the characteristic standing motion pattern with the correct polarity as shown in Figure 5.47b. Only one PD measurement was taken as the experiment started in the late afternoon.

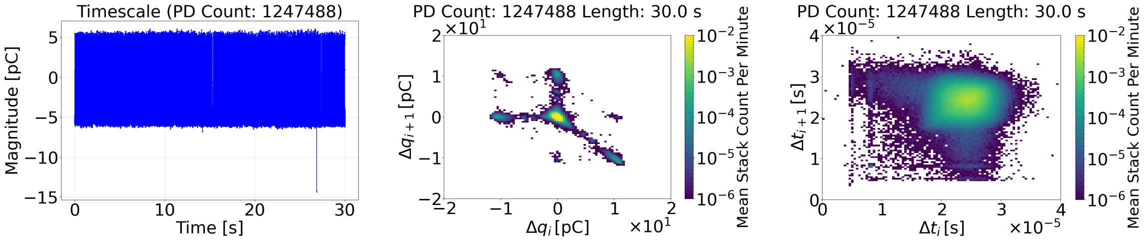

(a) MPD measurement over entire period

(b) MPD magnitude difference NoDi* plot

(c) MPD time difference NoDi* plot

Figure 5.47: Plots of the long-term protrusion defect experiment at 65 kV and 3 Bar absolute - day one (afternoon) measurement

Day Two

An anomaly occurred on the second day when the morning PD measurement showed no PD activity. The initial assumption was that the protrusion defect had detached itself from the electrical tape. Thorough troubleshooting discovered no visible discrepancies in the system. The only notable change was an ongoing 300 kV breakdown experiment in the adjacent lab room.

After discussing the issue with a colleague in the afternoon, it was discovered that the neighboring experiment was interfering with the gain amplifier of the measurement equipment. Out of the box, the Omicron software is set to automatic gain adjustment. Switching the gain to a fixed manual value resolved the issue, though the results remained suboptimal due to the low count and large dispersion of PD pulses, as shown in Figure 5.48. Nevertheless, the characteristic standing motion pattern is still discernible in Figure 5.48b.

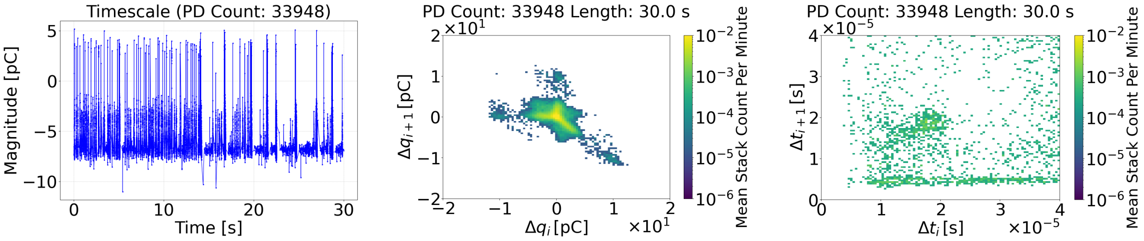

(a) MPD measurement over entire period **(b)** MPD magnitude difference NoDi* plot **(c)** MPD time difference NoDi* plot

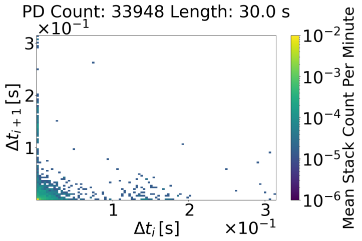

(d) Wide view of time difference plot [c]

Figure 5.48: Plots of the long-term protrusion defect experiment at 65 kV and 3 Bar absolute - day two (afternoon) measurement

Day Three

On the third day, the PD activity returned to a more expected behavior. Intermittent 300 kV experiments still occurred throughout the morning, resulting in the occasional PD pulse in the range of 60 to 80 pC, as shown in Figure 5.49a. Despite this, the following observations were made. The characteristic standing motion pattern observed on the first two days gradually transitioned into a more blended pattern, where the distinctive diagonals began to merge, as observed in the preliminary test phase. Additionally, the time-scale plot of the afternoon measurement in Figure 5.49d, free from external interference, reveals emerging peaks rising above the residual PD activity.

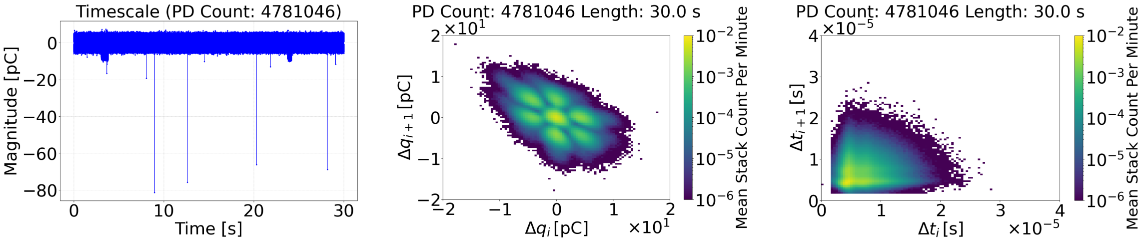

(a) MPD measurement over entire period **(b)** MPD magnitude difference NoDi* plot [a] **(c)** MPD time difference NoDi* plot [a]

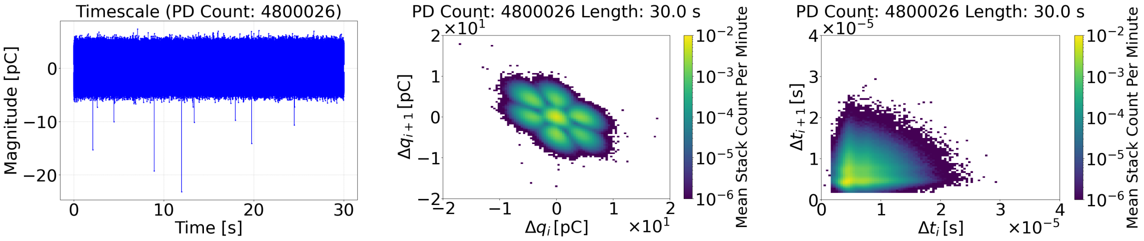

(d) MPD measurement over entire period **(e)** MPD magnitude difference NoDi* plot [d] **(f)** MPD time difference NoDi* plot [d]

Figure 5.49: Plots of the long-term protrusion defect experiment at 65 kV and 3 Bar absolute - day three (morning [a], [b], and [c], and afternoon [d], [e], and [f]) measurement

Day Four

On the fourth day, the PD behavior observed during day three persisted, with additional external experimental interference occurring in the morning. The magnitude difference NoDi* plots in Figure 5.50b and Figure 5.50e continue to exhibit the morphed standing motion pattern seen the previous day. Similarly, the time difference NoDi* plots in Figure 5.50c and Figure 5.50f closely resemble those from the prior measurements, further reinforcing the trend of rapid change in the beginning and a more gradual pattern evolution in the days after. As with the long-term free metallic particle defect experiment, the fourth day of PD measurements occurred on a Friday, with data collection resuming the following Monday.

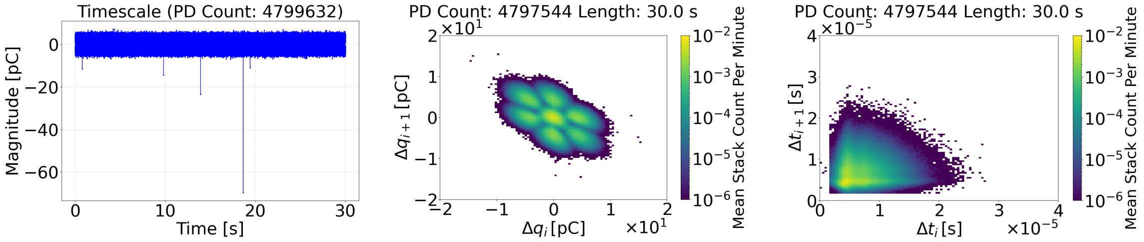

(a) MPD measurement over entire period **(b)** MPD magnitude difference NoDi* plot [a] **(c)** MPD time difference NoDi* plot [a]

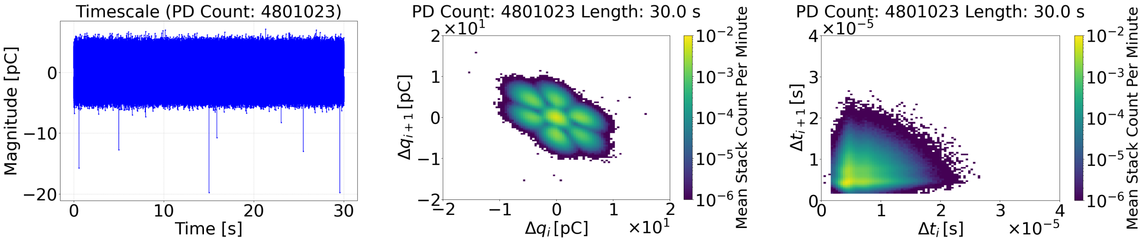

(d) MPD measurement over entire period **(e)** MPD magnitude difference NoDi* plot [d] **(f)** MPD time difference NoDi* plot [d]

Figure 5.50: Plots of the long-term protrusion defect experiment at 65 kV and 3 Bar absolute - day four (morning [a], [b], and [c], and afternoon [d], [e], and [f]) measurement

Day Seven

The final PD measurement in Figure 5.51 shows minimal deviation from the previous measurement on day four, despite continuous voltage application over the weekend. The magnitude difference NoDi* plot in Figure 5.51b maintains the morphed standing motion pattern, while the time difference NoDi* plot in Figure 5.51c remains largely unchanged. This suggests that the most significant changes in PD behavior occurred in the initial days, with little to no further evolution over the extended test period.

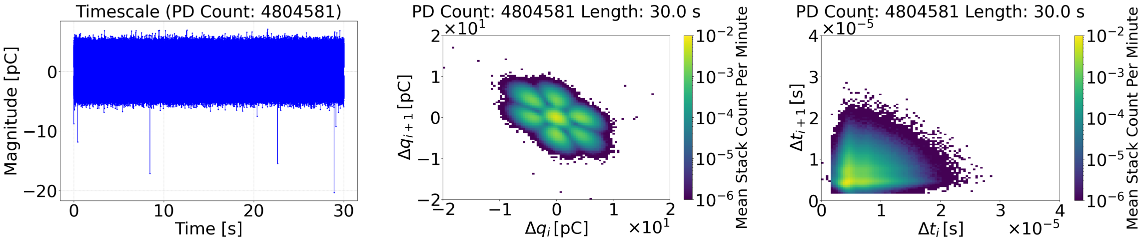

(a) MPD measurement over entire period **(b)** MPD magnitude difference NoDi* plot **(c)** MPD time difference NoDi* plot

Figure 5.51: Plots of the long-term protrusion defect experiment at 65 kV and 3 Bar absolute - day seven

As expected, the long-term experiment with the protrusion defect closely aligned with the findings of the long-term study conducted by T. Vu-Cong et al. [10]. Most notable changes in the magnitude difference NoDi* plots occurred within the initial days, specifically within the first two days in this case. The preliminary overnight voltage application test run even suggests that significant changes may occur within a single day. However, the hypothesis remains unverified due to the lack of follow-up testing. A more detailed discussion of the long-term experiment results can be found in Chapter 6. The next section focuses on a microscopic examination of the protrusion defect.

5.3.4. Protrusion Erosion

The tip erosion observed in the protrusion defect exhibited significantly greater progression than any of the particles in the free metallic particle defect. Before the long-term experiment, the protrusion defect displayed a multi-faceted tip, as captured under 100x magnification in Figure 5.52. As shown in Figure 5.52a, the overall tip thickness ranged from 240 to 250 μm along its length. A distinct outcrop protruding from the main tip, with a smaller width varying between 30 and 70 μm, is visible in Figure 5.52b.

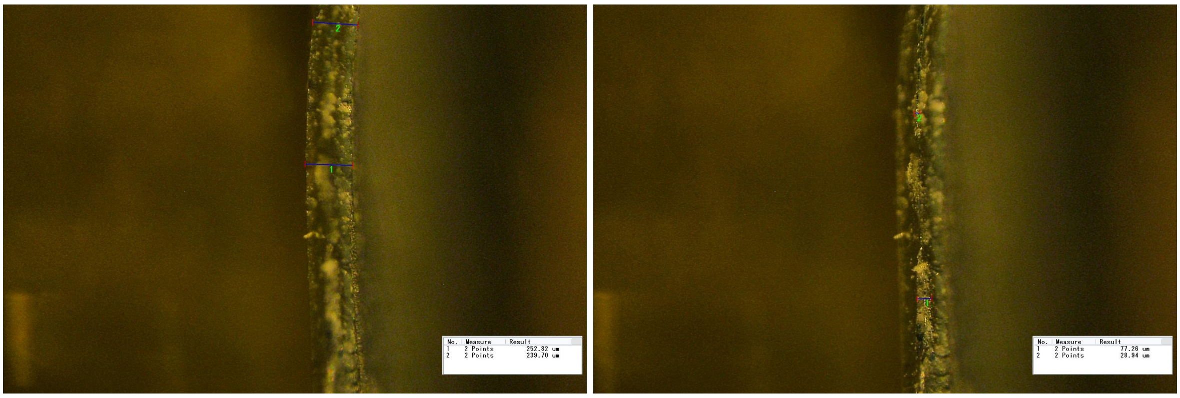

```
No.  Measure      Result
1    2 Points          252.82 um
2    2 Points          239.70 um
```

```
No.  Measure      Result
1    2 Points           77.26 um
2    2 Points           28.94 um
```

(a) 100x magnification of overall thickness **(b)** 100x magnification of outcrop protruding from tip

Figure 5.52: Microscope imaging of particle tip before the long-term protrusion defect experiment

Following the long-term experiment, the protrusion defect was reexamined under the microscope at 100x and 200x magnification, as shown in Figure 5.53. The 100x magnification image in Figure 5.53a reveals that the previously observed outcrop at the particle tip has eroded entirely. Further examination of the particle edge confirms the same trend. This tip erosion directly correlates with the observed changes in PD behavior, reinforcing the relationship between physical degradation and PD behavior over time, as noted by the long-term study by T. Vu-Cong et al. [10].

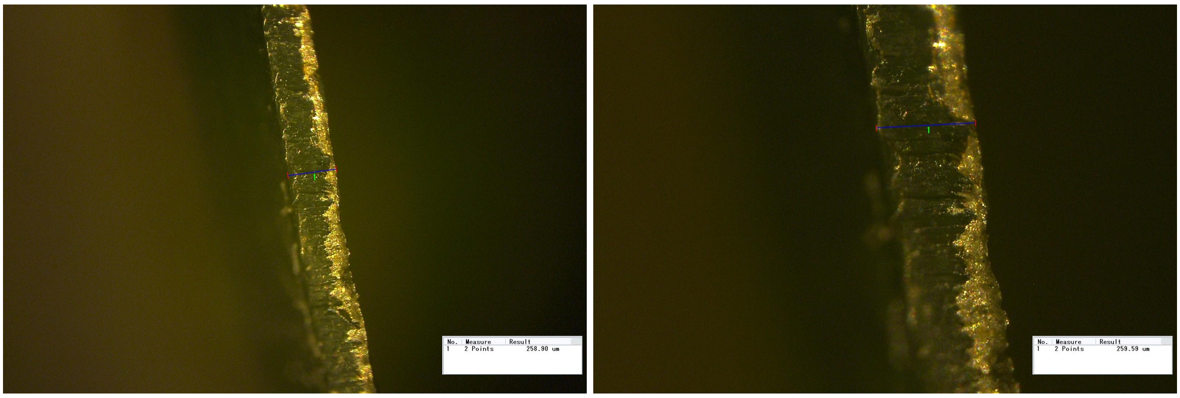

```
No.  Measure      Result
1    2 Points          258.90 um
```

```
No.  Measure      Result
1    2 Points          259.59 um
```

(a) 100x magnification of overall thickness **(b)** 200x magnification of overall thickness

Figure 5.53: Microscope imaging of particle tip after the long-term protrusion defect experiment

Unfortunately, weight measurements were an afterthought, as the metallic particle was not initially weighed. Instead, the focus had been on improving the management of microscopic imaging. Better coordination and the capture of multiple images along the entire particle length allowed for a more detailed comparison and analysis of tip erosion. The next chapter presents the results from both the free metallic particle and the protrusion defects.

6

Discussion

This chapter discusses the results from both the preliminary and long-term experiments on the free metallic particle and protrusion defects. Each section provides insights and key considerations from various test setups and parameters. Following this, common factors influencing both defect types are discussed. The chapter concludes with reflections on the overall test setup, analysis methods, and planning considerations.

While the discussion in this chapter is not meant to be all-encompassing, it strives to convey the thought process encountered along the way and address the main objectives stated in Chapter 1.

6.1. Free Metallic Particle Defect

The free metallic particle defect provided new insights into the long-term study of PD activity in defects, expanding upon previous research. As the long-term study by T. Vu-Cong et al. [10] solely addressed protrusion defects, this work heavily relied on the findings of the works presented in the literature review in Chapter 3. The NoDi* plots from the works [24], [41] provided characteristic patterns that validated the particle behavior observed in the preliminary and long-term experiments. Additionally, the study by P. Wenger et al. [46] was instrumental in explaining the various firefly motions detected. These prior works allowed the focus to remain on analyzing the long-term changes in PD behavior rather than on verifying the observed particle motion patterns.

Given the extensive results presented in the previous chapter, the discussion begins by analyzing the preliminary test trials to identify common trends with the long-term experiment and reiterate the decision to proceed with the third test setup, featuring the stacked hoop and ring configuration as the primary setup. The key findings are summarized in the concluding paragraph of the long-term experiment section.

6.1.1. Preliminary Test Phase

The preliminary test runs involved multiple test configurations, including setups with the stainless steel lid, the copper hoop, and a combination of both. Despite the relatively short voltage application periods, the NoDi* patterns and physical observations derived invaluable insights, even though certain aspects like microscope imaging were reserved for the long-term experiment.

Particle containment remained a persistent challenge, as collisions with the HV conductor often ejected particles from the electrode configuration. Early design concepts explored using glass or acrylic domes to enclose the space between the electrodes. However, both materials are prone to space charge accumulation, generating static forces that attract particles rather than acting as effective insulators. The work by G. C. Stone et al. [36] provided a foundation with its stainless steel lid setup. However, their electrode configuration and test environment greatly enhanced particle retention. This work modified the previously mentioned setup by incorporating a copper hoop to improve particle containment, specifically when several particles were used simultaneously.

Particle containment was only one aspect of the challenge. Preliminary testing revealed that a single particle was insufficient to ensure continuous motion, prompting the introduction of multiple particles into the test environment. Including several particles in the electrode configuration ensured periodic particle motion but uncovered a significant issue. Notably, the PD activity associated with the firefly motion of one particle often overshadowed the PD signals from other particles, raising concerns that both algorithmic detection methods and human experts might misinterpret the data, incorrectly identifying a single particle rather than the actual number present.

These solutions generated multiple NoDi* patterns, establishing a baseline for the long-term experiment. Most importantly, these patterns aligned with those observed for the firefly and the standing motion in previous studies in Figure 3.6. The following sub-sections present additional minor observations gathered during each test run in the preliminary phase.

First Setup with Stainless Steel Lid

The first setup featured Particle 1 (4 mm) placed on a stainless steel lid, as shown in Figure 5.2a. The particle achieved lift-off at 52 kV, demonstrating that its length was suitable for the protrusion defect experiments. As mentioned later in Section 6.2, the protrusion defect managed to reproduce the standing motion of a free metallic particle and offered a comparison baseline. Likewise, the PDIV of 45 kV and the lift-off voltage of 52 kV ensured a sufficient margin to the maximum operating voltage of 65 kV, inferring that particles with longer lengths within reason could achieve lift-off.

This setup also underscored the importance of UHF measurements in particle detection and noise rejection, as they confirmed that the detected PD activity originated from the free metallic particle rather than from any external source. The UHF measurement captured and reproduced the standing motion pattern of the particle at the HV conductor in the NoDi* plot in Figure 5.4i. At higher voltages, the NoDi* plots in Figure 5.5a at 53 kV and Figure 5.6a at 60 kV indicated continued PD activity, albeit at much lower magnitudes. The lack of UHF activity suggested that the particle had been ejected from the electrode configuration and that the PD activity originated from the stainless steel lid.

The NoDi* pattern observed in Figure 5.4c matched the firefly motion of wire and spiral particles as described in the work [39], confirming both the correct detection of particle motion and the known overlap in NoDi* patterns between different particle types, as noted in the same work. However, while the same polarity was applied, the orientation of the NoDi* pattern is mirrored. Likewise, the timescale plot in Figure 5.4b matches the firefly motion with large jumping amplitudes observed by the work [46]. As the voltage polarity was negative, the firefly motion occurred at the HV conductor, which explains the ejection of the particle from the electrode configuration.

The stainless steel lid is not without its faults, as illustrated by the presence of considerable PD activity at -53 kV in Figure 5.5b and at -60 kV in Figure 5.6b. Additional steps should be taken to treat the edges to minimize the PD activity generated. Likewise, the considerable levels of PD activity further reveal discrepancies in the initial PD-free check that certified the test setup. Further retesting should be done by analyzing the data with the help of the PSA plotter rather than exclusively through visual inspection of the incoming data stream.

Most importantly, this test setup highlighted a critical limitation: the stainless steel lid failed to contain the particle, allowing it to escape the electrode configuration. This necessitated a redesign of the containment approach, leading to the implementation of the copper hoop in the following preliminary test setup.

Second Setup with Copper Hoop

The second setup, consisting of only the copper hoop, aimed to remedy the shortcomings of the stainless steel lid. Particle liftoff was achieved at -43 kV, as observed in Figure 5.8. Compared to the previous setup, the lower liftoff voltage was primarily attributed to the difference in pressure, as the test particle remained unchanged. Since the particle lifted off during voltage ramp-up, the associated PD activity, identifiable by the largest PD apparent charge magnitude values detected in all test runs, was compounded by the initiation of other discharges within the system due to the AC-like conditions. As an unintended consequence, the large peaks observed in the MPD measurement generated a more defined NoDi* pattern in Figure 5.8d with its very prominent diagonals, which unmistakably indicate firefly motion. The time difference NoDi* plot in Figure 5.8e matches that of the first setup in Figure 5.4f, albeit with a factor-of-ten difference. Furthermore, a detailed analysis of the time scale plot in Figure 5.8b supports the firefly motion conclusion and classifies it as one with large jumping amplitudes.

The substantial magnitude values recorded by the MPD instrument are not reflected in the UHF measurements in Figure 5.8c. The nearly fivefold reduction in the UHF values when compared to those in the first setup in Figure 5.4g can be attributed to the shielding effect of the copper hoop as the standing waves of the EM signal inherently interact with the hoop. This effect is further reflected in the ability of the UHF to correctly assess the corresponding particle motion. The near-absence of data points in the signal does not facilitate the creation of a NoDi* pattern sufficient for defect classification, as illustrated in Figure 5.8f.

In retrospect, the second setup with the copper hoop was a success in some regards. The MPD instrument detected the correct polarity in the magnitude difference NoDi* plot in Figure 5.8d compared to the first setup in Figure 5.4c. Likewise, the free metallic particle was contained within the electrode configuration. However, the final resting place of the particle was less than ideal as it landed in a dead zone, as indicated by the absence of PD activity. Additionally, the setup achieved better ambient noise level suppression, aligning with the values measured in the PD-free check in Table 5.2, outperforming the first setup. The idea of stacking the copper hoop on the stainless steel lid was developed to guide the particle back to a more favorable location within the electrode configuration after motion. This modification is presented in the next section.

Third setup with Stacked Copper Hoop and Stainless Steel Lid

The third setup played a decisive role in preparing for the long-term experiment. The combination of the copper hoop and stainless steel lid improved noise suppression while ensuring that particles remained within the high-electric-field regions of the electrode configuration. During the voltage ramp-up, the noise level was notably low, with only five to ten pulses of 1–2 pC detected within a thirty-second MPD measurement, attributed to the presence of the particles. Upon exceeding the PDIV, the particles generated significant PD activity and exhibited firefly motion, with the most explicit example observed in the single-particle case, as shown in Figure 5.10b. However, the UHF measurement continued to be affected by the damping effect of the copper hoop on the EM waves, further reflected in the low number of PD pulses detected.

The two test trials, one with Particle 1 (4 mm) and the other with all ten particles, demonstrated the reproducibility of particle liftoff and firefly motion. The single-particle trial revealed that neither increasing the voltage nor reversing the voltage polarity could reset the particle to initiate PD activity once it had landed in a dead zone. The ten-particle trial mitigated this issue while also generating sufficient PD activity at the HV conductor for the UHF measurement to produce a characteristic NoDi* pattern, as illustrated in Figure 5.13e.

The UHF measurement in Figure 5.13e enabled proper particle motion recognition, capturing both the standing and firefly motion patterns observed in previous studies [12], [24]. While the MPD measurement aligned with the expected NoDi* pattern for firefly motion, the corresponding standing motion pattern was not immediately evident. To investigate further, a detailed analysis was performed to isolate the distinct stages of particle motion. A sixty-second MPD measurement was divided into two segments, as shown in Figure 5.14 and Figure 5.15. The latter thirty-second segment was further examined over a shorter time interval in Figure 5.16 to isolate a collection of peaks. This analysis revealed that the firefly motion referenced in previous studies is, in fact, unintentionally grouped with other motion patterns.

Existing studies often document the entire cycle of particle motion from the ground electrode to the HV conductor but overlook the fact that the firefly motion consists of two distinct groups of PD activity. The first group corresponds to the PD activity when the particle remains on the ground electrode, characterized by the unified concentration of pulses in the center of the NoDi* pattern, similar to that of the standing motion. By isolating the PD activity around the peaks, as shown in the detailed view in Figure 5.16d, the second group can be identified by the distinct diagonals and directly linked to the movement of the particle away from the ground electrode and its subsequent interaction with the HV conductor. This highlights how the more intense PD activity associated with firefly motion dominates, effectively overshadowing the background standing motion pattern in longer measurement intervals.

Testing multiple particles in the electrode configuration introduced additional challenges. Without visual recording devices, it was impossible to determine which particle was responsible for a given firefly motion. As reported, particles over 6 mm in length tend to exhibit more stable firefly motion and move along the electrode [31]. This suggests that the extended firefly motion duration in the single-particle test in Figure 5.10a corresponded to a larger particle, whereas the shorter duration in the following test run with ten particles in Figure 5.16 indicated a smaller one. P. Wenger et al. further clarified that a particle's charge-to-mass ratio increases with length, which provides a better explanation for these observations. Thus, the significantly larger PD apparent charge magnitude in the ten-particle test trial indicates the interaction of a particle larger than the initial 4 mm one used in the single-particle trial. The ejection of Particles 3 and 4 (5 mm) further coincides with this conclusion.

Ultimately, the test trials emphasized that particle length and positioning within the electrode configuration were the primary factors influencing PD apparent charge magnitude, contrary to the protrusion defect, where tip radius plays a dominant role. Consequently, for the long-term experiment, the voltage was increased from 50 kV to 60 kV to provide additional electrical stress and prolong particle motion, as particles tended to accumulate in certain regions due to the formation and distribution of space charge regions.

In conclusion, the third setup proved to be a highly effective platform for the long-term experiment, allowing for the analysis of various particle motions, from firefly to hovering. Furthermore, since all particles moved from their original placements, the test conditions did not limit particle behavior.

6.1.2. Long-Term Test Run

The previous test runs culminated in the long-term experiment. The preliminary tests established expectations for particle motion and PD apparent charge magnitude values while also addressing key challenges such as voltage level selection, particle containment, and particle selection. However, some issues, such as particle liftoff during voltage ramp-up, persisted in the long-term experiment. This effect was mitigated by the periodic liftoff observed in the days following the initial voltage application, during which conditions increasingly resembled a homogeneous DC environment.

Due to the more stable DC conditions, the MPD and UHF measurements on the second and third days yielded a more representative NoDi* pattern for firefly motion. The NoDi* patterns from the study [24] provided a strong foundation for particle motion classification despite the difference in gas used, i.e., SF_6. The comparison reveals key differences, such as the more elongated diagonals observed in the patterns of this work, as illustrated in Figure 5.22d and Figure 5.23d. These differences can be attributed to variations in test conditions independent of the gas used. Notably, A. Pirker et al. examined wire and spiral particles, whereas this study utilized lamella-shaped particles, which likely contributed to the observed pattern distinctions.

While pattern analysis played a key role in characterizing firefly motion, examining the time-scale domain provided deeper insights into the interactions between different particles in the test setup. Further analysis of the firefly motion within the time-scale domain enabled differentiation between particle lengths, as noted by P. Wenger et al. [31] and observed in the preliminary test runs. Notably, measurements from the first three days revealed three distinct sets of firefly motion, each exhibiting similar magnitudes but varying durations, suggesting the presence of multiple particles. However, visual confirmation is required to draw definitive conclusions.

Additionally, the MPD measurements captured patterns for other particle motions, such as hovering and standing, confirming their similarities and partial overlap with the firefly motion observed in the preliminary phase. The similarities between the standing and hovering motion patterns, as observed in Figure 5.25b and Figure 5.26b, necessitate a more detailed analysis of the time-scale plot for clear differentiation, which may not always be available. On the other hand, the firefly motion tends to dominate and overshadow the previous two motions in the NoDi* plot due to its distinct diagonals and significantly larger PD apparent charge magnitude values. This can lead to information loss and potential misidentification of the actual number of particles present in the test setup.

While visual recording devices would have aided in identifying the specific particles involved, the primary focus of this work was the evolution of PD behavior over time and whether physical changes to the particles were responsible for any observed variations. The long-term study by T. Vu-Cong et al. [10]

reported a fivefold increase in PD apparent charge magnitude and a twofold decrease in repetition rate in the SF_6 alternative gas, C_5FK–dry air, as shown in Figure 3.3. This was attributed to changes in the tip radius caused by electrochemical etching due to decomposition byproducts, though in the context of a protrusion defect.

In this study, the free metallic particles were subjected to a continuous 60 kV voltage over a week to initiate repeated PD activity and assess any physical changes at the end. As illustrated in Figure 6.1, the PD apparent charge magnitude varied considerably on the first three days due to measurements including the firefly motion. The maximum values in each MPD measurement were taken as the reference point, as averages did not accurately represent the change in PD behavior. Omitting the measurement values affected by the firefly motion, the overall change in PD apparent charge magnitude saw an increase from 35 pC on the first day to 44 pC on the fourth day, amounting to a 20% increase and far from the fivefold increase reported in the long-term study by T. Vu-Cong et al. [10]. The PD measurements from the seventh day were not included, given that only Particle 10 (10 mm) remained in the electrode configuration. Additionally, the repetition rate appeared to stabilize over time, likely due to the increasingly steady DC conditions, and did not exhibit the same level of steep decline as reported by T. Vu-Cong et al.

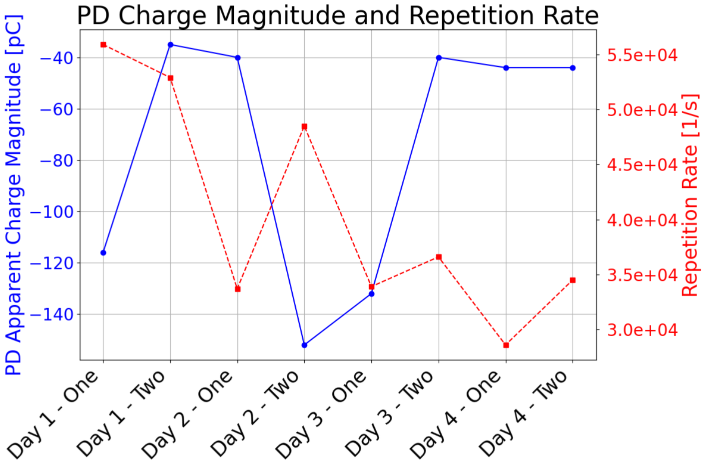

Figure 6.1: Maximum value of PD apparent charge magnitude and repetition rate of free metallic particle defect of the long-term experiment over four day period based on MPD measurement

Physical examination under a microscope, as shown in Figure 5.28, further supported the minimal increase in PD apparent charge magnitude by revealing only slight surface roughness without significant structural changes to the particle. This finding reinforces the hypothesis that free metallic particle defects behave fundamentally differently from protrusion defects. The work by P. Wenger et al. [46] further supports this distinction, highlighting that free metallic particles exhibit diverse motion patterns, including complete rotations about all axes of symmetry, as they move toward the HV conductor. Consequently, electric charge does not accumulate consistently on any single part of the particle due to charging effects from space charge regions, resulting in lower localized electric field concentrations compared to protrusion defects. Additionally, weight measurements from the long-term experiment further validate this perspective, as all particles exhibited measurable weight loss, suggesting that a physical change to the particles did occur.

In this study, the absence of physical particle changes in the range reported by other works can largely be attributed to the relatively moderate voltage levels used. In contrast, the particles tested by P. Wenger et al. [31] were exposed to voltages between 240 kV and 550 kV for 15 to 20 minutes, leading to significantly higher erosion levels, albeit with SF_6 as the insulating gas. However, the intended objective of this study was successfully achieved, as measurable changes in PD behavior were observed, eliminating the need for the higher voltage levels applied in existing works.

Furthermore, despite efforts to contain the particles, most eventually escaped the particle containment system. Positive polarity had been applied to the HV conductor to mitigate this, aiming to initiate and restrict firefly motion to the ground electrode, where the particles would have a higher chance of remaining in the high electric field regions. However, the UHF equipment detected the standing motion on the HV conductor, indicating that this restriction did not occur. Nonetheless, Particle 10 (10 mm) remained inside the electrode configuration and generated enough PD activity for the correct NoDi* pattern, as shown in Figure 5.27e, despite its off-center location.

In summary, the objective of analyzing the progressive, long-term evolution of PD behavior in the case of free metallic particle defects was successfully achieved. A 20% increase in PD apparent charge magnitude, accompanied by a corresponding decrease in repetition rate, was observed. Additionally, the evolving NoDi* patterns over multiple days demonstrated their dynamic nature, influenced by a combination of different particle motions, orientations, and space charge region distributions. However, pinpointing the exact time interval in which the most significant change in PD activity occurred remained challenging. While the existing long-term study by T. Vu-Cong et al. [10] focused solely on protrusion defects, this study provides a valuable dataset on an alternative defect type, which can be utilized in future research to enhance defect identification. Notably, the observed changes in PD behavior could be attributed to erosion caused by electrochemical etching from decomposition byproducts based on weight measurements rather than microscopic examination.

The next section will focus on the protrusion defect and its corresponding changes in PD behavior.

6.2. Protrusion Defect

The protrusion defect was the second defect type examined in this work, expanding on the findings from the free metallic particle defect in this work and the long-term study by T. Vu-Cong et al. [10]. The continued endeavor into the protrusion defect aimed to bridge the gap between the NoDi* patterns observed in SF_6 and the alternative gases, C_5FK–dry air and C_4FN–CO_2, and the lack of similar data in technical air in the long term. Similar to the free metallic particle defect, the protrusion defect underwent a series of preliminary test runs to identify potential challenges and improve the test setup before transitioning to long-term experiments. While the preliminary tests for the free metallic particle defect primarily addressed particle containment, the ones for the protrusion defect focused on assessing the effects of voltage interruption, pressure variations, and voltage polarity reversal.

Unlike the free metallic particle tests, which involved multiple particle lengths, the protrusion defect experiments utilized particles with a fixed height of 4 mm, ensuring a consistent baseline for comparison. This height was specifically chosen to imitate the standing motion of the 4 mm particle from the free metallic particle defect, allowing for a direct comparison of the corresponding NoDi* patterns.

The standing motion patterns obtained from the free metallic particle defect in this work, alongside those reported by K. Juhre et al. [41] in Figure 3.6a, played a crucial role in the validation process. Additionally, the long-term study by T. Vu-Cong et al. [10] served as a reference for analyzing changes in the PD apparent charge magnitude, the PD repetition rate, and the degree of erosion observed. Meanwhile, the corresponding NoDi* plots of C_5FK-dry air in Figure 3.3 provided further basis for the knowledge transfer feasibility from fluorinated gases to technical air.

The following sections detail the key findings from the preliminary test runs and the long-term experiment, highlighting the observed changes in PD behavior and erosion patterns. The long-term section addresses whether the main objectives were fulfilled for the protrusion defect.

6.2.1. Preliminary Test Phase

Before conducting the full-scale, long-term experiment, the protrusion defect underwent two rounds of preliminary testing. The first batch, involving overnight voltage application, yielded promising results. An increase in the PD apparent charge magnitude was observed after just one day of continuous voltage application, accompanied by considerable UHF activity, as shown in Figure 5.32.

This phase also addressed concerns regarding the use of negative polarity. Maintaining a sufficient margin between the PDIV and the applied voltage proved crucial to ensuring sufficient PD activity for defect classification. When comparing the session in Figure 5.33b and the one in Figure 5.35b, the number of PD pulses dropped by approximately 98% within one hour. Even increasing the voltage to the maximum value of -65 kV failed to restore PD activity to previous levels. Nonetheless, negative polarity produced a more precise standing motion pattern than positive polarity. Ultimately, a positive voltage was selected for the long-term experiment to ensure the PD repetition rate remained sufficiently high throughout the week-long period, owing to the lower PDIV over negative polarity.

Additionally, voltage reversal resulted in a significantly lower PD apparent charge magnitude due to the redistribution of space charge regions, as illustrated between Figure 5.36b and Figure 5.37b. Even after prolonged positive voltage application, the values did not return to those observed under negative polarity. This further reinforced the relation between PD activity and the applied voltage as a function of the PDIV, as reported by A. Pirker et al. [12].

The second round of preliminary testing incorporated repeated voltage interruptions and pressure variations alongside the previously tested case of voltage polarity reversal. The voltage interruption at 1 Bar absolute further reinforced the findings of the long-term study by T. Vu-Cong et al. [10], confirming that gas composition was not the primary factor driving changes in PD behavior. However, a stabilization period was observed before the NoDi* pattern returned to its prior state, likely due to the space charge regions reestablishing equilibrium. This effect is illustrated in the comparison of the three sets of NoDi* patterns in Figure 5.40b, Figure 5.41b, and Figure 5.42b. Additionally, testing at higher pressures resulted in a decrease in PD apparent charge magnitude and repetition rate, aligning with the findings of A. Pirker et al. [12].

Across both batches of preliminary test runs, the NoDi* patterns exhibited a consistent trend. Following the initial voltage application, the protrusion defect closely mirrored the standing motion previously observed in the free metallic particle defect, aligning with the PSA plots in other studies [10], [41]. However, as time progressed, the patterns evolved into a more unified structure, with individual concentrations merging rather than remaining distinct, as illustrated in Figure 5.45b. While the percentage increase in PD apparent charge magnitude does not provide a precise measure of PD behavior due to variations in test conditions, the preliminary testing phase successfully achieved a key objective of this study: demonstrating that PD behavior changes over time. These findings offer clear evidence of evolution in PD activity, reinforcing the need for the long-term experiment.

The following section presents the results of the long-term experiment.

6.2.2. Long-Term Test Run

The preliminary test runs laid the foundation for the long-term experiment, offering critical insights and NoDi* patterns for comparison. The overnight voltage application proved the most significant out of the two phases, revealing a clear increase in PD apparent charge magnitude. The long-term experiment validated these initial findings and provided further justification for the underlying mechanisms through physical examination of the tip radius.

Over seven days, as shown in Figure 6.2, the protrusion defect exhibited a 30% increase in PD apparent charge magnitude, accompanied by a 70% increase in the PD repetition rate before stabilizing. However, external interference from an adjacent experiment affected the measurements, notably influencing the repetition rate on day two and causing fluctuations in PD apparent charge magnitude on the mornings of days three and four. Therefore, the calculation for the percentage increases took only the MPD measurements on the first and last day into consideration. Likewise, to ensure accuracy and consistency with the previous evolution plot in Figure 6.1, the plot in Figure 6.2 was generated using the maximum values recorded by the MPD device for each PD measurement. Averaging the values resulted in abnormally low readings that did not accurately represent the observed trend in PD activity.

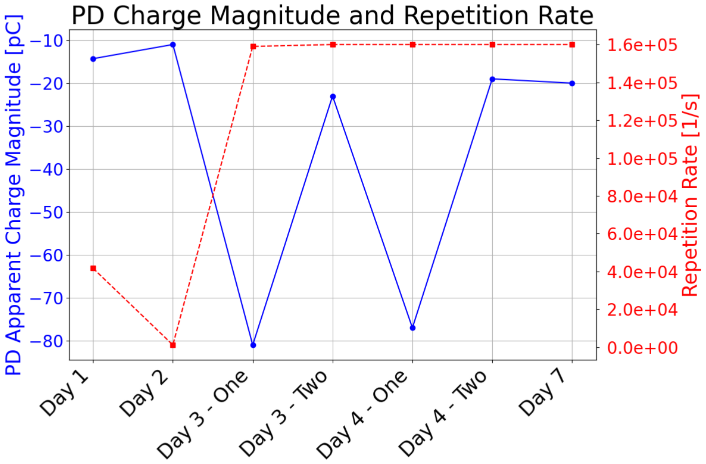

Figure 6.2: Maximum value of the PD apparent charge magnitude and repetition rate of protrusion defect of the long-term experiment over seven days based on the MPD measurements

The long-term experiment substantiates the changes in PD behavior through the observed erosion of the tip radius, as revealed in the microscope images taken before in Figure 5.52 and after in Figure 5.53. The overall increase in the tip radius is evident in the complete erosion of the outcrop extending beyond the main body of the protrusion. The physical change in the tip radius aligns with the findings of the long-term study by T. Vu-Cong et al. [10]. However, the initial tip radius in this work was larger at 30-70 μm compared to the 20-25 μm from the long-term study and not as uniformly defined as the needle used in the other work. Additionally, the degree of erosion in this work was more significant, amounting to a difference of 170-210 μm, primarily attributed to the soft aluminum metal. Since aluminum is more susceptible to erosion than tungsten, deformation occurred at a lower voltage level and gas pressure than in the long-term study by T. Vu-Cong et al. Unfortunately, the weight of the protrusion defect was not measured and was only considered for analysis once the long-term experiment had commenced.

Another noteworthy observation is the lower PD apparent charge magnitude recorded in the long-term experiment compared to the preliminary test runs. This discrepancy is attributed to the off-center placement of the protrusion defect within the test setup.

In summary, the objective of analyzing the progressive, long-term evolution of PD behavior in protrusion defects was successfully achieved. A 30% increase in PD apparent charge magnitude, accompanied by a corresponding rise in PD repetition rate, was observed. The correlation between PD repetition rate and voltage polarity aligns with the findings of the long-term study by T. Vu-Cong et al. [10]. Furthermore, the observed changes in PD behavior were successfully attributed to erosion at the protrusion tip, consistent with the previous study. Notably, the tip radius erosion measured in this work was approximately seven times greater than that reported in the earlier study. Lastly, the NoDi* patterns reveal an intriguing similarity between the standing motion pattern of the free metallic particle defect and that of the protrusion defect. This raises the critical question of whether these two defects can be reliably distinguished, which is further explored in the following section.

6.3. Remarks Concerning Both Defect Types

With both defect types individually analyzed, several overarching observations emerge. The desired outcome was achieved despite the lower pressures and voltages tested in this study compared to existing literature. Measurable changes in the PD behavior were observed and the NoDi* patterns obtained closely resembled those from previous works, albeit with some notable differences. The protrusion defect exhibited a clear standing motion pattern on the first day, as shown in Figure 5.47b, closely matching the plot of K. Juhre et al. [41] in Figure 3.6a. Similarly, the free metallic particle defect displayed the characteristic firefly motion pattern in Figure 5.19d, though with more pronounced diagonals, resembling patterns reported by A. Pirker et al. [24] as shown in Figure 3.6b.

However, as the long-term experiments progressed, the NoDi* patterns of both defects began to converge, making them increasingly difficult to distinguish, as shown in Figure 6.3. While the PD apparent charge magnitudes differed between the protrusion defect in Figure 6.3a and the free metallic particle defect in Figure 6.3c, a closer analysis of the protrusion defect in Figure 6.3b reveals striking similarities. On one hand, this resemblance underscores the success of the protrusion defect characterization, as its behavior was intended to replicate the standing motion of a free metallic particle. However, more critically, this convergence in pattern characteristics raises concerns about the reliability of defect classification. The similarities may pose challenges for both untrained neural networks and human operators, increasing the likelihood of misclassification and emphasizing the need for refined diagnostic techniques.

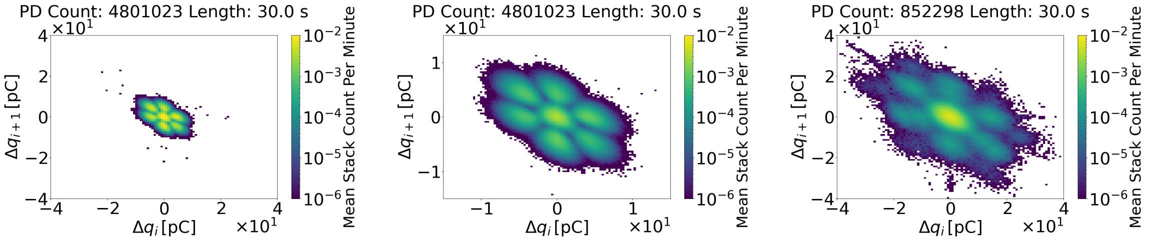

(a) Protrusion defect pattern **(b)** Closer view of protrusion defect pattern **(c)** Particle defect pattern (standing motion)

Figure 6.3: Comparison of the MPD magnitude difference NoDi* plots of the protrusion and free metallic particle defects at Day Four

Furthermore, space charge regions played an integral role in PD behavior, and their underlying mechanisms in other gases such as SF_6 have been extensively covered [44], [46]. As this work aimed to acquire the empirical results for the different defects over time, the specifics of space charge regions were not the main focus. Observations on space charge regions rely on more extensive PD capture devices such as high-speed cameras and photomultiplier tubes. Likewise, such measurement equipment would enable the capture of the particle motions and definitively confirm standing, hovering, or firefly motion at every instance over the long-term period.

In summary, determining whether the two defects can be reliably distinguished remains a complex challenge, as certain particle motions, such as standing, produce NoDi* patterns similar to those of a protrusion. A practical solution involves increasing the voltage to induce particle liftoff, triggering distinct patterns associated with bouncing, hovering, or firefly motions, which can help differentiate a free metallic particle from a protrusion. More importantly, comparing the long-term evolution of both defects and their respective changes in PD behavior leads to an intriguing conclusion: prolonged testing may not be necessary and could even hinder defect classification. In both cases, the most significant change in PD apparent charge magnitude occurred within the first two days of voltage application. Furthermore, since firefly motion is typically observed shortly after the initial voltage application, early-stage testing may be sufficient for accurate defect classification.

The next section covers the main discussion points of the test setup.

6.4. Test Setup

The test setup faced its fair share of issues, albeit none prevented the fulfillment of the main objectives. Early PD-free checks revealed that the short termination of the HVDC cable insulation generated PD activity and led to flashover at specific voltage levels. Background noise remained a persistent issue due to external interference from adjacent experiments. Better handling could have prevented the bending and breakage of the protrusion defect during the preliminary test runs. Appropriate measures were taken in each case, i.e., prolonging the insulation termination and taking additional precautions when handling delicate parts. Given the circumstances, the noise levels were managed to the operator's best efforts by implementing every possible measure, i.e., treating ground loops, swapping power supplies, and scheduling the PD measurements around the occurrence of other external experiments.

These issues were minor compared to two major oversights. Firstly, significant improvements are needed in the approach to PD measurements within the already configured test setup. Relying solely on visual inspection of the MPD software output is inadequate for confirming whether a test setup is genuinely PD-free. Instead, PD pulses should be systematically recorded and analyzed using the PSA plotter to quantify PD activity and identify recurring patterns. Secondly, automatic logging should be implemented to ensure continuous data collection, preventing gaps that could result in missed particle motion events.

The following section addresses the final objective: evaluating the analytical methods used and the feasibility of neural networks for long-term testing.

6.5. Analysis Methods

The analytical methods used in this work were effective, as the NoDi* plots generated from the captured data successfully differentiated between various particle motions and tracked changes in PD behavior over time. However, while these methods provided valuable insights, they are inadequate in certain cases, i.e., differentiating between the standing motion pattern of the free metallic particle defect and that of the protrusion defect, and limited to the test conditions they encompass. The logical next step is the integration of neural networks to advance their adoption in real-world conditions in the field.

Importantly, existing literature [48] has already addressed the challenge of training neural networks on datasets derived from long-term experiments. As a result, this work does not aim to contribute directly to that area. Instead, it fulfills a critical objective by promoting the standardization of data formatting for future neural network applications already set forth by other works. By utilizing NoDi* plots as the structured data format, this study hopes to ensure that future research can focus on refining neural network performance rather than grappling with data structuring issues. The PSA plotter was developed specifically to aid in the proliferation of NoDi* plots through its open-source nature and is further discussed in the following section.

6.5.1. PSA Plotter

Several key features and modifications were implemented in the PSA plotter to enhance its functionality. The code was initially adapted for the Omicron 600 device and required several revisions when transitioning to its counterpart, the 800 series. Additionally, new plot types, including density distribution and timescale plots, were added alongside the four original NoDi* pattern types. Improvements also included axis scaling and the ability to import UHF data. However, computing limitations became apparent when processing over ten million PD pulses. The Python script would freeze and take time to respond, highlighting the need for optimization to handle extensive datasets more efficiently.

6.6. Planning and Preparation

Despite careful planning and the best intentions, time constraints proved to be a major challenge. The delayed delivery of the GIS test cell from Siemens Energy significantly impacted the project timeline. Although the test cell was deemed ready for shipment as early as September 12th, it was not moved into the test facility until November 19th. During this waiting period, initial tests, as outlined in Appendix B, were conducted to make productive use of the available time. Thus, initial optimistic schedules were revised extensively to accommodate the shifting timeline.

The next chapter includes the conclusion of this work and the suggested future recommendations.

7

Conclusion

This study investigated key aspects of the long-term PD behavior of protrusion and free metallic particle defects in technical air under DC voltage. The primary objective, which was to analyze the progressive, long-term evolution of PD behavior in technical air under DC voltage stress in full-scale GIS and to compare the results with the long-term study by T. Vu-Cong et al. [10], was met. Both defect types exhibited increases in PD apparent charge magnitude and changes in repetition rate over time. Physical examination using microscope imaging and weight measurements confirmed surface erosion. The results align with the findings of the long-term study by T. Vu-Cong et al., reinforcing the correlation between changes in the PD behavior and tip radius erosion. Another objective of this work was to evaluate the degree of erosion in each defect type and assess the ability to distinguish between them reliably. A key finding was that while the two defects erode at different rates, they are not always easily distinguishable, particularly when the free metallic particle defect displays the standing motion behavior. Lastly, the third objective to adapt the long-term PD measurement data into a suitable format for defect classification and investigate the feasibility of using algorithms was fulfilled. The NoDi* format was successfully used to visualize PD activity, aligning with existing literature, and the feasibility of applying machine learning algorithms for defect classification was confirmed through the literature review, eliminating the need to replicate training efforts within this work.

Beyond the primary objectives, the long-term experiments provided additional insights. Notably, this study confirmed that existing knowledge from SF_6 and other SF_6 alternative gases, C_4FN–CO_2 and C_5FK-dry air, can be effectively applied to technical air. NoDi* plots from previous SF_6 studies successfully characterized defects in technical air, with only minor deviations. Additionally, the most significant changes in PD behavior occurred within the initial days of testing, aligning with the findings of T. Vu-Cong et al. [10]. The long-term experiments identified two days as the period for the most significant changes in PD behavior, whereas preliminary testing hinted at one day, compared to the three-day time frame reported by T. Vu-Cong et al. This early shift in PD characteristics underscores a key observation: prolonged testing may not be necessary and could even complicate defect classification. Prolonged testing has demonstrated similarities between the protrusion and free metallic particle defects, suggesting that early-stage testing provides a more accurate defect classification. Furthermore, the periodic motion of particles within the free metallic particle defect highlighted the challenge of accurately determining the number of particles present. The dominance of the firefly motion pattern obscured the presence of the standing motion, making it difficult to distinguish between individual particles. On a lesser note, this work emphasized the importance of UHF detection methods in localizing the PD activity, verifying the authenticity of the PD measurements obtained through the MPD device. Lastly, the relatively modest voltage and pressure levels used in this study, compared to previous works, did not hinder the results. The intended outcomes were successfully achieved, demonstrating changes in PD behavior.

This work serves to aid in the development and integration of air-insulated HVDC GIS into the existing energy grid. Research into PD behavior will continue to expand as efforts persist toward developing a standardized and comprehensive assessment framework for HVDC components. Future investigations generally focus on space charge mechanisms, the influence of multiple defects, and the correlation between PD severity and insulation degradation. These efforts will aid in the realization of more sustainable, resilient, and reliable power systems. Some potential recommendations based on the findings of this work are outlined in the next section.

7.1. Future Recommendations

Several recommendations can be made to advance future research on PD behavior in technical air. The first set relates to modifications in the GIS test cell and its associated setup. Increasing both the pressure and applied voltage levels would allow investigation into whether erosion at particle edges in both defect types progresses linearly with increased electrical stress. Additionally, applying negative polarity to both defect types in long-term experiments would offer valuable insight into how PD apparent charge magnitude and repetition rate evolve under reversed polarity. This would help further validate the correlation between repetition rate and voltage polarity, as previously reported by T. Vu-Cong et al. [10], since this work exclusively applied positive polarity to the HV conductor.

Further recommendations within the realm of the test setup focus on enhancing the quality and reliability of PD measurements. Improved shielding against external interference, such as the implementation of a complete Faraday cage, would significantly improve measurement accuracy. Likewise, the particle containment should be revised to minimize the interference to UHF equipment and offer an unobstructed view for visual capture devices through the viewing port. Moreover, integrating a fan within the GIS test cell could aid in circulating any decomposition byproducts, offering an additional area of study related to internal air currents and their potential effects within GIS systems.

The second set of recommendations focuses on deepening the understanding of the two defect types investigated. In particular, the free metallic particle defect warrants extensive further research, especially under multi-particle conditions, to develop reliable methods for accurately identifying the number of particles present. Particle motions such as firefly and standing remain sufficiently different, even under scenarios with particles of varying lengths and masses. Nonetheless, incorporating high-speed cameras could better correlate specific motion patterns with individual particles in such a dynamic test environment. Additionally, integrating photomultiplier tubes could enable further examination of the space charge behavior, particularly during the crucial initial days when most erosion occurs. For the protrusion defect, the prevailing assumption that an upright orientation adequately captures particle motion at liftoff may not be entirely true. As noted in discussions with the main author of the work [46], liftoff can occur at lower angles relative to the ground electrode. Future studies should investigate a range of protrusion angles to assess their impact on space charge distribution and corresponding NoDi* patterns.

More importantly, further research is needed to develop a robust method for distinguishing between protrusion defects and the standing motion of free metallic particle defects. As discussed in Section 6.3, the two defect types can exhibit overlapping PD patterns under specific conditions, making precise identification crucial.

References

[1] A. Alassi, S. Bañales, O. Ellabban, G. Adam, and C. MacIver, “HVDC Transmission: Technology Review, Market Trends and Future Outlook,” *Renewable and Sustainable Energy Reviews*, vol. 112, pp. 530–554, Sep. 2019, ISSN: 1364-0321. DOI: 10.1016/j.rser.2019.04.062. [Online]. Available: https://www.sciencedirect.com/science/article/pii/S1364032119302837 (visited on 10/03/2024).

[2] E. Csanyi, *Gas Insulated Substation (GIS) Versus Air Insulated Substation (AIS)*, en, Dec. 2016. [Online]. Available: https://electrical-engineering-portal.com/gas-insulated-substation-gis-vs-ais (visited on 10/03/2024).

[3] G. Mazzanti, G. Stomeo, and S. Mancini, “State of the Art in Insulation of Gas Insulated Substations: Main Issues, Achievements, and Trends,” en, *IEEE Electrical Insulation Magazine*, vol. 32, no. 5, pp. 18–31, Sep. 2016, ISSN: 0883-7554. DOI: 10.1109/MEI.2016.7552373. [Online]. Available: http://ieeexplore.ieee.org/document/7552373/ (visited on 09/10/2024).

[4] E. Önal, “Breakdown Characteristics of Gases in Non-uniform Fields,” en, *Journal of Electrical & Electronics Engineering*, vol. 4, pp. 1177–1182, 2004. [Online]. Available: https://www.researchgate.net/publication/228873410_BREAKDOWN_CHARACTERISTICS_OF_GASES_IN_NON-UNIFORM_FIELDS.

[5] S. Shi, Y. Li, Z. Cui, *et al.*, “Recent advances in degradation of the most potent industrial greenhouse gas sulfur hexafluoride,” *Chemical Engineering Journal*, vol. 470, p. 144 166, Aug. 2023, ISSN: 1385-8947. DOI: 10.1016/j.cej.2023.144166. [Online]. Available: https://www.sciencedirect.com/science/article/pii/S1385894723028978 (visited on 10/29/2024).

[6] *Fluorinated Gases and Ozone-depleting Substances: Council and Parliament Reach Agreement*, en, Aug. 2023. [Online]. Available: https://www.consilium.europa.eu/en/press/press-releases/2023/10/05/fluorinated-gases-and-ozone-depleting-substances-council-and-parliament-reach-agreement/ (visited on 08/30/2024).

[7] *Emission-free HV and MV Transmission Switchgear for AC and DC*, 2024. [Online]. Available: https://euprojectmission.net/ (visited on 08/30/2024).

[8] *Experis® ultra-high purity gases Technical specification Synthetic Air*, English, Nov. 2017. [Online]. Available: https://www.airproducts.ca/-/media/files/en/250/250-17-009-en-nov17-experis-ultra-high-purity-gases-technical-specification-synthetic-air.pdf (visited on 10/30/2024).

[9] K. Inami, T. Yoshida, H. Hama, Y. Nakadai, and T. Yamamoto, “Partial Discharge and Breakdown Properties in Dry Air, N2, and CO2 Under Nonuniform Electric Field,” en, *IEEE Transactions on Dielectrics and Electrical Insulation*, vol. 30, no. 6, pp. 2583–2591, Dec. 2023, ISSN: 1070-9878, 1558-4135. DOI: 10.1109/TDEI.2023.3292068. [Online]. Available: https://ieeexplore.ieee.org/document/10172047/ (visited on 09/24/2024).

[10] T. Vu-Cong, C. Toigo, F. Jacquier, *et al.*, “Long-Term Partial Discharge Behavior of Protrusion Defect in HVDC GIS,” en, *IEEE Transactions on Dielectrics and Electrical Insulation*, vol. 29, no. 6, pp. 2294–2302, Dec. 2022, ISSN: 1070-9878, 1558-4135. DOI: 10.1109/TDEI.2022.3206726. [Online]. Available: https://ieeexplore.ieee.org/document/9889682/ (visited on 08/27/2024).

[11] H. S. Kharal, M. Kamran, R. Ullah, M. Z. Saleem, and M. J. Alvi, “Environment-Friendly and Efficient Gaseous Insulator as a Potential Alternative to SF6,” en, *Processes*, vol. 7, no. 10, p. 740, Oct. 2019, ISSN: 2227-9717. DOI: 10.3390/pr7100740. [Online]. Available: https://www.mdpi.com/2227-9717/7/10/740 (visited on 08/27/2024).

[12] A. Pirker and U. Schichler, “Partial Discharges of Defects in Different Insulating Gases: N2, CO2, Dry Air and SF6,” en, in *2018 12th International Conference on the Properties and Applications of Dielectric Materials (ICPADM)*, Xi’an: IEEE, May 2018, pp. 140–143, ISBN: 978-1-5386-5788-1. DOI: `10.1109/ICPADM.2018.8401150`. [Online]. Available: `https://ieeexplore.ieee.org/document/8401150/` (visited on 08/27/2024).

[13] E. Ouss, L. Zavattoni, A. Beroual, A. Girodet, P. Vinson, and de Collongue, “Measurement and Analysis of Partial Discharges in HVDC Gas Insulated Substations,” en, Sep. 2017. DOI: `10.1109/EIC.2014.6869436`.

[14] S. Xiao, X. Zhang, J. Tang, and S. Liu, “A Review on SF6 Substitute Gases and Research Status of CF3I Gases,” en, *Energy Reports*, vol. 4, pp. 486–496, Nov. 2018, ISSN: 23524847. DOI: `10.1016/j.egyr.2018.07.006`. [Online]. Available: `https://linkinghub.elsevier.com/retrieve/pii/S2352484717301178` (visited on 10/11/2024).

[15] T. Götz, H. Kirchner, and K. Backhaus, “Partial Discharge Behaviour of a Protrusion in Gas-Insulated Systems under DC Voltage Stress,” en, *Energies*, vol. 13, no. 12, p. 3102, Jun. 2020, ISSN: 1996-1073. DOI: `10.3390/en13123102`. [Online]. Available: `https://www.mdpi.com/1996-1073/13/12/3102` (visited on 08/27/2024).

[16] C. Neumann, S. Neuhold, D. Steyn, *et al.*, “Dielectric Testing of Gas Insulated HVDC Systems,” en, *CIGRE*, Sep. 2021, ISSN: 978-2-85873-547-1.

[17] K. Juhre and C. Balkon, “Partial Discharge Measurement and Detectability of Imperfections in Synthetic Air Compared to SF6,” en, *IEEE International Conference on High Voltage Engineering and Applications*, pp. 151–154, 2024, ISSN: 979-8-3503-7498-8. (visited on 09/15/2024).

[18] M. Hartje, T. Kumm, B. Schober, U. Schichler, J. Torres, and P. Werle, “Reproducibility of Partial Discharge Measurements on Surface Discharges According to IEC60270 at DC and AC Voltages,” en, in *22nd International Symposium on High Voltage Engineering (ISH 2021)*, Hybrid Conference, Xi’an, China: Institution of Engineering and Technology, 2021, pp. 218–223, ISBN: 978-1-83953-605-2. DOI: `10.1049/icp.2022.0224`. [Online]. Available: `https://digital-library.theiet.org/content/conferences/10.1049/icp.2022.0224` (visited on 09/02/2024).

[19] H. Jiang, Y. Lai, Z. Gong, Y. Han, and T. Shao, “Simulation Comparison of the Positive and Negative Surface Discharges Induced by Metal Particles in a Plate–surface–plate Structure Under DC Excitation in Atmospheric Air,” en, *Journal of Physics D: Applied Physics*, vol. 57, no. 30, p. 305 202, Aug. 2024, ISSN: 0022-3727, 1361-6463. DOI: `10.1088/1361-6463/ad415d`. [Online]. Available: `https://iopscience.iop.org/article/10.1088/1361-6463/ad415d` (visited on 08/29/2024).

[20] R. Piccin, A. Rodrigo Mor, P. Morshuis, G. C. Montanari, and A. Girodet, “Partial Discharge Analysis and Monitoring in HVDC Gas Insulated Substations,” en, in *2014 IEEE Electrical Insulation Conference (EIC)*, Philadelphia, PA, USA: IEEE, Jun. 2014, pp. 488–492, ISBN: 978-1-4799-2789-0. DOI: `10.1109/EIC.2014.6869436`. [Online]. Available: `http://ieeexplore.ieee.org/document/6869436/` (visited on 08/27/2024).

[21] C. Mier Escurra, A. Khamlichi, M. Dalstein, *et al.*, “Methods for Partial Discharge Calibration in Gas-Insulated Substations for HVDC Power Grids and Charge Evaluation Uncertainty,” en, *IEEE Sensors Journal*, vol. 23, no. 19, pp. 23 486–23 493, Oct. 2023, ISSN: 1530-437X, 1558-1748, 2379-9153. DOI: `10.1109/JSEN.2023.3302871`. [Online]. Available: `https://ieeexplore.ieee.org/document/10215332/` (visited on 08/27/2024).

[22] C. P. Beura, P. Wenger, E. Tozan, M. Beltle, and S. Tenbohlen, “Classification of Partial Discharge Sources in HVDC Gas Insulated Switchgear using Neural Networks,” en, *VDE Hochspannungstechnik*, Nov. 2022, ISSN: 978-3-8007-5978-1.

[23] P. Morshuis and J. Smit, “Partial Discharges at DC Voltage: Their Mechanism, Detection and Analysis,” en, *IEEE Transactions on Dielectrics and Electrical Insulation*, vol. 12, no. 2, pp. 328–340, Apr. 2005, ISSN: 1070-9878. DOI: `10.1109/TDEI.2005.1430401`. [Online]. Available: `http://ieeexplore.ieee.org/document/1430401/` (visited on 10/01/2024).

[24] A. Pirker and U. Schichler, “Partial Discharge Measurement at DC Voltage - Evaluation and Characterization by NoDi* Pattern,” en, *IEEE Transactions on Dielectrics and Electrical Insulation*, vol. 25, no. 3, pp. 883–891, Jun. 2018, ISSN: 1070-9878, 1558-4135. DOI: 10.1109/TDEI.2018.006742. [Online]. Available: https://ieeexplore.ieee.org/document/8410717/ (visited on 08/27/2024).

[25] F. Zeng, J. Tang, X. Zhang, S. Zhou, and C. Pan, “Typical Internal Defects of Gas-Insulated Switchgear and Partial Discharge Characteristics,” in Oct. 2018, ISBN: 978-1-78923-768-9. DOI: 10.5772/intechopen.79090.

[26] W. Hauschild and E. Lemke, *High-Voltage Test and Measuring Techniques*, en. Berlin, Heidelberg: Springer Berlin Heidelberg, 2014, ISBN: 978-3-642-45351-9. DOI: 10.1007/978-3-642-45352-6. [Online]. Available: https://link.springer.com/10.1007/978-3-642-45352-6 (visited on 09/13/2024).

[27] C. Li, T. Shahsavarian, M. A. Baferani, K. Davis, Y. Cao, and D. Zhang, “Understanding DC Partial Discharge: Recent Progress, Challenges, and Outlooks,” en, *CSEE Journal of Power and Energy Systems*, vol. 8, no. 3, pp. 894–909, May 2022, ISSN: 2096-0042. DOI: 10.17775/CSEEJPES.2021.04740. [Online]. Available: https://www.sciopen.com/article/10.17775/CSEEJPES.2021.04740 (visited on 11/16/2024).

[28] N. Taylor, “Dielectric Response and Partial Discharge Measurements on Stator Insulation at Varied Low Frequency,” en, 2010, ISBN: 978-91-7415-713-0. [Online]. Available: https://www.semanticscholar.org/paper/Dielectric-response-and-partial-discharge-on-stator-Taylor/ef3939f88a650e8015f2e3cc96d728039a0f4b9e (visited on 09/09/2024).

[29] E. Lemke, “A Critical Review of Partial-Discharge Models,” en, *IEEE Electrical Insulation Magazine*, vol. 28, no. 6, pp. 11–16, Nov. 2012, ISSN: 0883-7554. DOI: 10.1109/MEI.2012.6340519. [Online]. Available: http://ieeexplore.ieee.org/document/6340519/ (visited on 09/27/2024).

[30] P. Mráz, S. A. Madhar, P. Treyer, and U. Hammer, “Guidelines for PD Measurement According to IEC60270,” en, *21st International Symposium on High Voltage Engineering*, 2019.

[31] P. Wenger, M. Beltle, S. Tenbohlen, and U. Riechert, “UHF-PD Measurement and High-Speed-Imaging of Firefly Motion at the Positive Electrode in HVDC-GIS,” en, in *2019 IEEE Conference on Electrical Insulation and Dielectric Phenomena (CEIDP)*, Richland, WA, USA: IEEE, Oct. 2019, pp. 389–392, ISBN: 978-1-7281-3121-4. DOI: 10.1109/CEIDP47102.2019.9009749. [Online]. Available: https://ieeexplore.ieee.org/document/9009749/ (visited on 01/28/2025).

[32] M. Hartje, L. Kästingschäfer, M. Farahani, P. Werle, A. Pirker, and U. Schichler, “Applicability of IEC 60270 for partial discharge measurements under DC voltage - results of a round Robin test,” en, *International Symposium on High Voltage Engineering*, no. 20, 2017.

[33] M. Sze and M. Lachance, *A Guide for Partial Discharge Measurements on Medium Voltage (MV) and High Voltage (HV) Apparatus - Part 2 - Measurement According to IEC60270*, en, 2020. [Online]. Available: https://www.google.com/url?sa=t&source=web&rct=j&opi=89978449&url=https://www.omicronenergy.com/download/file/e5e8a545dfbaebe53f6487fe7f4886a9&ved=2ahUKEwiWtc34s96IAxUVGxAIHTE_C6gQFnoECBIQAQ&usg=AOvVaw1efD7vmRQJOFF2efvhiVw-.

[34] “IEC 60270:2000 High-voltage test techniques - Partial discharge measurements,” en, *IEC*, no. 3, p. 50, Dec. 2000, ISSN: 2831855071.

[35] *MPD 800 User Manual*, en, 2021. [Online]. Available: https://www.omicronenergy.com/download/document/4DDF26D7-7482-494C-9DAB-68FAFC008401/.

[36] G. C. Stone, A. Cavallini, G. Behrmann, and C. A. Serafino, “Electromagnetic (RF) PD Detection,” en, in *Practical Partial Discharge Measurement on Electrical Equipment*, John Wiley & Sons, Ltd, 2023, pp. 137–158, ISBN: 978-1-119-83334-5. [Online]. Available: https://onlinelibrary.wiley.com/doi/abs/10.1002/9781119833345.ch7 (visited on 01/12/2025).

[37] U. Fromm, “Interpretation of partial discharges at dc voltages,” *IEEE Transactions on Dielectrics and Electrical Insulation*, vol. 2, no. 5, pp. 761–770, Oct. 1995, Conference Name: IEEE Transactions on Dielectrics and Electrical Insulation, ISSN: 1558-4135. DOI: 10.1109/94.469972. [Online]. Available: https://ieeexplore.ieee.org/document/469972 (visited on 01/18/2025).

[38] M. Florkowski, D. Krześniak, M. Kuniewski, and P. Zydron, “Partial Discharge Imaging Correlated with Phase-Resolved Patterns in Non-Uniform Electric Fields with Various Dielectric Barrier Materials,” *Energies*, vol. 13, p. 2676, May 2020. DOI: `10.3390/en13112676`.

[39] S. Kainaga, A. Pirker, and U. Schichler, “Identification of Partial Discharges at DC Voltage Using Machine Learning Methods,” en, *International Symposium on High Voltage Engineering*, no. 20, 2017. [Online]. Available: `https://www.e-cigre.org/publications/detail/ish2017-528-identification-of-partial-discharges-at-dc-voltage-using-machine-learning-methods.html`.

[40] B. Schober and U. Schichler, “Application of Machine Learning for Partial Discharge Classification under DC Voltage,” en, *Proceedings of the Nordic Insulation Symposium*, no. 26, pp. 16–21, Aug. 2019, ISSN: 2535-3969. DOI: `10.5324/nordis.v0i26.3268`. [Online]. Available: `https://www.ntnu.no/ojs/index.php/nordis/article/view/3268` (visited on 09/21/2024).

[41] K. Juhre, M. Geske, M. Kosse, and R. Plath, “Feasibility Study on the Applicability of Clean Air in Gas-insulated DC Systems,” in *VDE High Voltage Technology 2020; ETG-Symposium*, Nov. 2020, pp. 1–6. [Online]. Available: `https://ieeexplore.ieee.org/document/9275521` (visited on 12/11/2024).

[42] Y. Li, B. Zhang, X. Li, *et al.*, “Optimization of Insulators in ±550 kV HVDC GIS for Offshore Wind Platform Considering Charge Accumulation,” *Electric Power Systems Research*, vol. 223, p. 109 549, Oct. 2023, ISSN: 0378-7796. DOI: `10.1016/j.epsr.2023.109549`. [Online]. Available: `https://www.sciencedirect.com/science/article/pii/S0378779623004388` (visited on 10/03/2024).

[43] T. Vu-Cong, M. Dalstein, C. Toigo, F. Jacquier, and A. Girodet, “Partial discharge measurement in DC GIS: Comparison between conventional and UHF methods,” in *2021 IEEE Conference on Electrical Insulation and Dielectric Phenomena (CEIDP)*, ISSN: 2576-2397, Dec. 2021, pp. 607–610. DOI: `10.1109/CEIDP50766.2021.9705420`. [Online]. Available: `https://ieeexplore.ieee.org/document/9705420` (visited on 12/08/2024).

[44] L. Liu and J. Wang, “The Analysis of GIS Defect Model Partial Discharge Test,” en, in *Proceedings of the 2016 International Conference on Energy, Power and Electrical Engineering*, Shenzhen, China: Atlantis Press, 2016, ISBN: 978-94-6252-258-9. DOI: `10.2991/epee-16.2016.59`. [Online]. Available: `http://www.atlantis-press.com/php/paper-details.php?id=25864828` (visited on 12/10/2024).

[45] T. Berg, K. Juhre, T. Fedtke, H. Koch, and C. Neumann, “Specific Characteristics of Particle Traps for Application in DC gas-insulated transmission lines (DC GIL),” in *VDE High Voltage Technology 2020; ETG-Symposium*, Nov. 2020, pp. 1–8. [Online]. Available: `https://ieeexplore.ieee.org/document/9275552` (visited on 12/11/2024).

[46] P. Wenger, M. Beltle, S. Tenbohlen, U. Riechert, and G. Behrmann, “Combined Characterization of Free-Moving Particles in HVDC-GIS Using UHF PD, High-Speed Imaging, and Pulse-Sequence Analysis,” *IEEE Transactions on Power Delivery*, vol. 34, no. 4, pp. 1540–1548, Aug. 2019, Conference Name: IEEE Transactions on Power Delivery, ISSN: 1937-4208. DOI: `10.1109/TPWRD.2019.2909830`. [Online]. Available: `https://ieeexplore.ieee.org/abstract/document/8684218` (visited on 01/20/2025).

[47] J. Sun, W. Chen, K. Bian, Z. Li, X. Yan, and Y. Xu, “Movement characteristics of ball metallic particle between ball-plane electrodes under DC voltage,” *IEEE Transactions on Dielectrics and Electrical Insulation*, vol. 25, no. 3, pp. 1047–1055, Jun. 2018, Conference Name: IEEE Transactions on Dielectrics and Electrical Insulation, ISSN: 1558-4135. DOI: `10.1109/TDEI.2018.006879`. [Online]. Available: `https://ieeexplore.ieee.org/abstract/document/8410735` (visited on 11/20/2024).

[48] M. Dalstein, M. Medlock, G. Clerc, *et al.*, “Partial Discharge Defect Recognition Tool For MV/HV DC Equipment,” in *2022 IEEE 4th International Conference on Dielectrics (ICD)*, Jul. 2022, pp. 360–363. DOI: `10.1109/ICD53806.2022.9863490`. [Online]. Available: `https://ieeexplore.ieee.org/document/9863490` (visited on 11/26/2024).

A

Source Code

A.1. Python Script for NoDi* Plots

A.1.1. GUI File for NoDi* Plots

```python

import tkinter as tk
from tkinter import filedialog, messagebox
from tkinter import *
import matplotlib.pyplot as plt
from readQ import setup_Qfile
from readQ import nodi_plot
from readQ import setup_csvfile
import numpy as np
import pandas as pd
from tkinter import font as tkFont

# Function to select a file
def select_file():
    file_path = filedialog.askopenfilename()
    if file_path:
        file_label.config(text=file_path)  # Display file name in the label
        global selected_file, Time, Data, Count, file_length
        selected_file = file_path  # Store the selected file path
        if file_path.endswith('.Q'):
            [Time,Data,Count] = setup_Qfile(selected_file,"end")
        elif file_path.endswith('.csv'):
            [Time,Data,Count] = setup_csvfile(selected_file,"end")
        else:
            msg = print('file #s could not be opened - check folder!')
            [Time,Data,Count] = [0,0,0]
        # insert code for displaying the file length
        file_length = np.round((max(Time) - min(Time)),2)
        file_label_length.config(text="File length: " + str(file_length) + " (s)")

# Function to run plotting
def run_plotting():
    global Time, Data, Count, file_length
    Time_temp = Time
    Data_temp = Data
    Count_temp = Count

    try:
        # insert code for checking the correct bounds
        if checkbox_var_length.get() is False:
            start = float(input_entry_start.get())   # Get user input as string
            end = float(input_entry_end.get()) # Get user input as string
            if (start < end) and (end < file_length):

                Time_temp = np.array([t for t in Time if start <= t <= end])
                Data_temp = np.array([m for t, m in zip(Time, Data) if start <= t <= end])
```

```python
                Count_temp = np.size(Data_temp)

        input_value_plot = dropdown_var_plot.get()  # Get user input as string
        input_grid_size = int(dropdown_var_grid_size.get())

        x_scale = input_entry_xscale.get()
        y_scale = input_entry_yscale.get()

        save_data = nodi_plot(Time_temp,Data_temp,Count_temp,input_value_plot,input_grid_size,x_scale,y_scale)
        if checkbox_var_save.get() is True:
            df = pd.DataFrame(save_data)
            df.to_csv(selected_file + "_" + input_value_plot.replace(" ", "") + "_pulses_" + str(Count_temp) + str(input_grid_size) + "_file.csv")

    except ValueError:
        messagebox.showerror("Invalid input", "Please enter a valid file length.")

# Create the main window
root = tk.Tk()
root.title("NoDi* Plotter")
font_size = 16
button_size = tkFont.Font(family='Helvetica', size=12)

root.geometry("800x350")

# Label and button for file selection
file_label = tk.Label(root, text="No file selected")
file_label.pack(pady=5)

file_button = tk.Button(root, text="Select File", command=select_file, font=(button_size))
file_button.pack(pady=1)

# Label for file length
file_label_length = tk.Label(root, text="File length: (empty) (s)")
file_label_length.pack(pady=1)

# Label and Entry for file length selecion
input_length_label = tk.Label(root, text="Enter desired length(s): (Start) (End)")
input_length_label.pack(pady=5)

input_frame = tk.Frame(root)
input_frame.pack(pady=1)

input_entry_start = tk.Entry(input_frame, width=15)
input_entry_start.pack(side=tk.LEFT, padx=5)

input_entry_end = tk.Entry(input_frame, width=15)
input_entry_end.pack(side=tk.LEFT, padx=5)

checkbox_var_length = tk.BooleanVar()
checkbox_length = tk.Checkbutton(input_frame, text="Whole File", variable=checkbox_var_length, font=(button_size))
checkbox_length.pack(side=tk.LEFT, padx=5)

# Label and Entry for plot option
input_frame_2 = tk.Frame(root)
input_frame_2.pack(pady=1)

dropdown_label = tk.Label(input_frame_2, text="Select a plot option:", font=(font_size))
dropdown_label.pack(side=tk.LEFT, padx=5)

dropdown_var_plot = tk.StringVar(input_frame_2)
dropdown_var_plot.set("Q(i+1) and Q(i)")  # Set default option

options = ["Q(i+1) and Q(i)", "T(i+1) and T(i)", "T(i) and Q(i)", "Q(i)/T(i) and T(i)","Timescale","Q Density","T Density"]  # List of options
dropdown_menu_plot = tk.OptionMenu(input_frame_2, dropdown_var_plot, *options)
dropdown_menu_plot.pack(side=tk.LEFT, padx=5)
dropdown_menu_plot.config(font=button_size) # set the button font

```

```python
# Label and entry for grid size
input_frame_3 = tk.Frame(root)
input_frame_3.pack(pady=1)

dropdown_label_grid_size = tk.Label(input_frame_3, text="Select a grid size:", font=(font_size))
dropdown_label_grid_size.pack(side=tk.LEFT, padx=5)

dropdown_var_grid_size = tk.StringVar(input_frame_3)
dropdown_var_grid_size.set("100")  # Set default option

options_grid = ["25", "100"]  # List of options
dropdown_menu_grid_size = tk.OptionMenu(input_frame_3, dropdown_var_grid_size, *options_grid)
dropdown_menu_grid_size.pack(side=tk.LEFT, padx=5)
dropdown_menu_grid_size.config(font=button_size) # set the button font

# Label and entry for scaling factor
input_frame_5 = tk.Frame(root)
input_frame_5.pack(pady=1)

scale_factor_label = tk.Label(input_frame_5, text="Enter X and Y scale (pC)", font=(font_size))
scale_factor_label.pack(side=tk.LEFT, padx=5)

input_entry_xscale = tk.Entry(input_frame_5, width=15)
input_entry_xscale.pack(side=tk.LEFT, padx=5)

input_entry_yscale = tk.Entry(input_frame_5, width=15)
input_entry_yscale.pack(side=tk.LEFT, padx=5)

# Label and entry for plotting
input_frame_4 = tk.Frame(root)
input_frame_4.pack(pady=10)

plot_button = tk.Button(input_frame_4, text="Create Plots", command=run_plotting, font=(button_size))
plot_button.pack(side=tk.LEFT,padx=5)

checkbox_var_save = tk.BooleanVar()
checkbox_save = tk.Checkbutton(input_frame_4,text="Save Array", variable=checkbox_var_save, font=(button_size))
checkbox_save.pack(side=tk.LEFT,padx=5)

[wid.config(font=(None,font_size)) for wid in root.winfo_children() if isinstance(wid, Label) ]
# Run the GUI loop
root.mainloop()
```

A.1.2. Read Data from Omicron MPD or UHF File

```python


#import packages
import numpy as np
import matplotlib.pyplot as plt
#from scipy.stats import gaussian_kde
from matplotlib.ticker import LogFormatter
#from mpl_toolkits.mplot3d import Axes3D
from matplotlib.colors import LogNorm
import matplotlib.ticker as ticker

import pandas as pd
from datetime import datetime
import re

def setup_Qfile(sourcefile,command):

    # the value of command determines the length of the reading
    if not command.isdigit():
        f = open(sourcefile, 'rb')
```

```
        content = f.read()
        num_bytes = len(content)
        count = int(num_bytes/12)
        f.close()
    else:
        count = int(command)

    return readQ(sourcefile,count)

def  readQ(sourcefile,Count):
    #file gets opened
    f = open(sourcefile, 'rb')
    if f == -1:
        msg = print('file #s could not be opened - check folder!')
        return [0,0,0]
    counter=0
    # reset Matrix to Null
    Time = np.zeros((Count))
    # reset Matrix to Null
    Data = np.zeros((Count))
    # read file unitl count is reached
    while (counter < Count):
        # Charge
        q = np.fromfile(f,dtype='float32',count=1) # 4 Bytes
        # Time
        t = np.fromfile(f,dtype='float64',count=1); # 8 Bytes
        # if data avaiable
        if q.size > 0 and t.size > 0:
            # store results
            Time[counter]=t[0]
            Data[counter]=q[0]
            counter=counter+1
    #file gets closed
    f.close()
    # returns the three important data types
    return[Time,Data,counter]

def setup_csvfile(sourcefile,command):
    # Read the semicolon-separated file into a DataFrame
    data = pd.read_csv(sourcefile, delimiter=';', skiprows=1, header=None, names=["UTC_Time",
         "Value"])
    values = data["Value"].astype(float)
    Data = values.to_numpy(dtype='float64')

    # the value of command determines the length of the reading
    if not command.isdigit():
        count = len(Data)
    else:
        count = int(command)

    Time = np.zeros((count))
    counter = 0
    temp = data["UTC_Time"]
    while (counter < count):
        first_split = temp[counter].split(":")
        second_split = first_split[0].split(" ")
        seconds = re.sub(r'\.\.+', '.', str(first_split[2]))
        Time[counter] = float(second_split[1])*3600 + float(first_split[1])*60 + float(
            seconds)
        counter=counter+1
    Time = Time - Time[0]
    # Convert to arrays
    return [Time,Data,count]

def nodi_plot(Time,Data,Count,Plot_command, grid_size, xscale, yscale):
    #responsible for the creation of the nodi* plots
    # sets up the matrix for the magnitude calculation
    magnitude_i = np.zeros(Count)
    magnitude_i_1 = np.zeros(Count)
    # sets up the matrix for the time calculation
    time_i = np.zeros(Count)
```

```python
    time_i_1 = np.zeros(Count)
    # sets up the counter for the calculation; set to 2 as calculation takes PD before and after into account
    counter = 1
    counter2 = 0
    # performs the calculation for each PD pulse
    while(counter < (Count-1)):
        # magnitude
        magnitude_i[counter2] = Data[counter] - Data[counter-1]
        magnitude_i_1[counter2] = Data[counter+1] - Data[counter]
        # time
        time_i[counter2] = Time[counter] - Time[counter-1]
        time_i_1[counter2] = Time[counter+1] - Time[counter]
        counter = counter + 1
        counter2 = counter2 + 1
    print(str(np.average(Data)) + " " + str(np.min(Data)) + " " + str(np.average(time_i)))

    # clean the lists
    zero_indices_time = np.where(time_i <= 0)
    zero_indices_time_i = np.where(time_i_1 <= 0)

    # Remove entries from both lists at the zero indices
    magnitude_i = np.delete(magnitude_i, zero_indices_time)
    time_i = np.delete(time_i, zero_indices_time)

    magnitude_i_1 = np.delete(magnitude_i_1, zero_indices_time_i)
    time_i_1 = np.delete(time_i_1, zero_indices_time_i)

    # create 2D plot
    # sets up the plot labels
    if Plot_command == 'Q(i+1) and Q(i)':
        x = magnitude_i/(10**-12)
        y = magnitude_i_1/(10**-12)
        word = 'Magnitude'
        xlabel = r'$\Delta q_{{i}} \, \text{[pC]}$'
        ylabel = r'$\Delta q_{{i+1}} \, \text{[pC]}$'
        if xscale != "" and yscale != "":
            if int(xscale) > 0 and int(yscale) > 0:
                x_bins = np.linspace(-int(xscale), int(xscale), grid_size)
                y_bins = np.linspace(-int(yscale), int(yscale), grid_size)
        else:
            x_bins = np.linspace(min(x), max(x), grid_size)
            y_bins = np.linspace(min(y), max(y), grid_size)
        nodi_plot_2D_3D(x,y,word,xlabel,ylabel,grid_size,Time,Count, x_bins, y_bins)
    elif Plot_command == 'T(i+1) and T(i)':
        x = time_i
        y = time_i_1
        word = 'Time'
        xlabel = r'$\Delta t_{{i}} \, \text{[s]}$'
        ylabel = r'$\Delta t_{{i+1}} \, \text{[s]}$'
        if xscale != "" and yscale != "":
            if float(xscale) > 0 and float(yscale) > 0:
                x_bins = np.linspace(0, float(xscale), grid_size)
                y_bins = np.linspace(0, float(yscale), grid_size)
        else:
            x_bins = np.linspace(min(x), max(x), grid_size)
            y_bins = np.linspace(min(y), max(y), grid_size)
        nodi_plot_2D_3D(x,y,word,xlabel,ylabel,grid_size,Time,Count, x_bins, y_bins)
    elif Plot_command == 'T(i) and Q(i)':
        x = magnitude_i/(10**-12)
        y = time_i
        word = 'Time and Magnitude'
        xlabel = r'$\Delta q_{{i}} \, \text{[pC]}$'
        ylabel = r'$\Delta t_{{i}} \, \text{[s]}$'
        if xscale != "" and yscale != "":
            if int(xscale) > 0 and int(yscale) > 0:
                x_bins = np.linspace(-int(xscale), int(xscale), grid_size)
                y_bins = np.linspace(-int(yscale), int(yscale), grid_size)
        else:
            x_bins = np.linspace(min(x), max(x), grid_size)
            y_bins = np.linspace(min(y), max(y), grid_size)
```

```
        nodi_plot_2D_3D(x,y,word,xlabel,ylabel,grid_size,Time,Count, x_bins, y_bins)
    elif Plot_command == 'Q(i)/T(i) and T(i)':
        x = time_i
        y = (magnitude_i / time_i)/(10**-12)
        word = 'Magnitude and Time'
        xlabel = r'$\Delta t_{{i}} \, \text{[s]}$'
        ylabel = r'$\Delta q_{{i}}/ \Delta t_{{i}} \, \text{[pC/s]}$'
        if xscale != "" and yscale != "":
            if int(xscale) > 0 and int(yscale) > 0:
                x_bins = np.linspace(-int(xscale), int(xscale), grid_size)
                y_bins = np.linspace(-int(yscale), int(yscale), grid_size)
        else:
            x_bins = np.linspace(min(x), max(x), grid_size)
            y_bins = np.linspace(min(y), max(y), grid_size)
        nodi_plot_2D_3D(x,y,word,xlabel,ylabel,grid_size,Time,Count, x_bins, y_bins)
    elif Plot_command == 'Timescale':
        x = Time
        y = Data/(10**-12)
        word = 'Timescale (PD Count: ' + str(Count) + ')'
        xlabel = 'Time [s]'
        ylabel = 'Magnitude [pC]'
        time_scale_plot(x,y,word,xlabel,ylabel)
    elif Plot_command == 'Q Density':
        x = Data/(10**-12)
        xlabel = 'Magnitude Differences [pC]'
        ylabel = 'Count'
        word = 'Density Function of Magnitude Differences'
        plot_density_distribution(x,word,xlabel,ylabel)
    elif Plot_command == 'T Density':
        x = Time
        xlabel = 'Time Differences [s]'
        ylabel = 'Count'
        word = 'Density Function of Time Differences'
        plot_density_distribution(x,word,xlabel,ylabel)
    else:
        msg = print('Command is wrong!')
        return 0

def nodi_plot_2D_3D(x,y,word,xlabel,ylabel,grid_size,Time,Count, x_bins, y_bins):

    # 2D histogram to count the number of points in each bin
    H, xedges, yedges = np.histogram2d(x, y, bins=[x_bins, y_bins])

    # Calculate the number of minutes (assuming time is in seconds)
    num_seconds = (max(Time) - min(Time))/60

     # Calculate the mean stack count per minute
    mean_stack_count_per_min = np.sum(H) / num_seconds

    # Scale the stack heights by the mean stack count per minute
    H_scaled = (H / mean_stack_count_per_min)

    titlesize = 40
    labelsize = 40
    ticksize = 40
    norm = LogNorm(vmin=1e-6, vmax=1e-2)  # Adjust vmin and vmax as needed

    # Create a square figure
    fig, ax = plt.subplots(figsize=(12, 8))  # Adjust the size as needed
    ax.set_aspect('equal')  # Ensure a square aspect ratio for the axes

    # Plot the log-scaled density as a heatmap
    plt.imshow(H_scaled.T, origin='lower', aspect='auto', extent=[xedges[0], xedges[-1],
        yedges[0], yedges[-1]],cmap='viridis',norm=norm)
    ax = plt.gca()

    # Set the y-axis to use exponential notation
    ax.xaxis.set_major_formatter(ticker.ScalarFormatter(useMathText=True))
    ax.ticklabel_format(style='sci', axis='x', scilimits=(0, 0))
    ax.yaxis.set_major_formatter(ticker.ScalarFormatter(useMathText=True))
    ax.ticklabel_format(style='sci', axis='y', scilimits=(0, 0))
```

```python
    ax.tick_params(axis='both', labelsize=ticksize)
    tx = ax.xaxis.get_offset_text()
    tx.set_fontsize(ticksize)
    ty = ax.yaxis.get_offset_text()
    ty.set_fontsize(ticksize)

    # Add a colorbar with logarithmic scale
    cbar = plt.colorbar()
    cbar.set_label('Mean Stack Count Per Minute', size = 36)
    cbar.ax.tick_params(labelsize=ticksize)

    #cbar.set_label('Normalized Values')

    # Add labels and title
    plt.xlabel(xlabel, size = labelsize)
    plt.ylabel(ylabel, size = labelsize)
    file_length = np.round((max(Time) - min(Time)),2)
    plt.title('PD Count: ' + str(Count) + ' Length: ' + str(file_length) + ' s', size =
        titlesize)
    #mng = plt.get_current_fig_manager()
    #mng.window.state('zoomed')
    plt.subplots_adjust(left=0.14, bottom=0.178, right=0.918, top=0.854, wspace=0.2, hspace
        =0.2)
    plt.tight_layout()
    plt.show()

    # Create 3D plot

    titlesize = 30
    labelsize = 20
    ticksize = 20

    # Create a meshgrid for the surface plot
    X, Y = np.meshgrid(xedges[:-1], yedges[:-1])

    # Plotting the 3D heatmap
    fig = plt.figure()
    ax = fig.add_subplot(111, projection='3d')

    surf = ax.plot_surface(X, Y, np.transpose(H_scaled), cmap='viridis', edgecolor='none',
        norm=LogNorm())
    ax.xaxis.set_major_formatter(ticker.ScalarFormatter(useMathText=True))
    ax.ticklabel_format(style='sci', axis='x', scilimits=(0, 0))
    ax.yaxis.set_major_formatter(ticker.ScalarFormatter(useMathText=True))
    ax.ticklabel_format(style='sci', axis='y', scilimits=(0, 0))
    ax.tick_params(axis='both', labelsize=ticksize)
    tx = ax.xaxis.get_offset_text()
    tx.set_fontsize(ticksize)
    ty = ax.yaxis.get_offset_text()
    ty.set_fontsize(ticksize)

    # Set labels
    ax.set_xlabel(xlabel, size = labelsize)
    ax.set_ylabel(ylabel, size = labelsize)
    #ax.set_title('3D Heatmap of Normalized ' + word +' Differences (PD Count: ' + str(Count)
         + ')', size = titlesize)

    # Create an axes for the colorbar
    cax = fig.add_axes([0.9, 0.1, 0.03, 0.8])  # [left, bottom, width, height]

    # Create a colorbar with log normalization
    mappable = plt.cm.ScalarMappable(cmap='viridis', norm=LogNorm())
    mappable.set_array(H_scaled)

    # Create colorbar using the new axes
    cbar = plt.colorbar(mappable, cax=cax)
    cbar.set_label('Mean Stack Count Per Minute', size = labelsize)
    cbar.ax.tick_params(labelsize=ticksize)
    mng = plt.get_current_fig_manager()
    mng.window.state('zoomed')
    plt.show()
```

```
    return H_scaled.T

def time_scale_plot(x,y,word,xlabel,ylabel):
    # plotting the timescale
    titlesize = 40
    labelsize = 40
    ticksize = 40
    x = x - min(x)

    plt.subplots(figsize=(12, 8))  # Adjust the size as needed
    plt.title(word, size = titlesize)
    plt.xlabel(xlabel, size = labelsize)
    plt.ylabel(ylabel, size = labelsize)
    plt.plot(x, y, marker='o', linestyle='-', color='b', linewidth=1, markersize=2)

     # Adding grid lines for better visualization
    plt.grid(True, which='both', linestyle='--', linewidth=0.6, alpha=0.7)

    # Customizing tick parameters for a cleaner look
    plt.tick_params(axis='both', which='major', labelsize=ticksize)
    plt.subplots_adjust(left=0.12, bottom=0.12, right=0.98, top=0.94, wspace=None, hspace=
        None)

    #mng = plt.get_current_fig_manager()
    #mng.window.state('zoomed')
    plt.tight_layout()
    plt.show()

    return [x, y]

def plot_density_distribution(data,word,xlabel,ylabel):

    if len(data) < 2:
        print("Not enough data to create density plots.")
        return

    # Calculate differences
    diffs = np.diff(data)

    #zero_indices = np.where(diffs == 0)
    #diffs = np.delete(diffs, zero_indices)
    titlesize = 40
    labelsize = 40
    ticksize = 40

    # Create a density plot for time differences
    plt.subplots(figsize=(12, 8))  # Adjust the size as needed
    plt.hist(diffs, bins=1000, density=False, color='skyblue', edgecolor='black')
    plt.yscale('log')
    plt.title(word, size=titlesize)
    plt.xlabel(xlabel, size = labelsize)
    plt.ylabel(ylabel, size = labelsize)
    plt.grid(visible=True, which='both', color='gray', linestyle='--', linewidth=0.5)
    plt.tick_params(axis='both', which='major', labelsize=ticksize)
    plt.subplots_adjust(left=0.08, bottom=0.08, right=0.98, top=0.95, wspace=None, hspace=
        None)

    #mng = plt.get_current_fig_manager()
    #mng.window.state('zoomed')
    plt.tight_layout()
    plt.show()

    zero_indices_diffs = np.where(diffs < 0)
    diffs = np.delete(diffs, zero_indices_diffs)

    plt.subplots(figsize=(12, 8))  # Adjust the size as needed
    plt.hist(diffs, bins=1000, density=False, color='skyblue', edgecolor='black')
    plt.yscale('log')
    plt.title(word, size=titlesize)
    plt.xlabel(xlabel, size = labelsize)
    plt.ylabel(ylabel, size = labelsize)
```

```
    plt.grid(visible=True, which='both', color='gray', linestyle='--', linewidth=0.5)
    plt.tick_params(axis='both', which='major', labelsize=ticksize)
    plt.subplots_adjust(left=0.08, bottom=0.08, right=0.98, top=0.95, wspace=None, hspace=None)

    #mng = plt.get_current_fig_manager()
    #mng.window.state('zoomed')
    plt.tight_layout()
    plt.show()

    return diffs
```

A.1.3. PD apparent charge magnitude and repetition rate plot

```
import matplotlib.pyplot as plt
import numpy as np
from matplotlib.ticker import (MultipleLocator,
                               FormatStrFormatter,
                               AutoMinorLocator)

# Data
labels = [
    "Day 1 - One", "Day 1 - Two", "Day 2 - One", "Day 2 - Two",
    "Day 3 - One", "Day 3 - Two", "Day 4 - One", "Day 4 - Two"
]
values1 = [-116, -35, -40, -152, -132, -40, -44, -44]
values2 = [5.59E+04, 5.29E+04, 3.37E+04, 4.85E+04,
           3.39E+04, 3.66E+04, 2.86E+04, 3.45E+04]

titlesize = 30
labelsize = 24
ticksize = 24
fig, ax1 = plt.subplots(figsize=(12, 8))

# Primary axis
ax1.plot(labels, values1, marker='o', linestyle='-', color='b', label="PD Apparent Charge Magnitude [pC]")
ax1.set_ylabel("PD Apparent Charge Magnitude [pC]", color='b', fontsize=24)
ax1.tick_params(axis='y', labelcolor='b', labelsize=20)
ax1.tick_params(axis='x', labelsize=12)

# Secondary axis

ax2 = ax1.twinx()
ax2.set_ylabel('Y2-axis', color = 'green')
plot_2 = ax2.plot(labels, values2, marker='s', linestyle='--', color='r', label="Repetition Rate [1/s]")
ax2.set_ylabel("Repetition Rate [1/s]", color='r', fontsize=24)
ax2.tick_params(axis='y', labelcolor='r', labelsize=20)
ax2.yaxis.set_major_formatter(FormatStrFormatter('% 1.1e'))

# Formatting
ax1.set_xticklabels(labels, rotation=45, ha='right', fontsize=24)
ax1.set_title("PD Charge Magnitude and Repetition Rate", fontsize=30)
ax1.grid(True)

# Show plot
plt.tight_layout()
plt.show()

# Data
labels = [
    "Day 1", "Day 2", "Day 3 - One", "Day 3 - Two", "Day 4 - One", "Day 4 - Two", "Day 7"
]
values1 = [-14.3, -11, -81, -23, -77, -19, -20]
values2 = [4.17E+04, 1.14E+03, 1.59E+05, 1.60E+05, 1.60E+05, 1.60E+05, 1.60E+05]

titlesize = 30
labelsize = 24
ticksize = 24
```

```python
fig, ax1 = plt.subplots(figsize=(12, 8))

# Primary axis
ax1.plot(labels, values1, marker='o', linestyle='-', color='b', label="PD Apparent Charge Magnitude [pC]")
ax1.set_ylabel("PD Apparent Charge Magnitude [pC]", color='b', fontsize=24)
ax1.tick_params(axis='y', labelcolor='b', labelsize=20)
ax1.tick_params(axis='x', labelsize=12)

# Secondary axis

ax2 = ax1.twinx()
ax2.set_ylabel('Y2-axis', color = 'green')
plot_2 = ax2.plot(labels, values2, marker='s', linestyle='--', color='r', label="Repetition Rate [1/s]")
ax2.set_ylabel("Repetition Rate [1/s]", color='r', fontsize=24)
ax2.tick_params(axis='y', labelcolor='r', labelsize=20)
ax2.yaxis.set_major_formatter(FormatStrFormatter('% 1.1e'))

# Formatting
ax1.set_xticklabels(labels, rotation=45, ha='right', fontsize=24)
ax1.set_title("PD Charge Magnitude and Repetition Rate", fontsize=30)
ax1.grid(True)

# Show plot
plt.tight_layout()
plt.show()
```

B

Initial Test PD Measurements

An initial test setup before the arrival of the GIS test cell was implemented to gain a deeper understanding of the Omicron measurement equipment and the characteristic NoDi* patterns expected in both the preliminary and long-term experiments for each defect type. Two different test configurations were explored: a rod-plane setup, depicted in Figure B.1 and Figure B.2, and a rod-bowl setup, shown in Figure B.3. The rod-plane configuration was utilized for both AC and DC voltage tests. Initially, the MPD 600 model was employed before transitioning to the more advanced 800 series for improved measurement capabilities.

For the AC voltage test, a transformer was used to generate 30 kV, as illustrated in Figure B.1b, to induce PD activity at the rod suspended 21 cm from the plane electrode, as shown in Figure B.1a.

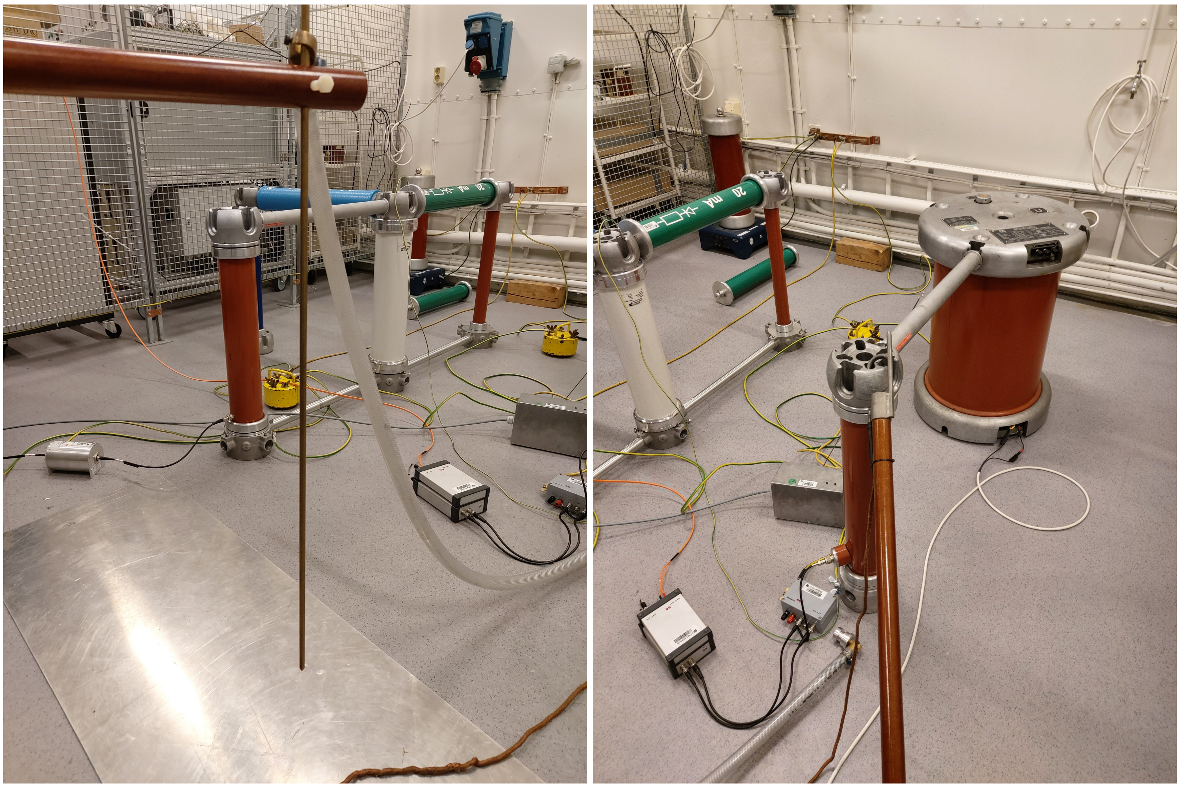

(a) Rod-plane electrode configuration

(b) AC circuit

Figure B.1: Pictures of the initial AC setup with rod-plane configuration

The test setup in Figure B.1 had a rectifier circuit in parallel that could be connected when DC voltage was desired, as shown in Figure B.2b. The rod was connected to the rest of the circuit using a water-filled resistor, as shown in Figure B.2a.

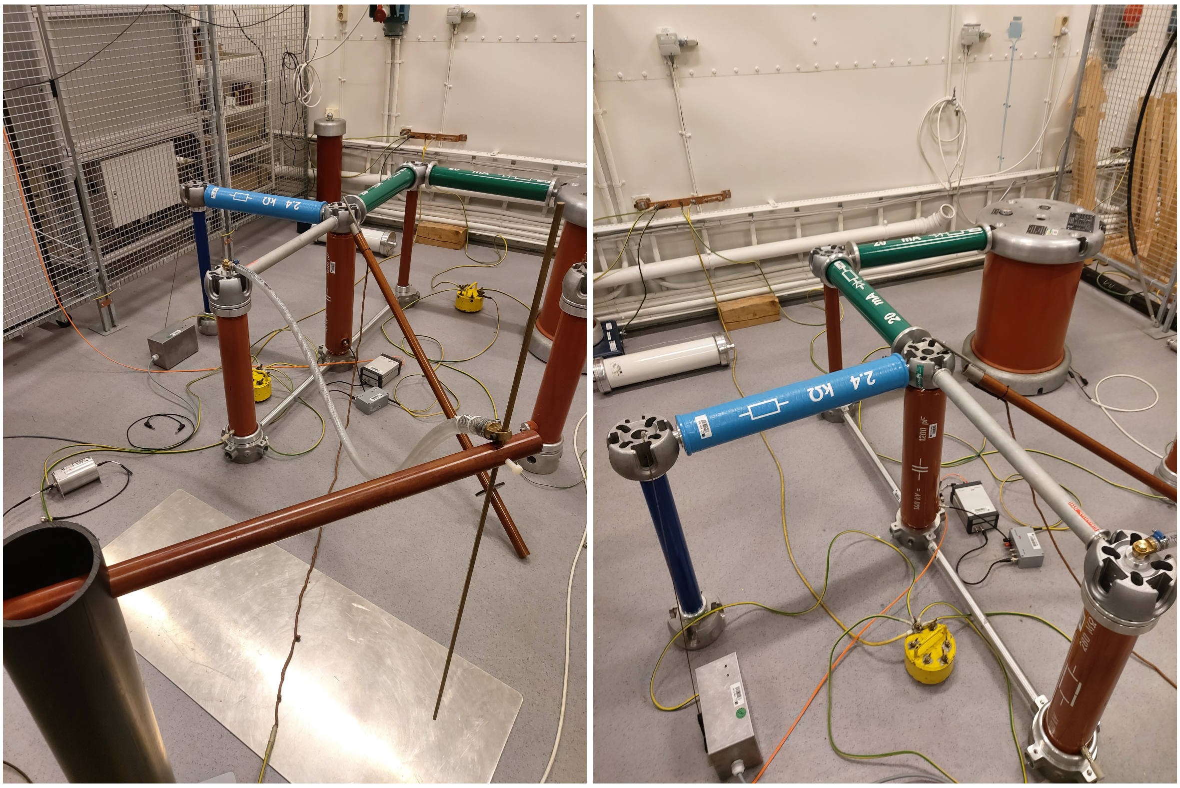

(a) Rod connection to rectifier circuit

(b) Rectifier circuit

Figure B.2: Pictures of the initial DC setup with the rod-plane configuration

The rod-plane configuration eventually evolved into the rod-bowl setup, as shown in Figure B.3. Similar to the situation with the stainless steel lid and copper hoop, two different particle containment setups were tried. The first one, consisting of half a spark gap as shown in Figure B.3a, was eventually replaced by the bowl depicted in Figure B.3b. After the delivery of the GIS test cell, the bowl was later repurposed to fabricate the copper hoop used in the free metallic particle defect setup. The original Spellman and FUG HVDC sources were utilized in this configuration as voltage levels up to 40 kV were sufficient.

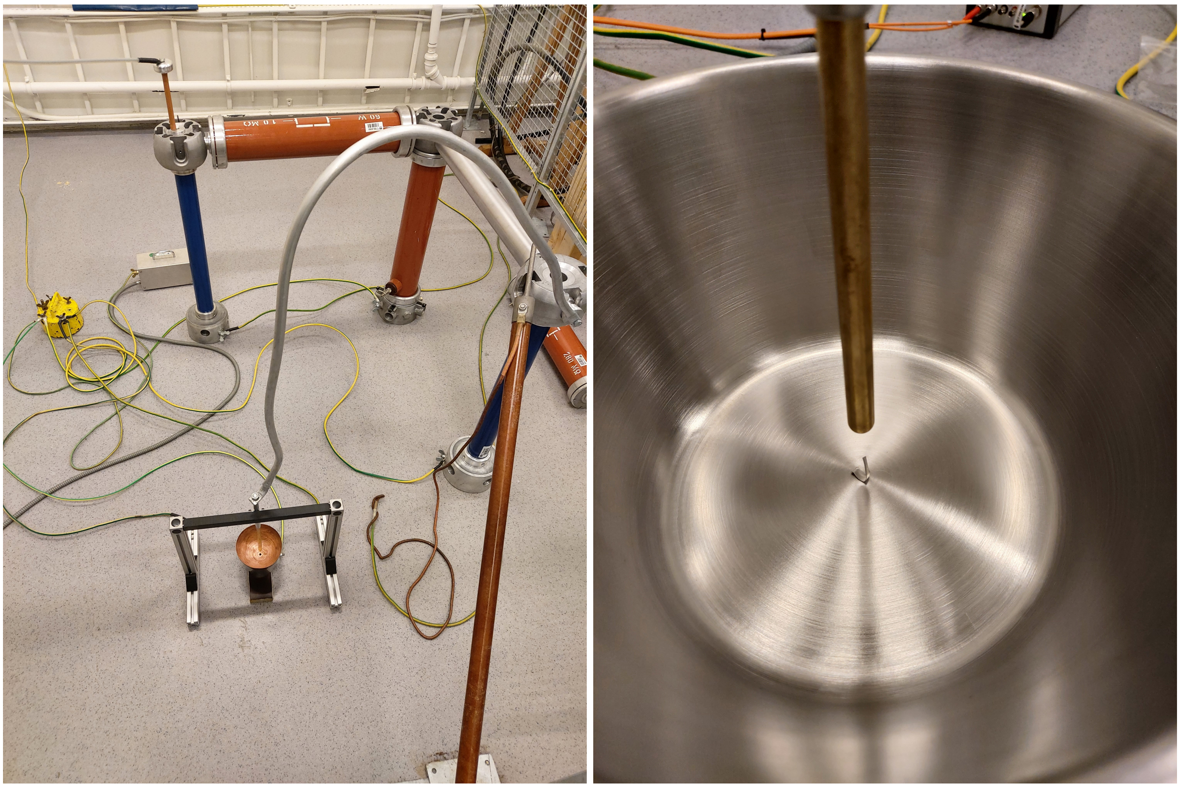

(a) Test circuit with coupling capacitor and rod-bowl setup

(b) Bowl with free metallic particle

Figure B.3: Pictures of the initial DC setup with rod-bowl configuration

The tests conducted using these two setups established a strong foundation for the rest of the study. By applying the fundamental principles outlined in Chapter 2, their significance was demonstrated in practical scenarios, reinforcing their critical role in PD measurements and analysis.

C

Additional Figures

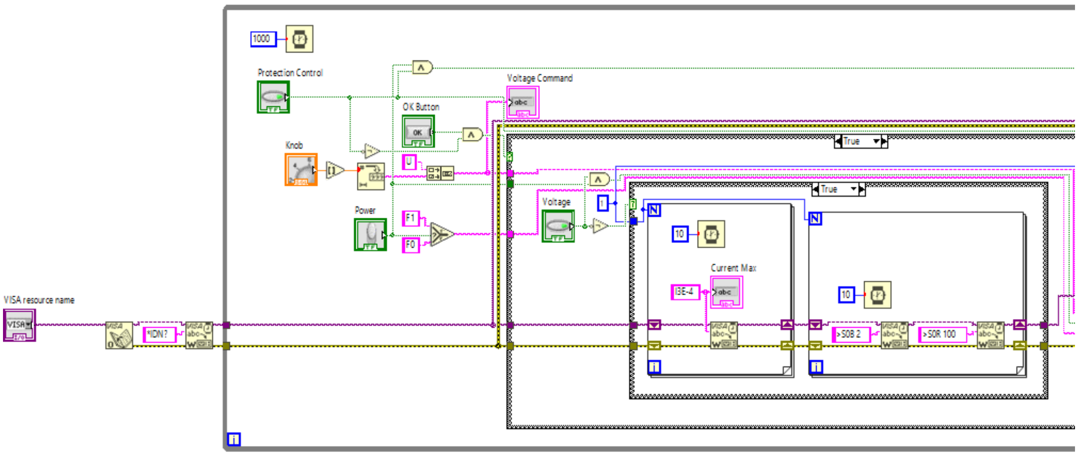

Figure C.1: First half of the LabView program backend for the HVDC source control and overcurrent protection

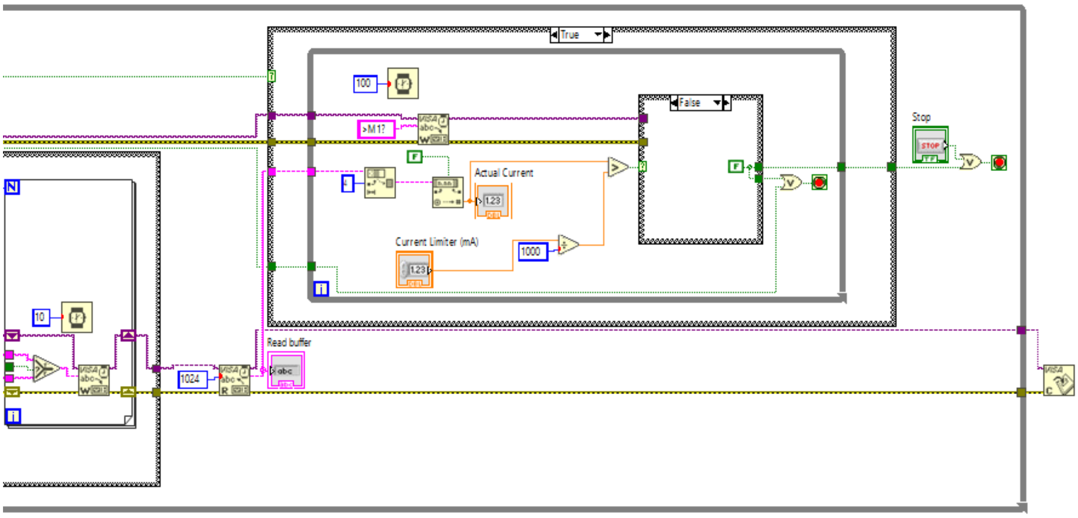

Figure C.2: Second half of the LabView program backend for the HVDC source control and overcurrent protection